Lawrence Berkeley Laboratory
UNIVERSITY OF CALIFORNIA

Materials & Molecular Research Division

MOLECULAR PHOTOEMISSION STUDIES
USING SYNCHROTRON RADIATION

Carlton M. Truesdale
(Ph.D. thesis)

April 1983

Prepared for the U.S. Department of Energy under Contract DE-AC03-76SF00098

DISCLAIMER

LBL-15902

MOLECULAR PHOTOEMISSION STUDIES USING SYNCHROTRON RADIATION

Carlton M. Truesdale

Ph.D. Thesis

Lawrence Berkeley Laboratory
University of California
Berkeley, California 94720

This work was supported by the Director, Office of Energy Research, Office of Basic Energy Sciences, Materials Sciences Division of the U. S. Department of Energy under Contract No. DE-AC03-76SF00098.

Table of Contents

MOLECULAR PHOTOEMISSION STUDIES USING SYNCHROTRON RADIATION

Carlton Maurice Truesdale

Materials and Molecular Research Division
Lawrence Berkeley Laboratory
and
Department of Chemistry
University of California
Berkeley, California 94720

Abstract

The angular distributions of photoelectrons and Auger electrons were measured by electron spectroscopy using synchrotron radiation. The experimental results are compared with theoretical calculations to interpret the electronic behavior of photoionization for molecular systems.

The synchrotron radiation source provides a time structure which allows the collection of time-of-flight (TOF) spectra. The photoelectron spectroscopy using the double-angle-time-of-flight method is discussed. Two advantages of this technique are the increased electron detection efficiency and a decreased systematic error. Automated control of the experimental data collection and on-line data analysis provide many advantages, such as increased ease of data acquisition and manipulation.

The photoelectron partial cross sections and asymmetry parameters β for the valence orbitals of H_2O were measured in the energy range $h\nu$ = 18-32 eV. The measurements are compared with earlier data and also multiple-scattering (MSMXα), atomic-extrapolation (AE), and Stieltjes-Tchebycheff moment-imaging (STMT) calculations. The

multiple-scattering model calculations agree well with our measurements of the photoelectron asymmetries β for the $1b_1$, $3a_1$, and $1b_2$ molecular orbitals of H_2O. The atomic character of the molecular orbitals is discussed in the context of the photoelectron angular asymmetry parameter β.

The vibrationally averaged photoelectron partial cross sections and asymmetry parameters β for the four outer valence orbitals of N_2O (X, A, B, and C) were measured over $h\nu$ = 19–31 eV. Vibrationally resolved data for the A and C ionic states were also obtained. The results are compared with previous measurements and multiple-scattering model calculations. A state-to-state comparison of the vibrationally averaged asymmetry parameters β of N_2O^+ and CO_2^+ was performed to show the behavior for these two isoelectronic triatomics. Similar changes in the asymmetry parameter are observed.

Vibrationally resolved measurements of the $1\pi_u$ molecular orbital of CO_2 over $h\nu$ = 18–26 eV were carried out. The vibrational states show shape resonances that are displaced in kinetic energy because of the different binding energies associated with each vibrational mode. Vibrationally resolved data for the 8σ molecular orbital of OCS were also obtained. The behavior of all but the (1,0,0) vibrational state of the $8\sigma^{-1}$ are similar. The results for CO_2 are compared with other synchrotron measurements, (e,2e) electron impact results, resonance-line measurements, and the vibrationally resolved multiple-scattering model calculations. The OCS results are compared with other

synchrotron measurements, and vibrationally averaged measurements of OCS are compared with theoretical predictions based on the multiple-scattering model.

Auger electron and photoelectron cross sections and asymmetry parameters were measured in the studies of the inner shell ionizations for CO, CO_2, CF_4, and OCS in the vicinity of the carbon (1s), oxygen (1s), and sulfur $L_{2,3}$ (2p) edges. The branching ratio for the O1s shake-up states of CO and CO_2, and the S2p shake-up states of OCS were also measured. Molecular shape resonances were observed for all of the carbon K-shell studies. Comparisons are made between other measurements and multiple-scattering, Stieltjes-Tchebycheff moment imaging, Hartree-Fock static exchange, and configuration interaction calculations. There are instances where each of these theoretical models has some success in predicting many of the observed molecular effects, such as shape resonances and the intensity of satellite-line intensities. To help explain the photoionization of the S2p level of OCS, "quasi-atomic" calculations have been performed. The S2p quasi-atomic calculations may suggest that correlation effects exist between the shake-up states and the S2p, because of the peculiar behavior in the S2p asymmetry parameter β near the ionization thresholds of S2p shake-up states.

David G Shirley

I. Theory

Sing softly young,
Bring bountiful gifts thee that have wealth.
Give tiny praises where praise is just,
And be what is intended you to be in this world.
Commit yourself (do not overthrow),
For the scenes and sights you focus on are totally unreal.
The world is a ripple in a pond,
A note to be sung.

From the travels of CMT

A. Introduction

The character of electronic structure and the photoionization process can be fully addressed when experimental measurements, collected over a range of photon energies, are compared with predictions based on theoretical models. Tunable synchrotron radiation makes it feasible to investigate energies, intensities, spin polarizations, and angular distributions of Auger electrons and photoelectrons. The measurements described in this dissertation in the tunable VUV and soft x-ray continua combine a synchrotron source and photoelectron spectroscopy in order to determine energy dependent photoelectron and Auger photoionization cross sections, angular distributions, and branching ratios.

Experimental measurements provide a test for the accuracy of theoretical results. In providing valid models that describe the

photoionization process, a requirement is for the mathematical solution to provide tractable information, so that experimental results can be interpreted. The marriage between experimental measurements and theoretical calculations will eventually lead to an accurate description of the photoionization process.

Experimental studies and theoretical calculations for molecular systems are at an early stage. Nonetheless, a large body of experimental data has been collected for a few molecular systems. Therefore a solid interpretation of molecular photoionization measurements awaits a clearer description to evolve from the comparision of theoretical models and experimental data. There are calculational difficulties in determining the continuum wavefunctions for multi-center systems; present models have schemes of approximation to circumvent these problems.

Measurements of photoelectron photoionization cross sections and angular distributions from the studies of H_2O, N_2O, CO_2, OCS, CO, and CF_4 are included in this dissertation. Vibrationally resolved results for N_2O, CO_2, and OCS were obtained. The Auger electron cross sections and angular distributions for CO, CO_2, CF_4, and OCS were also measured. The cross sections of the CO and CO_2 O1s shake-up states and OCS S2p shake-up states were also obtained.

In the remainder of this chapter, theoretical background material is presented. The list of references that accompany this discussion is not meant to be complete, but are examples to illustrate the topics presented.

In Chapter II the experimental apparatus and methods are described. The experimental results are discussed and compared with theoretical conclusions in Chapter III-VI.

B. Photoelectron Angular Distributions

A goal of molecular calculations is the proper treatment for the dynamics of molecular photoionization. A molecule (M) in the ground electronic state excited with monochromatic radiation $h\nu$ of suitable energy emits an electron as shown by

$$^{2S_o+1}M(\lambda_o) + h\nu \rightarrow {}^{2S_c+1}M^+(\lambda_c) + e^-(s\ell), \qquad (1)$$

where the λ_o and λ_c are the quantum numbers describing the rotational angular momentum of the initial state and ionic state projected on the molecular axis, respectively. The geometrical factors upon which the distribution of final ionic states depend are not affected by particular vibrational states of the neutral molecule and ionic state.[1] Full consideration for vibrationally resolved ionic states demonstrates that nuclear effects are apparent.[2] In the Born-Oppenheimer approximation which allows the separation of nuclear and electronic motion, the rotational quantum numbers of the ionic core need not to be considered when rotational structure is not resolved.[3] A full treatment of molecular rotation for diatomic molecules is given by Buckingham.[3]

Tunable radiation combined with photoelectron spectroscopy allows information to be derived from electronic structure of molecules

(atoms) by the measurement of ionization energies for the orbitals. The difference in energy between the final ionic state and initial state is called the ionization energy I. The kinetic energy ϵ of ejected electrons and ionization energy I are restricted by the conservation of energy as shown by

$$h\nu = I + \epsilon \tag{2}$$

Angular momentum (j) and parity (π) conservation lead to other restrictions placed on the ionization process as shown by the following equations:

$$h\nu(j_\gamma=1,\pi_\gamma=-1) + M(j_o,\pi_o) \rightarrow M^+(j_c,\pi_c) + e^-(s\ell,\pi_e=(-1)^\ell) \tag{3}$$

$$\vec{j} = \vec{j}_\gamma + \vec{j}_o = \vec{j}_c + \vec{s} + \vec{\ell} \tag{4}$$

$$\pi = \pi_\gamma\pi_o = \pi_c\pi_e \tag{5}$$

The photon has values $j_\gamma = 1$ and $\pi_\gamma = -1$ to specify electric dipole interaction during the absorption via collision with the target M. The parity of the photon is equal to -1 because the parity of a particle is defined as $(-1)^\ell$.[4] The photoelectron spin s will be neglected in the remainder of the discussion because the electron spin is not observed.

Two cases need to be discussed in identifying the parity conserved values of the asymptotic photoelectron angular momentum ℓ. In the first case, the initial state and final state parities π_o and

π_c are identical (equal symmetry), such that ℓ takes odd values of angular momentum (ℓ=1,3,5,...). In the second case, the initial state and final state have different parities, and ℓ takes even values of angular momentum (ℓ=0,2,4,...). For a thorough treatment of angular momentum topics refer to Brink and Satchler.[5]

The photoionization cross section and photoelectron angular distribution (spin-unobserved) are additional parameters necessary to describe the photoionization process.[6] In the electric-dipole approximation, the differential cross section $d\sigma/d\Omega$ of molecular (atomic) photoionization for a randomly oriented target (molecule or atom) which is excited by 100 percent linearly polarized radiation is given by

$$\frac{d\sigma(\epsilon,\theta)}{d\Omega} = \frac{\sigma(\epsilon)}{4\pi}\left[1 + \beta(\epsilon)P_2(\cos\theta)\right] \quad . \tag{6}$$

The differential cross section $d\sigma/d\Omega$ is a function of the kinetic energy ϵ of the photoelectron measured at an angle θ between the photoelectron emission referenced to the photon polarization axis.[7,8] $P_2(\cos\theta)$ is the second Legendre polynomial given as $\frac{3}{2}\cos^2\theta - \frac{1}{2}$. The angular distribution is completely described by the asymmetry parameter $\beta(\epsilon)$. The asymmetry parameter has physical solutions when the cross section has non-negative values, so that $\beta(\epsilon)$ is restricted to the range $(-1 \leq \beta(\epsilon) \leq 2)$. For low photon energies Eq. (6) is quite accurate. At higher photon energies, where the

photon momentum is on the order of the photoelectron momentum or the photon wavelength is nearly equal to the atomic dimensions (~Å), additional multipole components are needed to describe the angular distribution.[9,10]

The electronic structure of a molecule (atom) is sensitively described by measured cross sections and asymmetry parameters $\beta(\epsilon)$. The formulation of photoionization dynamics usually necessitates a definition of the continuum wavefunction, which is expanded in terms of alternate values of orbital angular momentum ℓ, partial-wave amplitudes, and interference terms. The cross section $\sigma(\epsilon)$ is found to be only dependent upon the magnitude of the partial-wave amplitudes given by the squares of the dipole matrix elements. Yet, the asymmetry parameter $\beta(\epsilon)$ is in addition dependent on the interference caused by non-Coulomb and Coulomb relative phase-shift differences and the signs of the dipole matrix elements.

Two energy domains characterize the angular distribution of photoelectrons. First, for non-resonant photoionization, the rapid variation in the asymmetry parameter $\beta(\epsilon)$ has been shown to be caused by the Coulomb phase-shift differences of the continuum waves.[11] Secondly, in the resonant case (excluding autoionization) variation in the asymmetry parameter $\beta(\epsilon)$ is attributable to variations in the dipole matrix elements.[11]

It has been shown that an alternative description of angular momentum dynamics can be achieved by defining the angular momentum transfer jt. Upon defining the angular momentum transfer jt,

bookkeeping of allowed momentum states for Eq. (4) is simplified.[12,13] The angular momentum transfer jt is the angular momentum vector difference taken between the final ionic state and the initial state or the photoelectron (ℓ) and the photon (1), shown by the following equation.

$$\vec{jt} = \vec{j}_c - \vec{j}_o = \vec{\ell} - \vec{1} \tag{7}$$

Transitions which have odd values of the sum $jt + \ell + j_\gamma$ are "parity favored" transitions. Even values for the sum $jt + \ell + j_\gamma$ refer to "parity unfavored" transitions. The asymmetry parameter for parity unfavored transitions is always equal to -1.[12]

The molecular symmetry requirements for molecular photoionization have been used to determine the selection rules governing jt[14] based on the character of the symmetry group. In that way, the role of symmetry properties in characterizing the angular distributions has been explicitly formulated for the direct ionization model. Table I. lists a few molecular point groups and the forbidden jt given by Druger.[14]

C. Auger Electron Angular Distributions

The present discussion will consider the ionization of K-shells for molecular systems. The vacancies produced in inner shells of molecules decay by an Auger process. The Auger decay accompanies the filling of the vacancy by an outer or inner valence electron. For photon energies that are insufficient to ionize core levels, excited electrons occupy discrete levels. After valence levels fill the

initial vacancy, singly-charged ionic states are subsequently produced. Doubly charged ions are produced when the photoexcitation energy is sufficient to ionize core levels. Molecular valence Auger spectra have been used to identify and analyze the elemental composition of large systems. Analysis of these spectra allows the possibility for unraveling final state assignments using atomic nomenclature, because core-level type Auger exhibit essentially atomic character.[15] Molecular Auger spectra have been studied experimentally[17-18] and theoretically.[15,19-23]

The kinetic energy of the ejected Auger electron ϵ_A (relaxation neglected) is given by[21]

$$\epsilon_A = I_c - I_j - I_k - U_{eff} , \tag{8}$$

where I_c, I_j, and I_k are the ionization potentials of the core, jth and kth valence levels, respectively. U_{eff} is the spin-dependent effective hole-hole interaction in the final state and is equivalent to the difference between the energy of the doubly ionized system and the ground state energy with additional energy given by I_j and I_k.

Molecular photoabsorption is expected to be highly anisotropic for discrete transitions because the excited states have particular symmetries and energies.[24] The interpretation of molecular Auger spectra is complicated by molecular orbital relaxation,[20] localization of the final hole states,[22] and hole-hole interaction in the final state.[24]

To calculate Auger electron intensities, Auger electron transition moments are required. The Auger transition moments can be expressed in terms of Coulomb (J_{ab}) and exchange (K_{ab}) integrals involving the continuum orbital $\phi(\varepsilon)$, the ionized 1s orbital, and the final state with holes in the outer molecular orbitals a and b.[13] The values of these Auger matrix elements are expected to be independent of the photon energy because the relative phases and Coulomb interaction should be static,[24] and the Auger matrix elements have been shown to be proportional to the atomic charge.[19]

The orientation of the molecular excited state affects the Auger electron angular distribution because the decay of the K-shell is a fast process compared with molecular rotation. For that reason, photoabsorption to a π excited state creates excited molecules that are expected preferentially to orient perpendicular to the electric vector of the light,[24] as for example, in CO.[25-27] In contrast, the σ shape resonance is expected to yield molecular ions preferentially oriented parallel.[24] Therefore the energy dependence of molecular Auger electron angular distributions should provide information about the anisotropy and identification of the symmetry of discrete excited and continuum states.[24]

The angular distribution of Auger electrons has been theoretically determined by Dill et al.[24] to be

$$\frac{d\sigma(h\nu,\theta)}{d\Omega} = \frac{\sigma(h\nu)}{4\pi}\left[1 + \beta_m(h\nu)AP_2(\cos\theta)\right] , \qquad (9)$$

where $\beta_m(h\nu)$ is the orientation parameter ($-1 \leq \beta_m \leq 2$) and A is a

constant ($-1/2 \leq A \leq 1$) that is characteristic for each Auger decay and is independent of the photon energy $h\nu$. One makes the identification that the Auger electron asymmetry parameter, $\beta_A(h\nu) = \beta_m(h\nu)A$, where A is expected to be nonzero.

The orientation parameter $\beta_m(h\nu)$ determines the alignment[28] due to unequal molecular orientations, parallel and perpendicular to the photon polarization vector, and is given by

$$\beta_m(h\nu) = \frac{2[D_\sigma^2(h\nu) - D_\pi^2(h\nu)]}{[D_\sigma^2(h\nu) + 2D_\pi^2(h\nu)]} \tag{10}$$

Unlike the photoelectron asymmetry parameter $\beta(\varepsilon)$, which includes interference between σ and π channels, the orientation parameter $\beta_m(h\nu)$ measures the photoabsorption strengths[24] D_σ and D_π, referenced to the photon polarization axis. In Chapter VI additional theoretical discussion of Auger asymmetry and experimental results is presented.

References

1. E.S. Chang, Proceedings of the Daresbury one-day meeting Feb. 16, 1978, edited by Brian D. Buckley, Daresbury Laboratory.
2. U. Fano and D. Dill, Phys. Rev. A 5, 185 (1972).
3. A.D. Buckingham, B.J. Orr, and J.M. Sichel, Phil. Trans. Roy. Soc. Lond. A 268, 147 (1970).
4. R. Eisberg, R. Resnick, Quantum Mechanics of Atoms, Molecules, Solids, Nuclei, and Particles, (New York, 1974) p. 691.
5. D.M. Brink and G.R. Satchler, Angular Momentum (Oxford, London, 1968).
6. K.N. Huang, Phys. Rev. A 22, 223 (1980).
7. C.N. Yang, Phys. Rev. 74, 764 (1948).
8. J. Cooper and R.N. Zare, J. Chem. Phys. 48, 942 (1968).
9. H.K. Tseng, R.H. Pratt, S. Yu, and A. Ron, Phys. Rev. A 17, 1061 (1978).
10. U. Fano and D. Dill, Phys. Rev. A 6, 185 (1972).
11. W. Thiel, Chem. Phys. Lett. 87, 249 (1982).
12. U. Fano, Phys. Rev. 135B, 863 (1964).
13. D. Dill, Phys. Rev. A 6, 160 (1972); D. Dill, Photoionization and other Probes of Many Electron interactions, ed. by F.J. Wuilleumier, 1976.
14. S.D. Druger, J. Chem. Phys. 64, 987 (1976).
15. H. Agren, J. Chem. Phys. 75, 1267 (1981).
16. W.E. Moddeman, T.A. Carlson, M.O. Krause, B.P. Pullen, W.E. Bull, and G.K. Schweitzer, J. Chem. Phys. 55, 2317 (1971).

17. C.I. Campbell, J.W. Rogers, Jr., R.L. Hance, and J.M. White, Chem. Phys. Lett. 69, 430 (1980).

18. J.C. Fuggle, in Electron Spectroscopy; Theory, Techniques and Applications, Vol. 4, edited by A.D. Baker and C.R. Brundle (Academic, New York, 1980).

19. D.R. Jennison, Phys. Rev. Lett. 40, 807 (1978).

20. D.R. Jennison, Phys. Rev. A 23, 1215 (1981).

21. D.R. Jennison, Phys. Rev. A 69, 435 (1980).

22. T.D. Thomas and P. Weightman, Chem. Phys. Lett. 81, 325 (1981).

23. T.A. Kelber, D.R. Jennison, and R.R. Rye, J. Chem. Phys. 75, 652 (1981).

24. D. Dill, J.R. Swanson, S. Wallace, and J.L. Dehmer, Phys. Rev. Lett. 45, 1393 (1980).

25. J. Stöhr, K. Baberschke, R. Jaeger, R. Treichler, and S. Brennan, Phys. Rev. Lett. 47, 381 (1981).

26. G.R. Wight, C.E. Brion, and M.J. van der Wiel, J. Electron Spectrosc. Relat. Phenom. 1, 457 (1973).

27. R.B. Kay, Ph. E. van der Leeuw, and M.J. van der Wiel, J. Phys. B 10, 2513 (1977).

28. J.L. Dehmer and D. Dill, Phys. Rev. B 17, 1692 (1978).

Table I. Character table of forbidden values of jt for representative symmetries and orbitals.

Symmetry group (orbital)	Forbidden values of jt[14]
$D_{\infty h}$ (Σ^+)	All even jt
$D_{\infty h}$ (Σ^-)	1
$D_{\infty h}$ (π)	0
$D_{\infty h}$ (Δ)	0,1
C_{2v} (B_1,B_2)	0
C_{3v} (E)	0
T (A)	1, 2, 5
T (E)	0, 1, 3
T (T)	0

II. Experiment

We embark on a self discovery,
And impose the restriction that
The universe is not under the command of chaos,
But directed by natural law.

A. Introduction

The molecular photoemission measurements discussed in this dissertation were all taken at the Stanford Synchrotron Radiation Laboratory (SSRL). The following discussion will describe the double-angle-time-of-flight instrumentation, analysis, and programming used in measuring photoelectron and Auger electron angular distributions. Many components have been discussed in detail by M.G. White, R.A. Rosenberg, S. Southworth, and P.H. Kobrin.[1-4]

B. Properties of the Synchrotron Radiation Source

TOF measurements were performed at SSRL because of the time structure and highly polarized character of the synchrotron radiation supplied to experimental stations (beam lines). Winick[5] has given a description of the properties of the electron storage ring (SPEAR) and its associated instrumentation at the SSRL facility.

Two beam lines were used to obtain TOF photoelectron and Auger spectra. The (8°) VUV beam line[6] I-3 uses a Seya-Namioka monochromator and has an operable energy range of $h\nu \simeq 4$-36 eV. The monochromator coupled with a 1200 line/mm grating and ~2.5 Å bandpass

delivers a flux of ~10^9-10^{10} photons per second/cm^2 when SPEAR operates with a 10 mA electron current. An aluminum window with a thickness of 1500 Å was used to separate our chamber vacuum (~10^{-4} torr) from the monochromator ultra-high vacuum (~10^{-10} torr).

Soft X-ray measurements can be performed at the (new 4°) beam line III-1.[7] Depending upon which grating is used, a grazing incidence "grasshopper" monochromator provides photon energies from $h\nu$ = 20-1000 eV. A 1200 line/mm grating was used for the measurements, so that 50 eV was the lowest attainable photon energy. Entrance and exit slits of the monochromator were adjusted to obtain a bandpass from 0.5 and ~5.0 eV. Depending upon the electron current in SPEAR and the monochromator bandpass used, the photon flux varies between 10^8-10^{10} photons per second/cm^2. On separate occasions an aluminum (1500 Å thick) and vitreous carbon (1000 Å thick) windows were used to separate the chamber vacuum from the monochromator vacuum.

C. Time-of-Flight Angular Distribution Measurements and Analysis

The experimental scheme is illustrated in Fig. 1. For single electron bunch operation of SPEAR, the photon pulses, which have a period of 780 nsec and a width of ~0.3 nsec, are monochromatized before entering our chamber. At the interaction region inside the chamber, the photon beam intersects a gas sample which has been introduced by an inlet probe positioned between two TOF detectors. The electrons emitted from the sample are detected by the TOF detectors placed at angles $\theta = 0°$ and $\theta = 54.7°$ relative to the photon polarization

direction. The electron signals are coincidenced with the signal from the electron storage ring to define the electron time-of-flight. The signals from the detectors are directed to a time-to-energy converter, and with routing electronics are stored in two quadrants of a multi-channel analyzer (MCA). Additional information about the instrument can be found in Refs. 1-4.

The TOF detectors provide major advantages for measurements of cross sections $\sigma(\epsilon)$ and asymmetry parameters $\beta(\epsilon)$ at low resolution. The entire spectrum is collected simultaneously at each photon energy, thereby enhancing the sensitivity, and the low duty cycle at each photoelectron and Auger electron kinetic energy enhances the signal/noise ratio.

As stated in Chapter 1, the differential cross section for excitation by plane-polarized photons takes the form

$$\frac{d\sigma(\epsilon,\theta)}{d\Omega} = \frac{\sigma(\epsilon)}{4\pi}[\ 1 + \beta(\epsilon)P_2(\cos\theta)\ ] \qquad (1)$$

At the "magic angle" of 54.7°, P_2 vanishes and the $d\sigma/d\Omega$ measurement yields $\sigma(\epsilon)$. Measurement of the relative intensities of electrons collected in the 0° and 54.7° spectra yields $\beta(\epsilon)$. We note that simultaneous data collection at two angles is intrinsically a more reliable method for obtaining $\beta(\epsilon)$ than measurements based on moving a single detector to several angles. Not only are the errors in reproducing the detector placements avoided, but fluctuations in photon beam intensity and sample gas density during each counting

period are totally compensated. The remaining principal sources of systematic error — relative detector efficiency for $\beta(\varepsilon)$ measurements and transmission of the 54.7° detector for $\sigma(\varepsilon)$ measurements — are dealt with in a calibration procedure.

Helium, argon, krypton, xenon, and neon are used as calibration gases. The asymmetry parameters given in the literature for these gases are compared to the ratio of the intensities measured by the 0° and 54.7° detectors in order to determine the relative efficiency of the two detectors as a function of the kinetic energy of electrons. Literature cross sections for these gases are compared with the relative intensity measurents taken by the 54.7° detector to determine the transmission of the 54.7° detector over the relevant electron kinetic energy. The calibration gases and sample gases were introduced into the sample chamber through an inlet probe described previously.[9] The sample density in the interaction region was taken as being proportional to the backing pressure (nominally 3 torr), which was monitored by a capacitance manometer.[9] The photon intensity was monitored by a sodium salicylate scintillator, phototube, and picoammeter. For each counting period (typically 1000 s), the relative photon flux and sample pressure were integrated and stored with electronic counters.

Data reduction is straightforward because of the calibration procedure. A more detailed description of this procedure has been given by Southworth et al.[8] Briefly, $\beta(\varepsilon)$ values are determined from the ratio of the peak areas determined from the ratio of the peak

area measured at 0° [$A(0°,\varepsilon)$] and 54.7° [$A(54.7°,\varepsilon)$] and the relative collection efficiency [$f_0(\varepsilon)$] of the two detectors,

$$\beta_0(\varepsilon) = -1 + \frac{A(0°,\varepsilon)/A(54.7°,\varepsilon)}{f_0(\varepsilon)} \qquad (2)$$

The $\beta_0(\varepsilon)$ measurements are corrected for a small unpolarized photon-beam component, for angle averaging over the finite source region and the collection solid angles, and for the difference between the measured $\beta(\varepsilon)$ value and that of the calibration photoelectron line. It should be noted that because of the internal calibration procedure performed, the derived asymmetry parameters are only rather weakly dependent on the degree of polarization of the radiation, on geometrical parameters of the interaction and detection system, and on certain experimental systematic errors.[8]

Peak areas measured at 54.7°, after normalization for sample density, photon intensity, and transmission of the 54.7° detector, were corrected in an analogous fashion to the $\beta(\varepsilon)$ values to yield relative partial cross sections. These were then scaled to yield absolute cross sections (usually) with the use of previously measured total cross sections.

D. Time-of-Flight Programming

The experimenter can effectively handle the stress of recording data, while being able to condense those measurements into meaningful results, with the aid of automation. On the average, it is necessary for TOF experimenters working at SSRL to be able to take data for 24

hours per day for a period of two weeks and interpret the data simultaneously. Therefore the experimenter must be prepared to be make efficient use of beam time granted, by possessing reliable hardware and effective software to control experimental data acquisition and manipulation.

The TOF experiment has evolved from being equipped with the bare necessities to a more sophisticated method for taking measurements and performing data analysis. In the early stages of this project, the data were stored on magnetic tape. The on-line data analysis consisted of integrating peaks from the 0° and 54.7° detectors by using a pen plotter that digitized the background and peak locations to calculate peak areas. Although we could determine relative cross sections with the peak intensities measured at 54.7°, the limited size of memory provided by an Motorola 8080 microprocessor (8K words) did not afford us the opportunity to program without severe restrictions on the size and capabilities of the software package. Presently, our 16 bit LSI-11/23 microprocessor has 64K bytes program space and a total addressable memory of 256K bytes.

In the discussion to follow, a brief description will be given of some of the hardware devices used for the TOF measurements. The discussion will concentrate on important topics that will in general guide the experimenter to produce software with simple, standardized, and understandable routines. The focus of these topics describes the development of the program called TOFCON (time-of-flight control), its structure, the inherent problems in its specific operation, and the

considerations needed to improve its capabilities. This program is designed to allow the experimenter to record and analyze photoelectron and Auger electron spectra with relative ease without sacrificing the attributes of performing rigorous data reduction. Topics that are related to program development are discussed to help future workers in the TOF "group" avoid some problems and pitfalls that can easily hinder one during experimental measurements, and understand the TOFCON program structure in order to be able to effectively change it without being forced to create an entirely new program.

A short list of the hardware devices (excluding signal processing) that record, store, and help in handling the data is given below.

1. Canberra Series 40 MCA (multi-channel analyser).
2. Hewlett-Packard 7220A pen plotter (microprocessor-based, RS-232C interface).
3. Ortec 778 dual counter.
4. Digital LA-120 line printer.
5. Digital VT-55 terminal.
6. Data Systems Design 8" floppy disk drive.
7. Digital LSI-11/23 microprocessor.

The Canberra Series 40 MCA records the time-of-flight spectra in two of four quadrants. With the use of Macro-11 routines supplied by the manufacturer, the MCA can be programmed to send peak locations and data to the LSI-11/23 microprocessor. The data are finally stored on double-density floppy disks. There are many static control

capabilities of the MCA. The data can be expanded, presented on a log scale, the area can be approximated, simultaneous live display of the 0° and 54.7° spectrum can be presented, and regions of the spectra can be highlighted (regions of interest) to locate peaks.

One of the indispensable hardware devices for TOF studies is a plotter. The plotter produces hard copy of spectra, graphs, and figures. An added value imparted to the Hewlett-Packard 7220A plotter is the ability to be programmed with the HP-GL plotter language. The pen plotter can perform tasks like drawing curves, digitizing points and graphs, and making special symbols (e.g., greek characters).

In order to derive partial cross sections, the intensity measured by the 54.7° detector must be normalized for sample density and photon flux. The sample density is monitored with a Barytron capacitance manometer, and the photon flux is detected with a sodium salicylate scintillator, phototube and picoammeter. The signals from the manometer and picoammeter are sent to separate channels of the Ortec 778 dual counter in order to store the integrated sample density and photon flux. The computer can start and stop the counter, and read the integrated sample density and photon flux for later storage with the experimental data on floppy disk.

The data or results can be printed with the Digital LA-120 line printer. This high speed (~120 char/sec) printer can be used to print quickly calculations and data, so that large amounts of time are not wasted generating our large volume of output. The LA-120 printer can also be used as a terminal.

The Digital VT-55 terminal is used to direct processes executed by the LSI-11/23 microprocessor or other peripheral devices. The keypad can be controlled by a text editor for easy creation/modification of text, such as program sources. The progress of tasks can be monitored by printing information to the terminal, and the experimenter can be prompted to supply additional information to complete certain menus.

The DSD 440 floppy disk system can read, write, modify, create, and delete data in the form of files. Two 512K byte floppy disks are managed by the controller. One of the disks is a system disk having routines for directory maintanence, program generation, and general file utilities. The other disk usually contains data of some sort and/or Fortran sources.

The Digital LSI-11/23 microprocessor performs calculations and directs tasks to be carried out by appropriate hardware devices. In addition this device allows software routines of a program to be overlaid. With this feature, many routines can be added together. These routines are grouped into certain regions and segments.

The TOFCON program is command activated. The main routine requests that the user specify a valid command. A valid command is a four letter descriptor that is defined prior to program execution. The four letter command activates a particular task or tasks to be completed. Besides having the ability to act on elementary commands, one can generate a menu consisting of a repetition of elementary commands.

There are two modes of operation for TOFCON. Firstly, one can work in an "echo" mode. In the echo mode there are forced instances where the terminal requires the user to input information before a task can be completed. In contrast, the "no-echo" mode allows answers to questions to be predefined and supplied internally to the program. A file contains the default answers that the TOFCON program uses to determine appropriate methods of action for certain tasks. The default values also reside in memory and can be easily changed. If the user wishes to know the individual questions that are allowed to be answered by defaults, he need only type that command and the default questions and their current values can be seen on the terminal or directed to be printed by the line printer. One power of the no-echo mode is that answers to questions can be defined, so that the user can alleviate supplying monotonous and unnecessary input. An entire process can in principle take place with the user only inputting the appropriate command.

To understand the capabilities of the TOFCON program, one needs to know the specific tasks it has been designed to perform. There are three classes of operations that TOFCON can carry out. The TOFCON program can be used in conjunction with hardware devices to retrieve data stored in the MCA, analyze data, and manufacture figures. The following discussions will only give a few of the possible uses of the TOFCON program.

The first class of tasks include the transfer of data to and from the MCA. The TOFCON program can be used to transfer data from the MCA

to floppy disk and vice versa, to retrieve the spectral peak and background locations from the MCA, and to retrieve the output of the dual counter. While data are being collected in two quadrants of the MCA, the previous spectrum can be analyzed in the other two quadrants of the MCA or by the pen plotter. The specification for this class of operations is that data acquisition is never restricted by data manipulations.

The second group of tasks that TOFCON can perform is data analysis. TOFCON contains routines that can determine peak areas, backgrounds, photoionization cross sections, asymmetry parameters, and branching ratios. TOFCON can also be used to do peak fitting, time-to-energy conversion of spectra,[4] digitization of points or graphs, and column algebra.

The last category of uses of the TOFCON program is for making figures. The natural path from obtaining data, to deriving the important results, is to present the results in a clear illustration. The TOFCON program allows one to plot graphs with variable-automatic axes and special characters. Easily understandable routines make it possible to make figures of journal quality without requiring a draftsman to produce them. Thus time is saved and experimenters can effectively proceed from the process of taking measurements to the completion of a paper, which presents the significant experimental results.

In some instances, high-quality graphics can be generated with programs on the VAX. The VAX is 32 bit interactive minicomputer that

contains other routines capable of data analysis and graphics. A program called RPN was written by John Barton, Charlie Bahr, students of the same research group as myself, and Dennis Trevor (former graduate student). The RPN program stands for Reverse Polish Notation. Without giving a detailed explanation of the design and operations possible using this program I quote Charlie Bahr, "the general purpose Reverse Polish Notation (RPN) program residing on the VAX computer (with a condensed version capable of being operated on a DEC LSI-11/23) has been used for graphics, curve fitting, Fourier analysis, spectral manipulations (summing, subtracting, smoothing, etc.), and various I/O specific to different types of data. The command structure is very sophisticated, allowing compound commands to be defined in terms of elementary operations. RPN can be programmed to perform a series of repetitive operations. The extreme generality of RPN has given it great flexibility and consistency."

Looking to the future, the TOF method can improve its capabilities in collecting data and performing data analysis by making further improvements in the TOFCON program. A major improvement in the TOF method can be achieved by allowing the experimenter the ability to take measurements in a monochromator scanning mode. With a few modifications and additions to existing routines, one could automatically scan the monochromator and monitor the peak areas of the 0° and 54.7° detector as a function of photon energy. The peak locations can be determined by modifying the time-to-energy conversion

routine to provide the peak locations for peaks with binding energies E_B. By including the total experimental resolution one can describe the peak shapes.

TOFCON can become a simpler and more general program by considering only a few ideas. The limitations and problems associated with the TOFCON program must be described if any effective resolution to those difficulties is achieved, so that the TOFCON can evolve into a more sophisticated sofware package. In the future the TOFCON program should be able to accept future "undefined" data characteristics and data types (e.g., 3 angle spectra). To this end, the flexibility of the program is improved.

A modification of the command structure and menu selection can also improve the general use of the TOFCON program. If commands are created that answer specific questions, unnecessary queries by the program can be reduced. To be able to access any task from any location in the program is highly desirable. With that capability, the full power of the TOFCON program can be utilized.

In summary, the continued development of the TOFCON program is encouraged. Experimenters can effectively handle the burdens of taking measurements and simultaneously analyzing the measurements with the TOFCON program. It is wise to build upon the routines of this program to create a flexible and adaptable software system by improving the command structure, and increasing the task capabilities of the TOFCON program.

References

1. M.G. White, Ph.D. Thesis, University of California, Berkeley (1979); Lawrence Berkeley Laboratory report No. LBL-9527.
2. R.A. Rosenberg, Ph.D. Thesis, University of California, Berkeley (1979); Lawrence Berkeley Laboratory report No. LBL-8948.
3. S. Southworth, Ph.D. Thesis, University of California, Berkeley (1982); Lawrence Berkeley Laboratory report No. LBL-13512.
4. P.H. Kobrin, Ph.D. Thesis, University of California, Berkeley (1983); Lawrence Berkeley Laboratory report No. LBL-15591.
5. H. Winick, in Synchrotron Radiation Research, H. Winick and S. Doniach, eds. (Plenum, New York, 1980).
6. V. Rehn, A.D. Baer, J.L. Stanford, D.S. Kyser, and V.O. Jones, in VUV Radiation Physics, E. Koch, R, Haensel, and C, Kunz, eds. (Pergammon-Vieweg, London/Braunswieg, 1974), p. 780.
7. F.C. Brown, R.Z. Bachrach, and N.L. Lien, Nucl. Instrum. Meth. 152,73 (1978).
8. S. Southworth, C.M. Truesdale, P.H. Kobrin, D.W. Lindle, W.D. Brewer, and D.A. Shirley, J. Chem. Phys. 76, 143 (1982).
9. M.G. White, R.A. Rosenberg, G. Gabor, E.D. Poliakoff, G. Thornton, S.H. Southworth, and D.A. Shirley, Rev. Sci. Instr. 50, 1288 (1979).

Figure Caption

Figure 1. Schematic diagram of the double-angle-time-of-flight experiment for measuring photoelectron and Auger electron angular distributions. The synchrotron radiation time structure is used to record time-of-flight spectra. One detector placed at 0° and another detector placed at 54.7° with respect to the photon polarization axes simultaneously measure electrons.

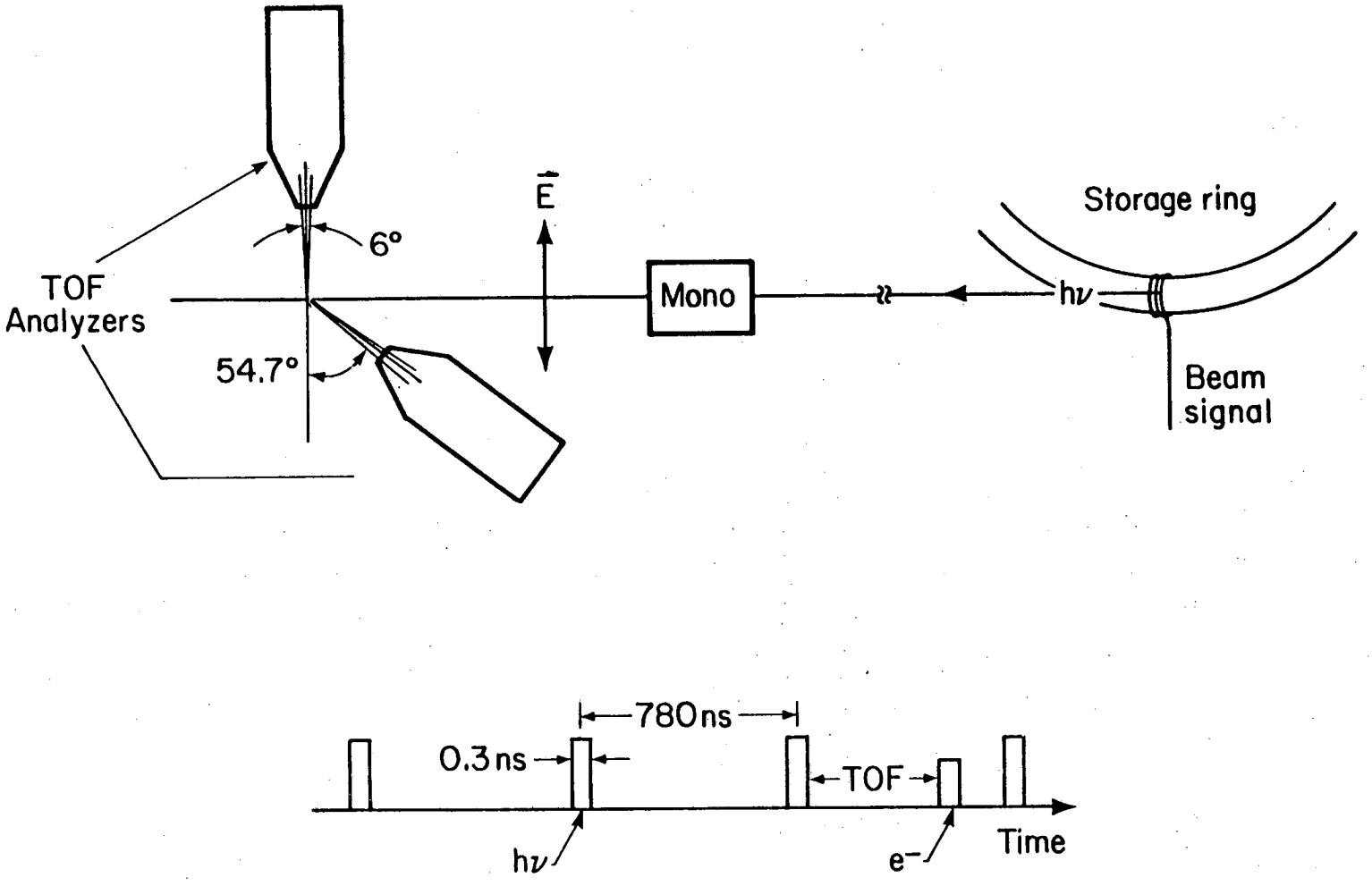

XBL 7910-4225

Fig. 1

III. PHOTOELECTRON ANGULAR DISTRIBUTIONS OF H_2O*

A. Introduction

Photoionization of the water molecule is a reaction of very wide interest. As in any photoionization process to which Yang's criteria[1] of initial-state random orientation and dipole multipolarity apply, and where the spin of photoelectrons is not detected, two parameters must be measured to describe photoionization to a given ionic state through a given channel.[2] These are the angle-integrated cross-section, $\sigma(\varepsilon)$, and the asymmetry parameter $\beta(\varepsilon)$, where ε is the photoelectron kinetic energy. If θ denotes the angle between the photoelectron propagation direction and the polarization vector of the exciting radiation, the differential cross section for excitation by plane-polarized photons takes the form

$$\frac{d\sigma(\varepsilon)}{d\Omega} = \frac{\sigma(\varepsilon)}{4\pi}\left[1 + \beta(\varepsilon)P_2(\cos\theta)\right] , \qquad (1)$$

where $P_2(\cos\theta)$ is the second Legendre polynomial, equal to $\frac{1}{2}(3\cos^2\theta - 1)$. Thus, the photoionization of H_2O can be characterized

---

* C. M. Truesdale, S. Southworth, P. H. Kobrin, D. W. Lindle, G. Thornton, and D. A. Shirley, J. Chem. Phys. 76, 860 (1982).

by measuring $[d\sigma(\epsilon)/d\Omega]$ at two or more ejection angles for the various photoionization channels, each of which corresponds to ejection of an electron from a particular molecular orbital. $\beta(\epsilon)$ characterizes the angular distribution of the photoelectrons. The complementary measurement of photoelectron spin polarization, in addition to $\sigma(\epsilon)$ and $\beta(\epsilon)$, would completely describe the photoionization process.[3]

In this paper we report $\sigma(\epsilon)$ and $\beta(\epsilon)$ measurements for the processes

$$H_2O + h\nu \rightarrow H_2O^+ (^2B_1, 1b_1^{-1}) + e^- \quad (2a)$$

$$H_2O + h\nu \rightarrow H_2O^+ (^2A_1, 3a_1^{-1}) + e^- \quad (2b)$$

and

$$H_2O + h\nu \rightarrow H_2O^+ (^2B_2, 1b_2^{-1}) + e^- \quad (2c)$$

for photon energies in the range $h\nu$ = 18–31 eV. These measurements are compared with previous experimental results and with theory.

The experiments were performed at the Stanford Synchroton Radiation Laboratory, on the VUV beam line.[4] This source provides highly (>97 percent)[4] linearly polarized radiation. The time structure of this source (0.3 nsec pulse length, with a 780 nsec period) facilitated the use of a specially designed time-of-flight (TOF) detector.[5] These experiments were performed with a 2.7Å (FWHM) monochromator band pass throughout the available radiation energy range of 18–31 eV.

As calibration gases we used helium and a rare gas mixture of argon, krypton, and xenon. The asymmetry parameters for these gases were taken from previous resonance-line and synchrotron-radiation measurements.[6,7] Both the relative efficiencies of the two detectors and the transmission of the 54.7° detector over the relevant electron kinetic-energy range were thereby obtained. A detailed description of the calibration procedure has been given by Southworth et al.[8] The calibration gases and sample gas (H_2O) were introduced into the sample chamber, through an inlet probe described previously.[5] The photon intensity was monitored by a sodium salicylate scintillator, phototube, and picoammeter. For each counting period (typically 1000 sec), the relative photon flux and sample pressure were integrated and stored on scalers. The backing pressure for the gases was nominally 3 torr. A typical TOF spectrum for the outer three molecular orbitals of H_2O is shown in Fig. 1. There is good separation of the molecular orbital peaks, but vibrational structure is not resolved.

The derived relative cross sections measured by the 54.7° detector, which are normalized for sample density, photon flux, and transmission of the 54.7° detector, were scaled to yield absolute partial cross-sections by the use of the total photoabsorption cross- sections measured by L. de Reilhac and N. Damany[9] and the ionization efficiencies reported by Katayama, et al.[10]

There are two Sections to follow. Results are presented and discussed in Section B and conclusions are given in Section C.

B. Results and Discussion

At this early stage in the development of theories of molecular photoionization, any discussion of molecular $\sigma(\varepsilon)$ and $\beta(\varepsilon)$ parameters must be somewhat tentative. Therefore, comparisions of results from different experimental and theoretical sources must perforce be an implicit evaluation of the methods employed by those sources. Thus, in the context of discussing our results we are addressing methodologies as well as the physical properties of the water molecule.

The ground-state electronic configuration of water is $(1a_1)^2\ (2a_1)^2\ (1b_2)^2\ (3a_1)^2\ (1b_1)^2$. In the UV range available, the $1a_1$ and $2a_1$ electrons are too strongly bound to be ejected. The other three orbitals can be ionized according to the channels in Eq. 2. In Table I, we present the partial cross-sections and asymmetry parameters for these three channels in the photon energy range 18-31 eV. Also shown for comparison are $\beta(\varepsilon)$ values at $h\nu$ = 21.2 eV, reported by Carlson and McGuire[11] and by Katsumata, Achiba, and Kimura,[12] and the $\sigma(\varepsilon)$ measurements at 21.2, 23.5, and 24.5 eV reported by Katsumata, et al. and dipole (e,2e) results of Tan, Brion, van der Leeuw, and van der Wiel.[13] The agreement is good.

Before separately discussing our results for the three channels, we note a strong similarity among them. This arises, as Roche, Salahub, and Messmer[14] have pointed out, because the $1b_1$, $3a_1$, and $1b_2$ molecular orbitals are all derived from the O 2p shell. Banna and Shirley carried this analogy further in discussing photoemission from the second-row hydrides,[15] noting both their conceptual

derivation from neon and the dominant contribution of the second-row atom's valence orbitals (rather than a hydrogen "1s" orbital) to the photoemission cross-sections. Roche, et al.[14] computed $\sigma(\epsilon)$ and $\beta(\epsilon)$ values for O 2p to compare with their H_2O molecular-orbital $\sigma(\epsilon)$ and $\beta(\epsilon)$ results, which are based on the multiple-scattering $X\alpha$ method.[16,17] Thus, the strong similarity among the $\sigma(\epsilon)$ and $\beta(\epsilon)$ curves (Figs. 2, 3, and 4) for the three channels is the first qualitative success of this theoretical picture. A more quantitative measure of the success of $X\alpha$ computations is obtained by comparison with other theoretical curves and with experiment, as discussed below.

The lone-pair $1b_1$ orbital is least distorted from an atomic O 2p orbital by the presence of the atomic hydrogens because this orbital is orthogonal to the plane of the molecule and is nonbonding. As predicted,[14] both $\sigma(\epsilon)$ and $\beta(\epsilon)$ follow the atomic orbital curves quite closely as shown in Fig. 2. The observed ~60 percent increase of $\beta(\epsilon)$ with increasing energy agrees well with the $X\alpha$ calculation, and the agreement of the $\beta(\epsilon)$ behavior near the end points leaves little to be desired. The MS$X\alpha$ calculation predicts a decrease of $\sigma(\epsilon)$ by about 20 percent with increasing energy, although the absolute value of $\sigma(\epsilon)$ is typically 20 percent higher than predicted. There is better agreement between our $\sigma(\epsilon)$ results and $X\alpha$ calculation below 20 eV photon energy.

The magnitude of $\sigma(\epsilon)$ was predicted more accurately by Williams and Langhoff,[18] and by Hilton, Nordholm, and Hush.[19] The former calculation was based on the Stieltjes-Tchebycheff (ST) moment imaging

theory,[20,21] and the latter is developed by use of the ground state inversion potential method (GIPM). The ST approach uses variational calculations of square-integrable wavefunctions of the photoelectron interacting with a non-local and noncentral molecular-ionic potential. It yields pseudospectra and oscillator strengths from which the cross-sections are derived by moment-imaging methods, but $\beta(\epsilon)$ is not calculated because the continuum wavefunctions are not determined. It should, however, be capable of predicting structure in $\sigma(\epsilon)$, a subject to be discussed latter. The ST calculation of Delaney, Saunders, and Hillier[22] is in only qualitative agreement with our results for predicting the decrease in $\sigma(\epsilon)$ as a function of photon energy.

The GIPM calculation determines the molecular orbital cross-sections from those of the atomic subshell components. It can include the interference effects between the atomic components of the molecular orbital.[21] As stated, the calculations of Hilton, et al. predict $\sigma(\epsilon)$ with rather good accuracy. Their model determined that interference effects between the atomic components of the $1b_1$ molecular orbital are negligible.

We conclude our comments on the gross form and magnitude of $\sigma(\epsilon)$ for the $^2B_1(1b_1^{-1})$ transition by noting that, although the (e,2e) data do not show any resonance structure, there is otherwise good qualitative agreement between our results and the (e,2e) data of Tan, et al.[13] throughout the range of our measurements. Maxima in our $\sigma(\epsilon)$ data appear near 22 eV and 25 eV, and some structure is present below 20 eV. Dutuit, et al. reported photoelectron intensities for

this state up to 20 eV, with structure at 19 eV, but their reported cross-sections are higher than ours in the small region of overlap.[23] Those authors suggest that the broad maximum at 19 eV may be due to a competition between neutral dissociation and autoionization to ionic states of H_2O. Wu and Judge, who reported recent measurements of Lyman α fluorescence of neutral dissociation products of H_2O, have suggested that a sharp structure present in absorption spectra at ~18.5 eV corresponds to an s-like Rydberg state, converging to the $^2B_2$ ionic channel, from which predissociation occurs.[24] This explanation accounts for resonance structure in, and competition between, the photoionization and dissociation channels.

The two ST calculations are somewhat different in detail, one being based on the time-dependent Hartree-Fock (TDHF) approximation[18] and the other on a static-exchange approximation,[22] and their resulting $\sigma(\epsilon)$ curves differ as well. In particular, excitations of virtual discrete states and states in the ionization continuum (e.g., $1b_1 \rightarrow 4a_1$) in the TDHF[18] calculation were found to yield maxima in the sub-channel cross sections for the $^2B_1$ ($1b_1^{-1}$) channel. These maxima were smaller or absent in their final curves. A broad shape resonance centered around 22 eV photon energy due to excitation of a σ^*a_1 valence-like orbital predicted by Williams and Langhoff may identify the resonance structure located at ~22 eV in the present work. Figure 2 shows that Delaney et al.[22] also find structure in the $\sigma(\epsilon)$ curve at ~18 eV for the $^2B_1$ state, but with small amplitude. The experimental response feature in $\sigma(\epsilon)$ for the $^2B_1$ state below 20 eV

may also result from the shape resonance predicted by Delaney, et al. Until confirmatory measurements are made it seems prudent to defer further interpretation.

The $\beta(\varepsilon)$ parameter for the $^2B_1$ $(1b_1^{-1})$ channel has been measured previously only at fixed energies (see Table I), and has been calculated only by Roche, et al. As noted above, agreement between experiment and theory is excellent, except for the structure near $h\nu$ = 22 eV and 25 eV, as in $\sigma(\varepsilon)$. In particular, $\beta(\varepsilon)$ starts relatively high (0.76) at $h\nu$ = 18 eV, rises quickly to 1.0 by $h\nu$ = 20 eV, and (except for the structure near 22 eV and 25 eV) remains large and increases to ~1.4 near 30 eV, in good accord with the Xα results.

Results for the $^2A_1(3a_1^{-1})$ channel are shown in Fig. 3. There is good agreement among our measurements, the results of Dutuit, et al.[23] above 22 eV, and the (e,2e) results[13] for the entire photon energy range. This channel involves the "O 2p-like" orbital, which is in-plane and directed along the C_{2v} axis. It has significant involvement with the hydrogen atoms. This fact is evident in photoemission. For example, in earlier work[15] the $^2A_1$ intensity was shown to increase much more between spectra excited by soft-x-ray radiation (132.3 eV) and those excited by higher energies (1487 eV) than did those of the $^2B_1$ or $^2B_2$ states. This suggests that O 2s admixture is present in the $3a_1$ orbital. We interpret this as being due to sp hybridization, which is allowed by symmetry. Thus, unlike the $1b_1$ and $1b_2$ orbitals, the $3a_1$ orbital does not have a nodal plane through the oxygen nucleus.

There is little difference between the present experimental $\sigma(\epsilon)$ values for the $^2B_1$ $(1b_1^{-1})$ and $^2A_1$ $(3a_1^{-1})$ states, although the calculated $\sigma(\epsilon)$ values of Roche, et al. are somewhat higher for the $^2A_1$. On the average, the Xα calculation is somewhat closer to experiment than the ST[18,22] or GIPM[19] results. The GIPM calculation that includes interference effects for the $^2A_1$ channel is presented in Fig. 3: the GIPM calculation without interference effects would be in better agreement with the present results, judging from the four points given by Hilton, et al.[19] The GIPM $\sigma(\epsilon)$ curve shown in Fig. 3 predicts a broad maximum near 20 eV.[19] Delaney, et al.[22] predict a resonance at ~19 eV. Williams and Langhoff[18] predicted that a continuum subchannel resonance ~25 eV is present for the excitation into the continuum σ^*a_1 orbital. The experimental structure falls at ~18 eV, ~22 eV, and ~25 eV.

The prediction of $\beta(\epsilon)$ for the $^2A_1$ $(3a_1^{-1})$ ionic state is a success for the Xα model. The theoretical curve starts at a low value of 0.6 at $h\nu$ = 18 eV and rises to a value of 1.2 near $h\nu$ = 31 eV, in good overall agreement with the data. This behavior is to be contrasted to the $\beta(\epsilon)$ curve for the $^2B_1$ $(1b_1^{-1})$ channel discussed above. The two $\beta(\epsilon)$ curves are quite different in detail, as a careful comparison will show, and on a coarse scale the predicted differences are closely followed experimentally. The difference of the $^2A_1$ $(3a_1^{-1})$ $\beta(\epsilon)$ curve from that for the $^2B_1$ $(1b_1^{-1})$ state, which closely follows the differences from the $\beta(\epsilon)$ curve of an O 2p orbital, can be attributed to perturbations of the O 2p orbital by the hydrogens,

leading to hybridization. Table II presents the theoretical $\beta(\varepsilon)$ and experimental difference between $^2B_1$ and $^2A_1$ ionic states of H_2O. Both the experimental and the theoretical average differences $\Delta\beta$ for these two states are ~0.3 β unit. The $X\alpha$ calculation is in excellent agreement with experiment in predicting this molecular bonding effect. Again weak resonance-like structure is found in $\beta(\varepsilon)$ at $h\nu$ = 20 eV and 24 eV.

The $^2B_2$ $(1b_2^{-1})$ cross section is larger than those of the other two states as shown in Fig. 4, which is consistent with a larger difference of this O-H bonding orbital from an O 2p orbital. The $X\alpha$ calculation predicts this result well,[14] while the GIPM curve is low and the ST calculations[18,22] are typically 30-50 percent higher than experiment. Our data agree well with the (e,2e) results[13] and with Dituit, et al.[23] There appears to be two small resonances in our data at ~22 eV and ~25 eV. Williams and Langhoff[18] predict a broad subchannel resonance centered around 25 eV due to transitions into a σ^*a_1 orbital in the continuum, but no maximum appears in the final $\sigma(\varepsilon)$ curve. Cross section measurements of Dituit, et al. seem to confirm that there is structure near 22 eV.[23] The ST calculations of Delaney, et al.[19] also predict a resonance feature near ~23 eV.

The $\beta(\varepsilon)$ parameter for the $^2B_2$ $(1b_2^{-1})$ channel is much lower than for the other two channels and for the O 2p orbital, owing to its strong molecular O-H bonding character. The $\beta(\varepsilon)$ value increases smoothly from -0.1 to 0.6 as $h\nu$ increases from 21 eV to 30 eV. This behavior is well predicted by the $X\alpha$ model, which is in very good agreement at the high-energy end.

C. Conclusions

Several conclusions can be drawn from this work:

1. The $\sigma(\epsilon)$ and $\beta(\epsilon)$ parameters for the $^2B_1$ $(1b_1^{-1})$, $^2A_1$ $(3a_1^{-1})$, and $^2B_2$ $(1b_2^{-1})$ channels in the photoionization of H_2O correspond with the parameters for O 2p orbitals from which these molecular orbital are derived. The $\sigma(\epsilon)$ and $\beta(\epsilon)$ parameters are sensitive to chemical bonding.
2. The $X\alpha$ calculation of Roche, et al. predicts the overall form of $\sigma(\epsilon)$ and $\beta(\epsilon)$ for these orbitals very well.
3. The GIPM calculation of Hilton, et al. predicts $\sigma(\epsilon)$ equally well, on the average.
4. The two available ST calculations predict $\sigma(\epsilon)$ values which tend to be somewhat higher than experiment.
5. Our work agrees well overall with the (e,2e)-derived $\sigma(\epsilon)$ results of Tan, et al.; however, their results do not show any structure.
6. Our measurements show weak resonance-like structure in both $\sigma(\epsilon)$ and $\beta(\epsilon)$, as do the results of Dutuit, et al. There is good qualitative agreement with Dutuit, et al. at photon energies higher than 21 eV.
7. The ST models show resonances in the ionization sub-channels, corresponding to excitation of virtual discrete orbitals imbedded in the continuum. The location of broad continuum resonances predicted by Williams and Langhoff may identify the underlying resonance structure present in our data at 22 eV

for the $^2B_1$, and 25 eV for the $^2A_1$ and $^2B_2$ ionic states calculations of Delaney, et al. give further indication that the ST method may possibly determine resonance structure in the cross sections of the ionic states of H_2O. More experimental and theoretical study is needed to provide a definitive understanding of the usefulness of the ST model in the prediction and identification of resonances in H_2O.

8. Vibrationally resolved measurements of the $^2B_1$, $^2A_1$, and $^2B_2$ ionic states would help in the identification of weak features in the data that are possibly due to autoionization, predissociation, and shape resonances.

References

1. C. N. Yang, Phys Rev. 74, 764 (1948).

2. If direct photodissociation accompanies photoionization, there is more information in the correlation of product properties.

3. K. N. Huang, Phys. Rev. A 22, 223 (1980).

4. V. Rehn, A. D. Baer, J. L. Stanford, D. S. Kyser, and V. O. Jones, in "Vacuum Ultraviolet Physics," edited by E. Koch, R. Haensel, and C. Kunz (Braunschweig, Pergammon-Vieweg, 1974), pp. 780-2.

5. M. G. White, R. A. Rosenberg, G. Gabor, E. D. Poliakoff, G. Thornton, S. H. Southworth, and D. A. Shirley, Rev. Sci. Instrum. 50, 1288 (1979).

6. W. H. Hancock and J. A. R. Samson, J. Electron Spectrosc. Relat. Phenom. 9, 211 (1976); J. Kriele and A. Schweig, J. Electron Spectrosc. Relat. Phenom. 20, 191 (1980).

7. F. Wuilleumier and M. O. Krause, J. Electron Spectrosc. Relat. Phenom. 15, 73 (1978). J. L. Dehmer, W. A. Chupka, J. Berkowitz, and W. T. Jivery, Phys. Rev. A. 12, 1966 (1973).

8. S. Southworth, C. M. Truesdale, P. H. Kobrin, D. W. Lindle, W. D. Brewer, and D. A. Shirley, submitted to J. Chem. Phys. (1981).

9. L. de Reilhac and N. Damany, J. Quant. Spectry. Radiative Transfer 18, 121 (1977).

10. D. H. Katayama, R. E. Huffman, and L. L. O'Bryan, J. Chem. Phys. 59, 4309 (1973).

11. T. A. Carlson and G. E. McGuire, J. Electr. Spectr. Relat. Phonom. 1, 209 (1972-73).

12. S. Katsumata, Y. Achiba, and K. Kimura, J. Electron. Spectrosc. Relat. Phenom. 17, 229 (1979).

13. K. H. Tan, C. E. Brion, Ph. E. van der Leeuw, and M. J. van der Wiel, Chem. Phys. 29, 299 (1973).

14. M. Roche, D. R. Salahub, and P. R. Messmer, J. Elect. Spectr. and Relat. Phenom. 19, 273 (1980).

15. M. S. Banna and D. A. Shirley, J. Chem. Phys. 63, 4759 (1975).

16. J. C. Slater, Adv. Quantum Chem. 6, 1 (1972).

17. D. Dill and J. Dehmer, J. Chem. Phys. 61, 692 (1974).

18. G. R. J. Williams and P. W. Langhoff, Chem. Phys. Letters 60, 201 (1979).

19. P. R. Hilton, S. Nordholm, and N. S. Hush, Chem. Phys. Letters 64, 595 (1979).

20. P. W. Langhoff, Chem. Phys. Letters 22, 60 (1973).

21. T. N. Rescigno, C. F. Bender, B. V. McKoy, and P. W. Langhoff, J. Chem. Phys. 63, 970 (1978).

22. J. J. Delaney, V. R. Saunders, and I. H. Hillier, J. Phys. B. Atom. Molec. Phys. 14, 819 (1981).

23. O. Dutuit, K. Ito, A. Tabche-Foutiale, P. Morinm T. Baer, P. M. Guyon, and I. Nenner, Proc. 6th Int. Conf. of Vacuum Ultraviolet radiation Physics, Charottesville, USA Abstracts 12, 17 (1980).

24. C. Y. R. Wu and D. L. Judge, J. Chem. Phys. 75, 172 (1981).

Table I. Cross sections and asymmetry parameters of the $^2B_1$, $^2A_1$ and $^2B_2$ ionic states of H_2O.

	$^2B_1$		$^2A_1$		$^2B_2$	
hν(eV)	σ(Mb)	β	σ(Mb)	β	σ(Mb)	β
18.	5.60(14)*	.76(5)	6.51(16)	.35(4)	...	...
19.	5.91(15)	.88(5)	5.83(14)	.45(4)	...	...
19.5	5.01(15)	1.18(8)	4.83(14)	.63(6)		
20.	5.24(15)	1.09(6)	4.71(14)	.85(6)	...	...
20.5	5.23(13)	1.08(7)	5.23(13)	.75(5)		
21.2	5.77(14)	.99(8)	5.87(16)	.68(5)	7.03(16)	-.11(3)
	5.9(4)[a]	1.09(4)[a],1.0(1)[b]	6.0(4)[a]	.45(5)[a],.3(1)[b]	8.4(8)[a]	-.09(10)[a],-.1(2)
22	6.06(15)	.96(6)	5.70(15)	.72(5)	8.05(18)	-.10(3)
23	5.92(15)	.96(6)	5.65(14)	.64(5)	7.32(17)	-.06(3)
23.3	5.46(14)	1.06(7)	5.41(14)	.76(6)	7.88(18)	.02(3)
23.5	5.23(13)	1.24(7)	5.00(13)	1.00(5)	6.91(16)	.02(3)
	6.03[c]		5.44[c]		6.63[c]	
24	5.11(14)	1.19(7)	4.77(14)	.85(6)	6.81(17)	.06(3)
24.5	5.23(13)	1.20(7)	4.88(13)	.94(6)	6.69(16)	.20(3)
	5.65[c]		5.30[c]		6.59[c]	
25	6.16(14)	.88(5)	6.00(14)	.75(5)	7.83(17)	.22(3)
26	5.55(15)	1.05(5)	5.03(13)	.90(6)	6.94(17)	.23(4)
27	5.26(13)	1.21(6)	5.45(13)	.80(3)	6.70(15)	.37(4)
28	4.92(14)	1.31(8)	5.14(14)	.85(6)	6.05(15)	.48(5)
29	4.63(13)	1.12(8)	4.66(13)	1.01(7)	5.77(15)	.54(5)
30	4.40(12)	1.38(8)	3.11(13)	1.20(9)	5.43(15)	.55(6)
31	4.38(14)	1.36(9)	3.72(12)	1.21(9)	5.54(15)	.56(5)

*Errors in the last place are given parenthetically.
[a]Reference 12.
[b]Reference 11.
[c]Reference 13.

Table II. Asymmetry parameter differences between the $^2B_1$ and $^2A_2$ ionic states of H_2O.

$h\nu$	$\Delta\beta$(experiment)*	$\Delta\beta$(theory)**
18	.41(4)	.30
20	.24(6)	.30
22	.24(5)	.29
24	.34(6)	.29
26	.15(6)	.25
28	.46(7)	.28
30	.18(8)	.26

*Present results.
**Roche, et al.[14]

Figure Captions

Fig. 1. TOF photoelectron spectrum showing the $^2B_1$, $^2A_1$, and $^2B_2$ ionic states pf H_2O.

Fig. 2. $\sigma(\epsilon)$ and $\beta(\epsilon)$ for the $^2B_1$ $(1b_1^{-1})$. For the $\sigma(\epsilon)$ curves, A is the $X\alpha$ calculation of Roche, et al., B is the GIPM calculation of Hilton, et al., C is the ST calculation of Williams and Langhoff, D is the ST calculation of Delaney, et al., □- are the (e,2e) data of Tan, et al., ■- are the measurements of Dituit, et al., and ⧫ are the present measurements. For the $\beta(\epsilon)$ curves, the solid curve is the $X\alpha$ calculation of Roche, et al. and ⧫ are the present measurements.

Fig. 3. Photoionization cross section $\sigma(\epsilon)$ and photoelectron asymmetry for H_2O^+ $^2A_1$ $(1a_1^{-1})$. The experimental and theoretical results are denoted as in Fig. 2.

Fig. 4. Photoionization cross section $\sigma(\epsilon)$ and photoelectron $\beta(\epsilon)$ for H_2O^+ $^2B_2$ $(1b_2^{-1})$. The experimental and theoretical results are denoted as in Fig. 2.

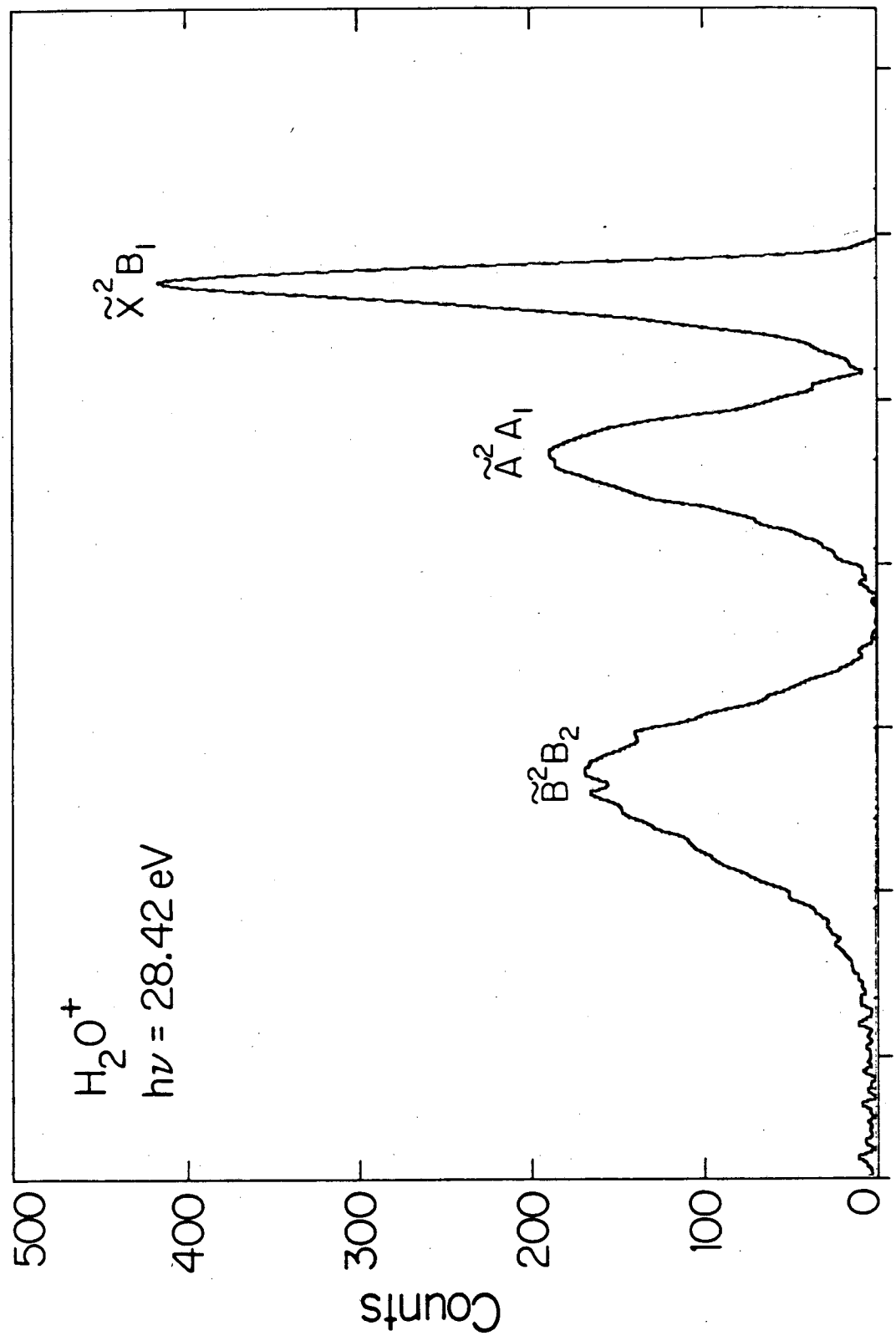

XBL 806-1185

Fig. 2

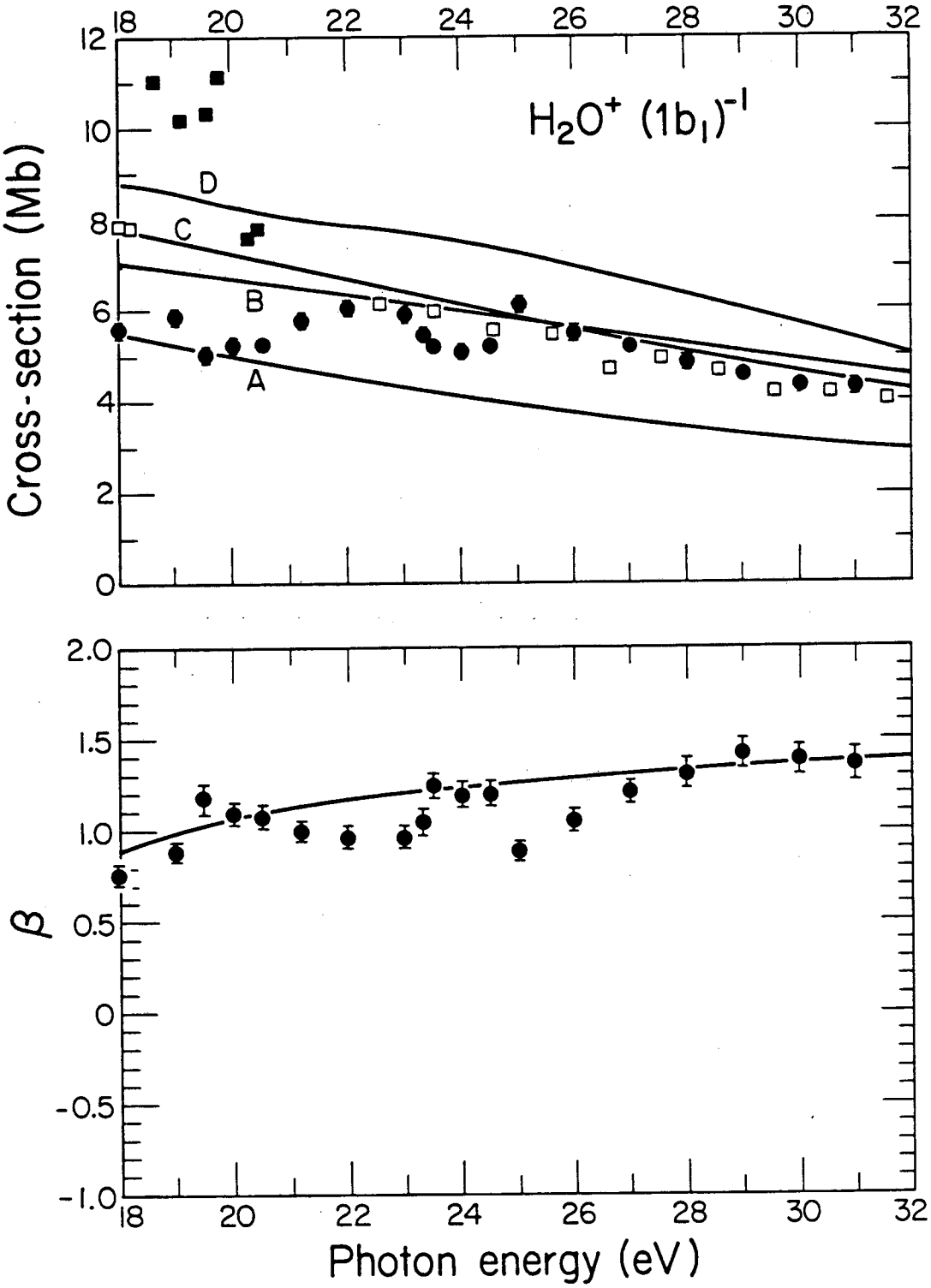
$H_2O^+ (1b_1)^{-1}$
Cross-section (Mb)
D
C
B
A
β
Photon energy (eV)
XBL 818-1224

Fig. 3

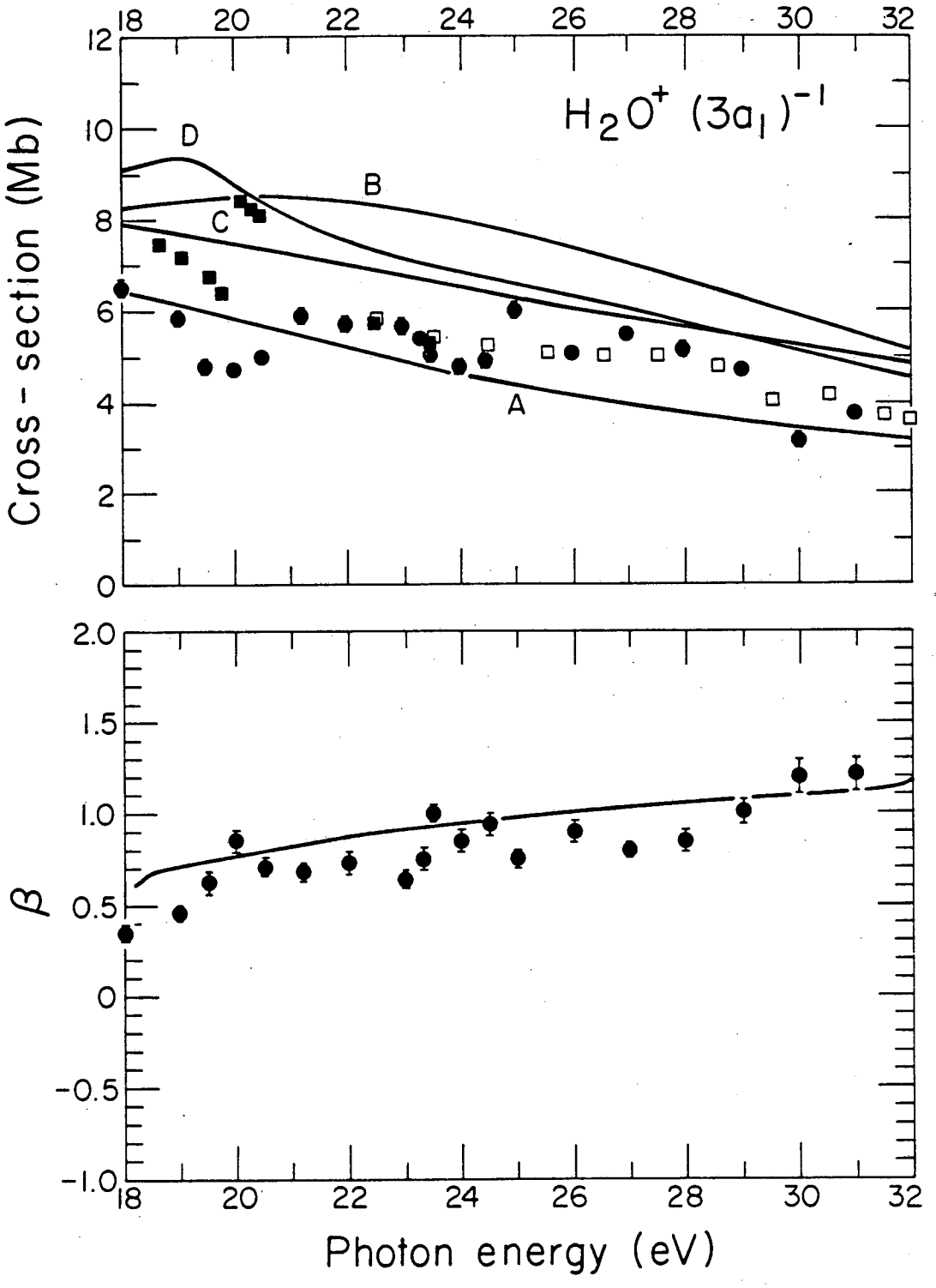

XBL 818-2455

Fig. 3

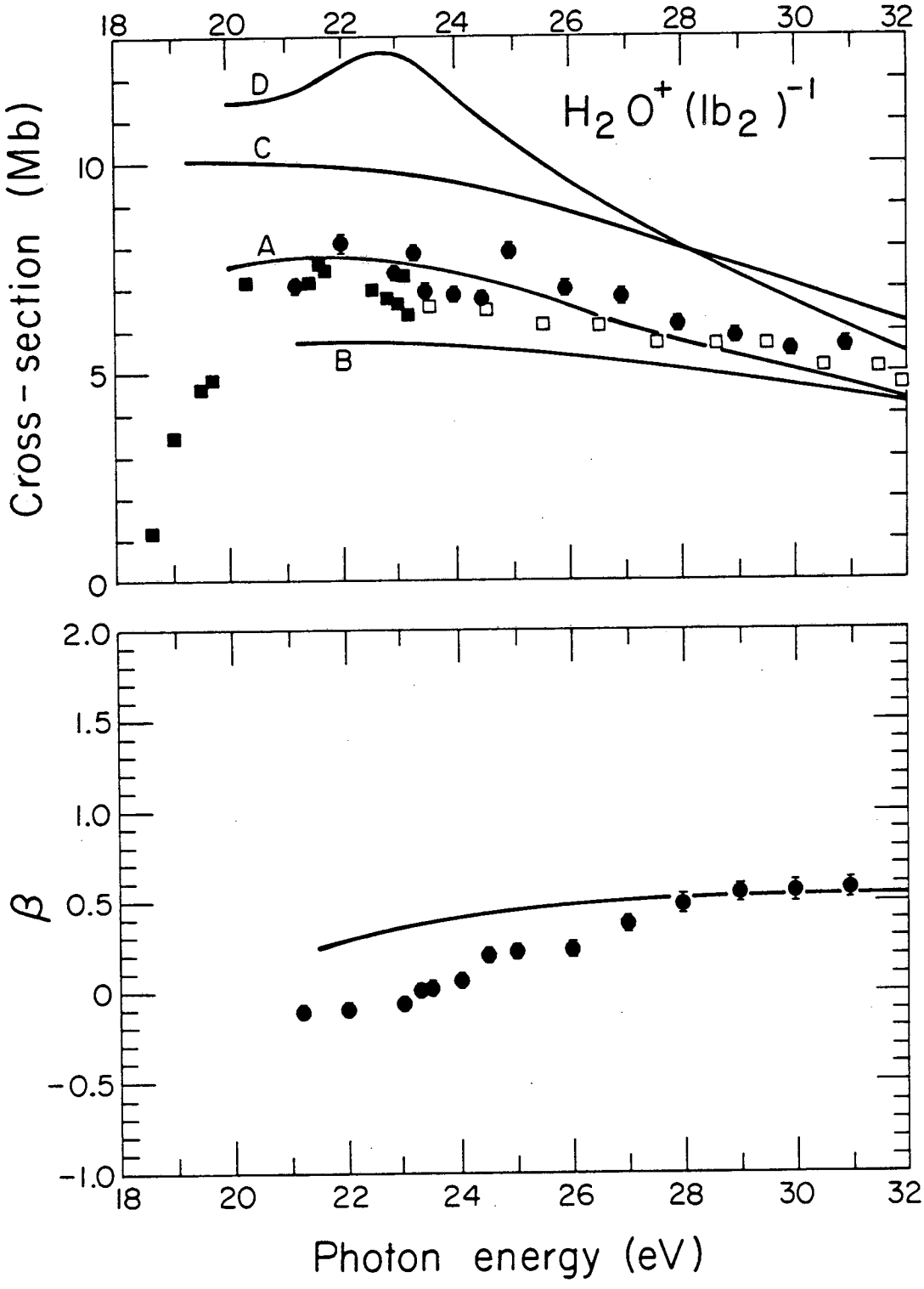

XBL 818-2454

Fig. 4

IV. PHOTOELECTRON ANGULAR DISTRIBUTIONS OF THE N_2O OUTER VALENCE ORBITALS IN THE 19-31 eV PHOTON ENERGY RANGE*

A. Introduction

Photoelectron spectroscopy of the individual molecular orbitals of molecules, using tunable-energy radiation, is in principle capable of yielding a great deal of information about molecular electronic structure. This is a consequence of the fact that the photoionization process is sensitive to dipole amplitudes and asymptotic phases, which in turn depend on both the ionization channel and the molecular field.

It is useful first to write the expression for the differential cross section for (dipole) photoemission from a randomly-oriented sample of molecules irradiated by linearly-polarized light:[1]

$$\frac{d\sigma(\epsilon,\theta)}{d\Omega} = \frac{\sigma(\epsilon)}{4\pi}\left[1 + \beta(\epsilon)P_2(\cos\theta)\right] , \qquad (1)$$

where $P_2(\cos\theta) = (3\cos^2\theta - 1)/2$ is the second Legendre polynomial, θ is the angle between the polarization direction and the photoelectron propagation direction, and ϵ is the photoelectron kinetic energy. If spin is neglected,[2] measurement of both $\sigma(\epsilon)$ and $\beta(\epsilon)$ as functions of ϵ will yield all the measurable information about

---

* C.M. Truesdale, S. Southworth, P.H. Kobrin, D.W. Lindle, and D.A. Shirley, accepted for publication in J. Chem. Phys. (1983).

a given photoionization channel (e.g., ionization from a given molecular orbital). Variation of ε is effected by adjusting the photon energy $h\nu$ from a tunable source, such as synchrotron radiation. The two energies are related by

$$h\nu = \varepsilon + B \qquad (2)$$

for photoionization from an orbital of binding energy B. Thus photoelectron spectroscopy can provide more information than that obtained from more conventional methods, such as absorption spectroscopy, because each photoionization channel with a particular binding energy can be monitored independently. In addition, $\sigma(\varepsilon)$ and $\beta(\varepsilon)$ are sensitive to the molecular potential in different ways.

As yet, the development of variable-energy photoelectron spectroscopy is in a very early stage. On the experimental side, the increasing availability and use of synchrotron radiation is facilitating the acquisition of a rapidly growing body of data. For example, recently reported data on molecules such as H_2O,[3] OCS,[4] CS_2,[4] CO_2,[5] N_2,[6] and O_2 [7] have measured the sensitivity of both $\sigma(\varepsilon)$ and $\beta(\varepsilon)$ to shape resonances, autoionization, and predissociation, as well as confirming the sensitivity of these parameters to the molecular potential.

The theoretical situation is still evolving. Modelling the photoionization process is a challenge to theory if the goal is to provide a reasonably accurate description of $\sigma(\varepsilon)$ and $\beta(\varepsilon)$, while

preserving both computational tractability and a faithful description of physically interesting features in the molecular potentials. Among the models used to date, the multiple scattering method (MSM) seems to describe the photoionization process well. Although it assumes a muffin-tin molecular potential and the results are not always quantitative, it has been very successful in describing the energy dependence of β and σ for some molecular systems.[8] Yet to come are a sufficient number of comparisons between theory and experiment to allow broad conclusions to be drawn concerning the efficacy of various theoretical approaches. Still further away is the stage in which quantitative interpretation of the parameters is feasible, without recourse to careful comparison with theory, to obtain quantitatively useful information.

The photoelectron spectra were obtained using a double-angle time-of-flight spectrometer. A detailed discussion of this instrument has been published.[9] Two detectors, one placed at 0° and another at 54.7° with respect to the polarization axis of the radiation, detect photoelectrons with microchannel plates. A time spectrum of the photoelectrons is collected, and their intensities as functions of kinetic energy are analyzed to yield $\sigma(\epsilon)$ and $\beta(\epsilon)$. All spectra presented here were collected for 1000 seconds. The $\beta(\epsilon)$ parameters are obtained from the intensity ratio of photoelectrons measured at 0° to those measured at 54.7°. The ratios were corrected for the relative efficiency of the two detectors by a calibration procedure which has been explained in detail.[10] Relative partial cross

sections were obtained from the intensity of photoelectrons measured at 54.7°, the "magic angle". At this angle the intensity is independent of the asymmetry parameter. After correcting partial cross sections for the transmission of the 54.7° detector, they were normalized for photon flux and sample density, then scaled to the (e,2e) total cross sections given by Hitchcock et al.[11]

The Stanford Synchrotron Radiation Laboratory provides a tunable ultraviolet radiation source at the 8° beam line. Our measurements used photon energies in the range 18–31 eV. The bandpass of the monochromator was 2.7 Å for these experiments. Additional energy resolution broadening from our spectrometer of ~3 % of the kinetic energy of the photoelectrons increases the overall experimental resolution.

This paper is organized in two more sections: B. Results and Discussion, and C. Conclusions. The body of the paper appears in Section B, in which photoionization of each valence orbital is discussed in turn.

B. Results and Discussion

The ground state electronic configuration of N_2O can be written $(1\sigma)^2(2\sigma)^2(3\sigma)^2(4\sigma)^2(5\sigma)^2(6\sigma)^2(1\pi)^4(7\sigma)^2(2\pi)^4\ {}^1\Sigma^+$. We present the partial cross sections, branching ratios, and asymmetry parameters for ejection of photoelectrons from the 2π, 7σ, 1π, and 6σ orbitals of N_2O, leading respectively to the X, A, B, and C states of N_2O^+. A complete designation of these channels is given by

$$
\begin{aligned}
N_2O(^1\Sigma^+) + h\nu &\rightarrow N_2O^+(X^2\Pi\overline{2\pi}) + e^- \\
&\rightarrow N_2O^+(A^2\Sigma^+\overline{7\sigma}) + e^- \\
&\rightarrow N_2O^+(B^2\Pi\overline{1\pi}) + e^- \\
&\rightarrow N_2O^+(C^2\Sigma^+\overline{6\sigma}) + e^- \quad ,
\end{aligned}
$$

where $\overline{2\pi}$ denotes a hole in the $(2\pi)^4$ configuration, etc. A comment on notation is needed. Because the photoionization process involves both initial and final states, we believe that clarity is best served, at the cost of a little redundancy, by fully specifying "the $X^2\Pi\overline{2\pi}$ channel", etc., throughout.

The mean binding energies of these electronic states are 12.9(X), 16.4(A), 18.3(B), and 20.1(C) eV. A typical spectrum, taken at 24.6 eV photon energy and converted to an energy scale, is shown in Fig. 1. The density of data channels varies with the kinetic energy of the detected photoelectrons as $\epsilon^{-3/2}$. Vibrationally-resolved data for the $A^2\Sigma^+\overline{7\sigma}$ and $C^2\Sigma^+\overline{6\sigma}$ channels are shown in Figs. 2 and 3, respectively. It has been proposed by Domcke[12] that the asymmetry parameter as a function of vibrational state may be used to probe vibronic coupling effects in photoelectron spectra. A simplex algorithm[13] determined the initial estimates for a nonlinear least squares fitting routine, which deconvolute selected spectra. The peak shapes were assumed to be Gaussian. The accuracy of the fitted areas is 10-20%. The variation of the derived partial cross sections and

asymmetry parameters for the vibrational channels is more accurate than an absolute comparison of their values. The assignments of the vibrational modes in N_2O^+ are given by Dehmer et al.[14]

Our results are discussed in the following format. First, the branching ratios of the ionic states referenced to the total cross section are shown in Fig. 4, along with the total cross section. Table I contains a tabulation of the partial cross sections and $\beta(\epsilon)$ for the first four states of N_2O^+. There are four subsections to follow. Section B1 will discuss the $X^2\Pi\overline{2\pi}$ channel, Section B2 the $A^2\Sigma^+\overline{7\sigma}$ channel, Section B3 the $B^2\Pi\overline{1\pi}$ channel, and Section B4 the $C^2\Sigma^+\overline{6\sigma}$ channel.

The other figures fall into two groups. Figs. 7 and 10 show vibrational partial cross sections and asymmetry parameters for the A and C states. They are described in the appropriate subsections. The remaining four figures (5, 6, 8 and 9) display the main results of this work. They all have the same format. The MSM calculations of Whitley and Grimm, which will be discussed in detail in a later publication,[15] are represented by the solid curves for both $\sigma(\epsilon)$ and $\beta(\epsilon)$. The (e,2e) results of $\sigma(\epsilon)$ from Brion and Tan[16] are represented by open circles, and the filled circles represent the present N_2O measurements. The open triangles in the lower panel of Fig. 5 are our recent $\beta(\epsilon)$ results for CO_2, which will be described in detail in a later publication.

The CO_2 results have been corrected for the difference between the binding energies for the X states of CO_2^+ and N_2O^+, in order to compare $\beta(\epsilon)$ at equal kinetic energies. The motivation for

making a comparison between CO_2 and N_2O is that these two molecules are isoelectronic and have similarities in spectral features. The remarkable similarity between the $\beta(\epsilon)$ parameters for the X ionic states of N_2O^+ and CO_2^+ is intriguing — especially so because the molecules are isoelectronic and the two X states both have $^2\Pi$ symmetry. The other three states of N_2O^+ show $\beta(\epsilon)$ values quite similar to those of the A, B, and C states of CO_2^+. However, we are reluctant to draw conclusions from this observation because states of different symmetry must be paired to produce the best match of $\beta(\epsilon)$ values.

B1. The $X^2\Pi\overline{2\pi}$ Channel

McLean and Yoshimine[17] have described the 2π molecular orbital as a combination of $N_1(2p)$ and $O(2p)$ atomic orbitals. Fig. 5 presents the cross section and asymmetry parameter for photoelectrons emitted via ionization of this orbital. The partial cross section indicates a probable maximum at ~19.2 eV and a minimum at 21 eV, superimposed on a monotonically decreasing overall $\sigma(\epsilon)$. Dibeler et al.[18] obtained a photoionization curve for N_2O which shows an autoionizing peak at 19.2 eV that could be due to the population of superexcited, preionized states followed by internal conversion. Eland[19] observed an $(ns\sigma)$ type resonance at ~18.6 eV that appeared strongly in the first four ionic channels.

The MSM calculation agrees only qualitatively with the data in describing the general shape of the decrease in cross section. Our

cross section measurements are in good overall agreement with the (e,2e) results.[16]

The $\beta(\epsilon)$ results for the $X^2\Pi\overline{2\pi}$ channel, also shown in Fig. 5, start at a low value of -0.2 at 19 eV and increase to an asymptotic value of ~0.8 at 30 eV. Because $\sigma(\epsilon)$ does not show any resonance behavior in the high-energy portion of our measurements, Coulomb phase shifts are presumed to be responsible for the gradual variation in $\beta(\epsilon)$.[20] The $X^2\Pi_g\overline{1\pi_g}$ channel in CO_2 is particularly interesting to consider at this point, because it seems to have an almost identical $\beta(\epsilon)$ behavior to that of the $X^2\Pi\overline{2\pi}$ channel in N_2O (Fig. 5, lower panel). The $1\pi_g$ molecular orbital in CO_2 is composed of out-of-phase overlap of the $p\pi$ atomic orbitals on each of the oxygen atoms. Like the N_2O 2π orbital, it is nonbonding with a two-fold degeneracy[21]. The similarity in $\beta(\epsilon)$ is probably a consequence of the similarity in the ionic potentials. The MSM calculation of $\beta(\epsilon)$ for N_2O agrees qualitatively with the present measurements.

B2. The $A^2\Sigma^+\overline{7\sigma}$ Channel

Calculations suggest that the 7σ molecular orbital of N_2O is composed mainly of $N_1(2s)$, $N_2(2p)$, and $O(2p)$ character, and is weakly bonding.[17] The partial cross section for the corresponding $A^2\Sigma^+\overline{7\sigma}$ channel is shown in Fig. 6. The $\sigma(\epsilon)$ data again show a maximum at around 19.2 eV, and a monotonic decrease to 31 eV photon energy. The maximum in the partial cross section could again be due

to an autoionizing resonance, as for the $X^2\Pi\overline{2\pi}$ channel. There is little agreement with the MSM calculation. The (e,2e) results of Brion and Tan are in excellent agreement with the present measurements, except at ~19.2 eV.

The $\beta(\epsilon)$ parameter for the $A^2\Sigma^+\overline{7\sigma}$ channel starts at a low value, near zero, and increases to an asymptotic value of ~1.2. The MSM calculation is in poor agreement with the measured asymmetry parameter. The CO_2 $A^2\Pi\overline{1\pi}_u$ channel $\beta(\epsilon)$ parameter (not shown) matches the N_2O data remarkably well. However, the two channels are very different. The $1\pi_u$ orbital of CO_2 is composed of two perpendicular pairs of $2p\pi$ orbitals on each atom which are overlapping in-phase to form C — O bonding. Thus, if the symmetry assignments of the two A states are correct — and they appear to be correct — the similarity of the two $\beta(\epsilon)$ parameters remains unexplained.

Fig. 2 shows a typical vibrationally-resolved spectrum collected at $h\nu$ = 20 eV plotted linearly in time. Both the log and linear plots were fitted with the simplex and nonlinear least-squares routines. The log plot confirms that there are five vibrational peaks in the spectrum: in particular, the (0,0,2) line is evident. We could not determine $\sigma(\epsilon)$ and $\beta(\epsilon)$ values for the (0,0,2) peak, because of its weak intensity. The four vibrational peaks analyzed correspond to the (0,0,0), (1,0,0), (0,0,1), and the (1,0,1) vibrational modes, with binding energies of 16.40, 16.57, 16.71, and 16.85 eV, respectively.[22] The quantum numbers represent, from left to right, the symmetric, bending, and asymmetric stretch modes.

The derived $\sigma(\epsilon)$ and $\beta(\epsilon)$ values for the vibrationally resolved $A^2\Sigma^+7\sigma$ channel at selected photon energies are presented in Table II. The $\sigma(\epsilon)$ and $\beta(\epsilon)$ values of the (0,0,0), (1,0,0), (0,0,1), and (1,0,1) channels are shown in Fig. 7. The $\beta(\epsilon)$ parameter for the (0,0,1) channel is not plotted for clarity, because it has poor statistical error over most of the 19 to 21 eV photon energy range. The $\sigma(\epsilon)$ and $\beta(\epsilon)$ values for individual members of this vibrational manifold show varied behavior, indicating that more information is available at higher resolution. The vibrationally-unresolved cross section, illustrated in Fig. 6, shows only weak structure in the $h\nu$ = 19-21 eV region, whereas the resolved cross sections show more variation. The unresolved $\beta(\epsilon)$ values tend to smooth out structure because the radial dependencies of the various channels are averaged.[23] Vibrationally-resolved asymmetry parameters could contain information about a whole range of non-Franck-Condon effects, as well as the dependence of $\beta(\epsilon)$ on the internuclear separations in molecules.[24] The consequences of these effects on the asymmetry parameter have been discussed theoretically by Itikawa[25] for non-resonant cases, Dehmer et al.,[26] Stockbauer et al.,[27] and West et al.[28] have studied the shape-resonance effects, and autoionization effects have been discussed by Jungen et al.[29]

B3. The $B^2\Pi 1\pi$ Channel

According to McLean and Yoshimine,[17] the 1π molecular orbital is mostly the result of N-O π bonding with little N-N bonding

character. Our $\sigma(\epsilon)$ and $\beta(\epsilon)$ results are presented in Fig. 8. The partial cross-section data show a low point at 20 eV and a high value at 21.2 eV. The low point may arise through a competing mechanism dissociating this channel. Lorquet and Cadet[30] have calculated potential energy surfaces of N_2O and a correlation diagram of the N_2O ion to show the possible dissociation channels. Their calculations predict an asymptotic dissociation at 20.29 eV above the ground state of N_2O. The process is

$$N_2O^+(B^2\Pi) \rightarrow N_2^+(X^2\Sigma_g^+) + O(^2P^o).$$

More careful measurements near 20 eV are warranted. The MSM calculation predicts $\sigma(\epsilon)$ values that are about 50 lower than the present results and that show a different energy dependence. Again, there is good agreement between our data and the (e,2e) results.

The $\beta(\epsilon)$ values show variations at ~22 eV and below which could arise from the same causes as the variations in $\sigma(\epsilon)$. The asymmetry parameter $\beta(\epsilon)$ starts at a low value, near zero, and increases to unity. There is only fair agreement with the MSM calculation of Whitley et al.[15] The $C^2\Sigma_g^+\overline{4\sigma}_g$ results for $\beta(\epsilon)$ in CO_2 (not shown) are in fair to good agreement with $\beta(\epsilon)$ for the $B^2\Pi\overline{1\pi}$ channel in N_2O. However, we are again reluctant to draw any conclusions from this similarity because the states have different symmetries.

B4. The $C^2\Sigma^+\overline{6\sigma}$ Channel

The 6σ molecular orbital is a combination of N-O and N-N antibonding s-like orbitals.[17] The partial cross sections and asymmetry parameters for this channel are shown in Fig. 9. The cross section varies slowly over the entire photon energy range, and there is no evidence of resonances. The agreement between the behavior of the calculated MSM partial cross sections and the present results is poor, but once again there is excellent agreement with the (e,2e) measurements.

The asymmetry parameter for the $C^2\Sigma^+\overline{6\sigma}$ channel shows a steep increase from -0.5 at 21 eV to 1.0 at 31 eV, with most of the rise occurring between 24 and 27 eV. The variation of $\beta(\varepsilon)$ for this channel is very different than that of the first three channels. As was the case for $\sigma(\varepsilon)$, there is poor agreement between the MSM calculation of $\beta(\varepsilon)$ and our results. However, the $\beta(\varepsilon)$ data for the $B^2\Sigma_u^+\overline{3\sigma_u}$ channel in CO_2 (not shown) follow these data quite closely. The $3\sigma_u$ molecular orbital of CO_2, according to Mulligan,[31] is also nearly nonbonding, with "sp" oxygen character. Hybridized 2s and 2p orbitals on the oxygen atoms overlap a $2p\sigma$ orbital on the carbon atom.

Fig. 3 shows the partially-resolved vibrational peaks observed in the time-of-flight spectra for the $C^2\Sigma^+\overline{6\sigma}$ channel. There are three peaks, corresponding to the (0,0,0), (1,0,0), and (0,0,1) channels, with binding energies of 20.15, 20.30, and 20.43 eV, respectively.[22] The $\sigma(\varepsilon)$ and $\beta(\varepsilon)$ values for these peaks are shown in Fig. 10.

Partial cross sections and asymmetry parameters are tabulated in Table III. The $\beta(\epsilon)$ results do not show any resonance behavior, but they vary over a large range, and $\beta(\epsilon)$ for the (1,0,0) vibrational mode is near -1 for the entire region measured.

C. Conclusions

The main conclusions of this work are as follows:

1. The partial photoelectron cross sections and asymmetry parameters for the first four ionic states of N_2O were measured. They were found to be substantially different for the X, A, B, and C ionic states, demonstrating the sensitivity of $\sigma(\epsilon)$ and $\beta(\epsilon)$ to details of the different channels sampling the molecular potential.

2. Resolved measurements of $\sigma(\epsilon)$ and $\beta(\epsilon)$ for individual vibrational levels in the A and C states showed large variations with vibrational quantum numbers, demonstrating high sensitivity to non-Franck-Condon effects and/or internuclear spacing.

3. The published (e,2e) partial cross sections of Brion and Tan are in good or excellent agreement with the present results.

4. There is a close empirical, pairwise correspondence between the $\beta(\epsilon)$ values for the molecular orbitals of CO_2 and N_2O. The correspondence is between the CO_2 $X^2\Pi_g\overline{1\pi}_g$ and N_2O $X^2\Pi\overline{2\pi}$, CO_2 $A^2\Pi_u\overline{1\pi}_u$ and N_2O $A^2\Sigma^+\overline{7\sigma}$, CO_2 $C^2\Sigma_g^+\overline{4\sigma}_g$ and N_2O $B^2\Pi\overline{1\pi}$, and CO_2 $B^2\Sigma_u^+\overline{3\sigma}_u$ and N_2O $C^2\Sigma^+\overline{6\sigma}$ ionic states. The significance of this observation is unclear. In the first and last pairs, states of the same symmetry are matched, but the other two pairs involve states of opposite symmetry.

5. Better calculations are needed to describe the measured asymmetry parameters and partial cross sections.

References

1. C.N. Yang, Phys. Rev 74, 764 (1948).

2. K.N. Huang, Phys. Rev A. 22, 223 (1980).

3. C.M. Truesdale, S. Southworth, P.H. Kobrin, D.W. Lindle, G. Thornton, and D.A. Shirley, J. Chem. Phys. 76, 860 (1982).

4. T.A. Carlson, M.O. Krause, and F.A. Grimm, J. Chem. Phys. 77, 1701 (1982).

5. T.A. Carlson, M.O. Krause, F.A. Grimm, J.D. Allen, D. Mehaffy, P.R. Keller, and J.W. Taylor, Phys. Rev. A. 23, 3316 (1981); F.A. Grimm, J.D. Allen, Jr., T.A. Carlson, M.O. Krause, D. Mehaffy, P.R. Keller, and J.W. Taylor, J. Chem, Phys. 75, 92 (1981).

6. A.C. Parr, D.L. Ederer, B.E. Cole, J.B. West, R. Stockbauer, K. Codling, J.L. Dehmer, Phys. Rev. Lett. 46, 22 (1981).

7. P. Morin, I. Nenner, M.Y. Adam, M.J. Hubin-Franskin, J. Delwiche, H. Lefebvre-Brion, and A. Giusti-Suzor, Chem. Phys. Lett. 92, 609 (1982); P. Morin, I. Nenner, P.M. Guyon, L.F.A. Ferreira, and K. Ito, Chem. Phys. Lett. 92, 103 (1982).

8. M. Roche, D.R. Salahub, and P.R. Messmer, J. Electron Spectrosc. Relat. Phenom., 17, 229 (1979).

9. M.G. White, R.A. Rosenberg, G. Gabor, E.D. Poliakoff, G. Thornton, S.H. Southworth, and D.A. Shirley, Rev. Sci. Instrum. 50, 1288 (1979).

10. S. Southworth, C.M. Truesdale, P.H. Kobrin, D.W. Lindle, W.D. Brewer, and D.A. Shirley, J. Chem. Phys. 76, 143 (1982).

11. A.P. Hitchcock, C.E. Brion, and M.J. van der Wiel, Chem. Phys. 45, 461 (1980).

12. W. Domcke, Physica Scripta 19, 11 (1979).

13. J.A. Nelder and R. Mead, Computer J. 7, 308 (1965); R. O'Neill, Applied Statistics 20, 338 (1971).

14. P.M. Dehmer, J.L. Dehmer, and W.A. Chupka, J. Chem. Phys. 73, 126 (1980).

15. Private communication with T.A. Carlson; T.A. Carlson, P.R. Keller, J.W. Taylor, T.A. Whitley, and F.A. Grimm, to be published.

16. C.E. Brion and K.H. Tan, J. Electron Spectrosc. Relat. Phenom. 15, 241 (1979).

17. A.D. McLean and M. Yoshimine, Tables of Linear Molecular Wave Functions, IBM Corp., San Jose Calif., 1967.

18. V.H. Dibeler, J.A. Walker, and S.K. Liston, J. Res. Natl. Bur. Stands., 71A, 371 (1967).

19. J.H. Eland, Mol. Phys. 40, 917 (1980).

20. W. Thiel, Chem. Phys. Lett. 87, 249 (1982).

21. A.D. Walsh, J. Chem. Soc. 2266 (1953).

22. C.R. Brundle and D.W. Turner, Int. J. Mass Spectry. Ion Physics 2, 195 (1969).

23. J.R. Swanson, D. Dill, and J.L. Dehmer, J. Phys. B: At. Mol. Phys. 14, L207 (1981).

24. J.W. Rabalais, Principles of Ultraviolet Photelectron Spectroscopy p. 194 Wiley-Interscience, 1977.

25. Y. Itikawa, Chem. Phys. Lett. 62, 261 (1979); Y. Itikawa, Chem. Phys. 37, 401 (1979).

26. J.L. Dehmer, D. Dill, and S. Wallace, Phys. Rev. Lett. 43, 1005 (1979).

27. R. Stockbauer, B.E. Cole, D.L. Ederer, J.B. West, A.C. Parr, and J.L. Dehmer, Phys. Rev. Lett. 43, 757 (1979).

28. J.B. West, A.C. Parr, B.E. Cole, D.L. Ederer, R. Stockbauer, and J.L. Dehmer, J. Phys B 13, L105 (1980).

29. Ch. Jungen and O. Altebek, J. Chem. Phys. 66, 5584 (1977); Ch. Jungen and D. Dill, J. Chem. Phys. 73, 3338 (1980).

30. J. C. Lorquet and C. Cadet, Int. J. Mass Spectry. Ion Physics 7, 245 (1971).

31. J.F. Mulligan, J. Chem. Phys. 32, 1595 (1951).

32. T.A. Carlson and G.E. Mc Guire, J. Electron Spectrosc. Relat. Phenom. 1, 209 (1972).

Table I. Cross sections and asymmetry parameters of the X, A, B, and C Channels of N_2O^+.

	$X^2\Pi 2\sigma$		$A^2\Sigma^+ 7\sigma$		$B^2\Pi 1\pi$		$C^2\Sigma^+ 6\sigma$	
hν(eV)	σ(Mb)[a]	β(ε)	σ(Mb)	β(ε)	σ(Mb)	β(ε)	σ(ε)	β(ε)
19.0	15.29(34)[b]	0.24(2)	12.09(28)	0.07(1)				
19.2	17.00(40)	-0.15(3)	15.57(37)	0.00(3)	8.89(22)	0.20(4)		
20.0	15.64(35)	-0.12(2)	10.90(25)	0.20(3)	7.89(18)	0.22(3)		
20.5	14.30(32)	-0.06(3)	9.12(21)	0.39(4)	10.17(23)	0.18(3)		
21.2	12.27(27)	-0.03(3)	8.76(21)	0.43(1)	11.48(27)	0.11(3)	6.70(16)	-0.36(2)
		0.0(1)[c]		0.35(10)[c]		-0.2(2)[c]		-0.4(2)[c]
21.8	13.03(30)	0.15(3)	6.30(15)	0.67(5)	10.26(25)	0.48(4)	5.94(14)	-0.26(2)
23.0	14.18(31)	0.32(3)	6.34(15)	0.81(2)	10.28(24)	0.45(4)	6.24(12)	-0.17(2)
24.0	13.12(29)	0.41(4)	5.55(13)	0.90(3)	9.93(23)	0.58(4)	5.70(14)	-0.13(3)
25.0	13.74(30)	0.50(4)	4.59(12)	1.00(3)	10.01(24)	0.73(5)	5.39(13)	0.13(3)
26.0	12.52(28)	0.61(4)	4.27(11)	1.06(3)	9.31(22)	0.85(5)	4.61(12)	0.45(5)
27.0	12.70(31)	0.68(5)	4.38(13)	1.07(6)	8.49(22)	1.08(7)	4.58(13)	0.80(7)
28.0	12.29(22)	0.86(5)	4.23(10)	1.15(7)	8.46(19)	1.00(6)	3.67(9)	0.87(6)
29.0	11.27(29)	0.76(5)	4.88(15)	1.03(4)	8.56(22)	1.06(7)	3.13(10)	0.90(7)
29.5	8.80(22)	0.88(6)	3.83(11)	1.17(8)	7.61(19)	1.01(6)	3.04(12)	0.95(7)
31.0	9.87(31)	0.78(6)	4.37(18)	1.16(5)	7.92(25)	1.09(9)	3.26(15)	0.96(10)

(a) Absolute cross sections were obtained by scaling to (e,2e) data (Ref. 11).
(b) Errors in the last place are given parenthetically.
(c) Ref. 32.

Table II. Cross sections and asymmetry parameters of the $A^2\Sigma^+ 7\sigma$ vibrational channels of N_2O^+.

	(0,0,0)		(1,0,0)		(0,0,1)		(1,0,1)	
hν(eV)	σ(Mb)[a]	β(ε)	σ(Mb)	β(ε)	σ(Mb)	β(ε)	σ(Mb)	β(ε)
19.0	7.42(16)	0.16(3)	3.39(16)	0.04(5)	0.72(7)	0.76(9)	0.55(13)	-.45(7)
19.2	9.33(34)	0.11(3)	4.91(35)	-0.34(5)	0.94(19)	0.70(25)	0.39(5)	.02(12)
20.0	6.12(47)	0.36(2)	3.46(47)	-0.30(10)	1.09(40)	0.23(45)	0.21(2)	.28(16)
20.5	5.37(38)	0.76(11)	3.61(40)	-0.21(8)	0.52(10)	0.90(36)	0.42(11)	.18(36)
21.2	5.86(12)	0.57(3)	1.78(8)	0.61(9)	0.76(4)	0.49(15)	0.35(4)	.02(26)
		0.35[b]		0.45(5)[b]		0.20(20)[b]		

(a) The total cross section was obtained by scaling to (e,2e) data (Ref. 11).
(b) Ref. 32.

Table III. Cross sections and asymmetry parameters of the $C^2\Sigma^+\overline{6\sigma}$ vibrational channels of N_2O^+.

	(0,0,0)		(1,0,0)		(0,0,1)	
hν(eV)	σ(Mb)[a]	β(ε)	σ(Mb)	β(ε)	σ(Mb)	β(ε)
23.0	4.05(10)	.36(3)	1.32(7)	-.75(4)	0.88(7)	-.51(6)
24.0	3.53(38)	.15(11)	1.17(24)	-.72(6)	1.38(17)	-.46(9)
25.0	3.45(38)	.57(12)	1.65(70)	-.70(13)	1.35(23)	-.18(12)
26.0	3.14(23)	.80(5)			1.47(18)	-.17(11)

(a) The total cross section was obtained by scaling to (e,2e) data (Ref. 11).

Figure Captions

Figure 1. TOF photoelectron spectrum showing the $X^2\Pi\overline{2\pi}$, $A^2\Sigma^+\overline{7\sigma}$, $B^2\Pi\overline{1\pi}$, and $C^2\Sigma^+\overline{6\sigma}$ ionic states of N_2O^+.

Figure 2. TOF photoelectron spectrum showing the $A^2\Sigma^+\overline{7\sigma}$ vibrational states of N_2O^+. The curves in the linear spectrum are deconvoluted peaks from nonlinear least-squares fits. The curve in the log plot represents the sum of deconvoluted peaks calculated with the same fitting method.

Figure 3. TOF photoelectron spectrum showing the $C^2\Sigma^+\overline{6\sigma}$ vibrational states of N_2O. The curves are the deconvoluted peaks as in Fig. 2.

Figure 4. Branching ratios to the ionic states in N_2O^+, and total photoionization cross section of N_2O. The symbols represent states as follows: X(△), A(○), B(■), and C(□). All are referenced to our total cross-section measurements, denoted by ●. The ▲ are (e,2e) total cross-section measurements of Brion and Tan.[16]

Figure 5. The $\sigma(\epsilon)$ and $\beta(\epsilon)$ results for the $X^2\Pi\overline{2\pi}$ ionic state. The present results are plotted as filled circles. The curves are the MSM calculations of Whitley and Grimm.[15] Open circles in the $\sigma(\epsilon)$ plot are the (e,2e) results of Brion and Tan.[16] Open triangles in the $\beta(\epsilon)$ panel are our measurements on the $X^2\Pi_g\overline{1\pi}_g$ state of CO_2. The CO_2 results were adjusted by 0.9 eV to compare equal kinetic energies.

Figure 6. The $\sigma(\epsilon)$ and $\beta(\epsilon)$ results for the $A^2\Sigma^+\overline{7\sigma}$ ionic state. The notation is similar to Fig. 5.

Figure 7. Vibrational resolved $\sigma(\epsilon)$ and $\beta(\epsilon)$ of the $A^2\Sigma^+\overline{7\sigma}$ ionic state.

Figure 8. The $\sigma(\epsilon)$ and $\beta(\epsilon)$ values for the $B^2\Pi\overline{1\pi}$ ionic state. The notation is similar to Fig. 5.

Figure 9. The $\sigma(\epsilon)$ and $\beta(\epsilon)$ values for the $C^2\Sigma^+\overline{6\sigma}$ ionic state. The notation is similar to Fig. 5.

Figure 10. Vibrational resolved $\sigma(\epsilon)$ and $\beta(\epsilon)$ of the $C^2\Sigma^+\overline{6\sigma}$ ionic state.

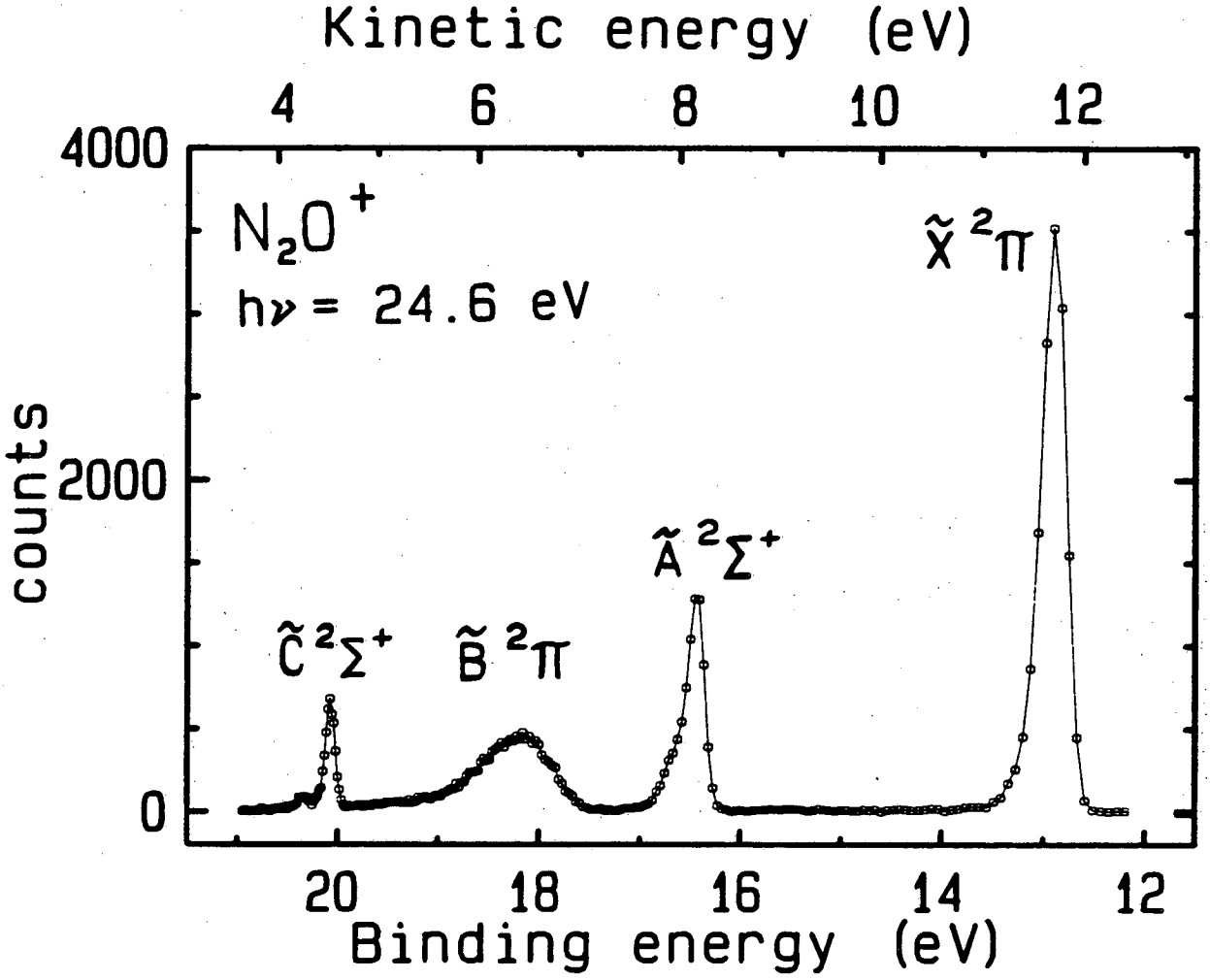

XBL 8212-12248

Fig. 1

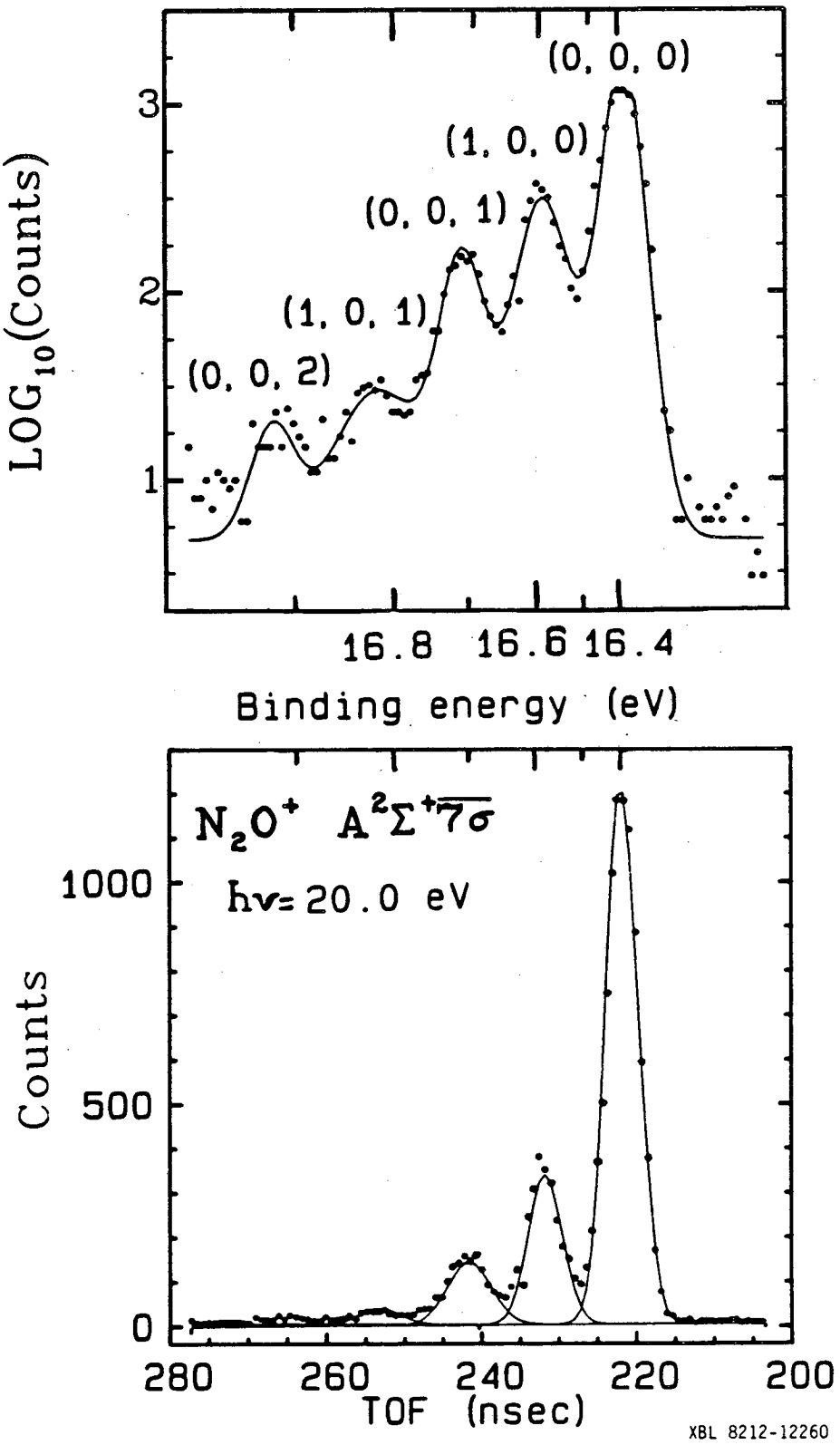
(0, 0, 0)
(1, 0, 0)
(0, 0, 1)
(1, 0, 1)
(0, 0, 2)
LOG10(Counts)
3
2
1
16.8 16.6 16.4
Binding energy (eV)
N2O+ A2Σ+ 7σ
hν= 20.0 eV
1000
500
0
Counts
280 260 240 220 200
TOF (nsec)
XBL 8212-12260

Fig. 2

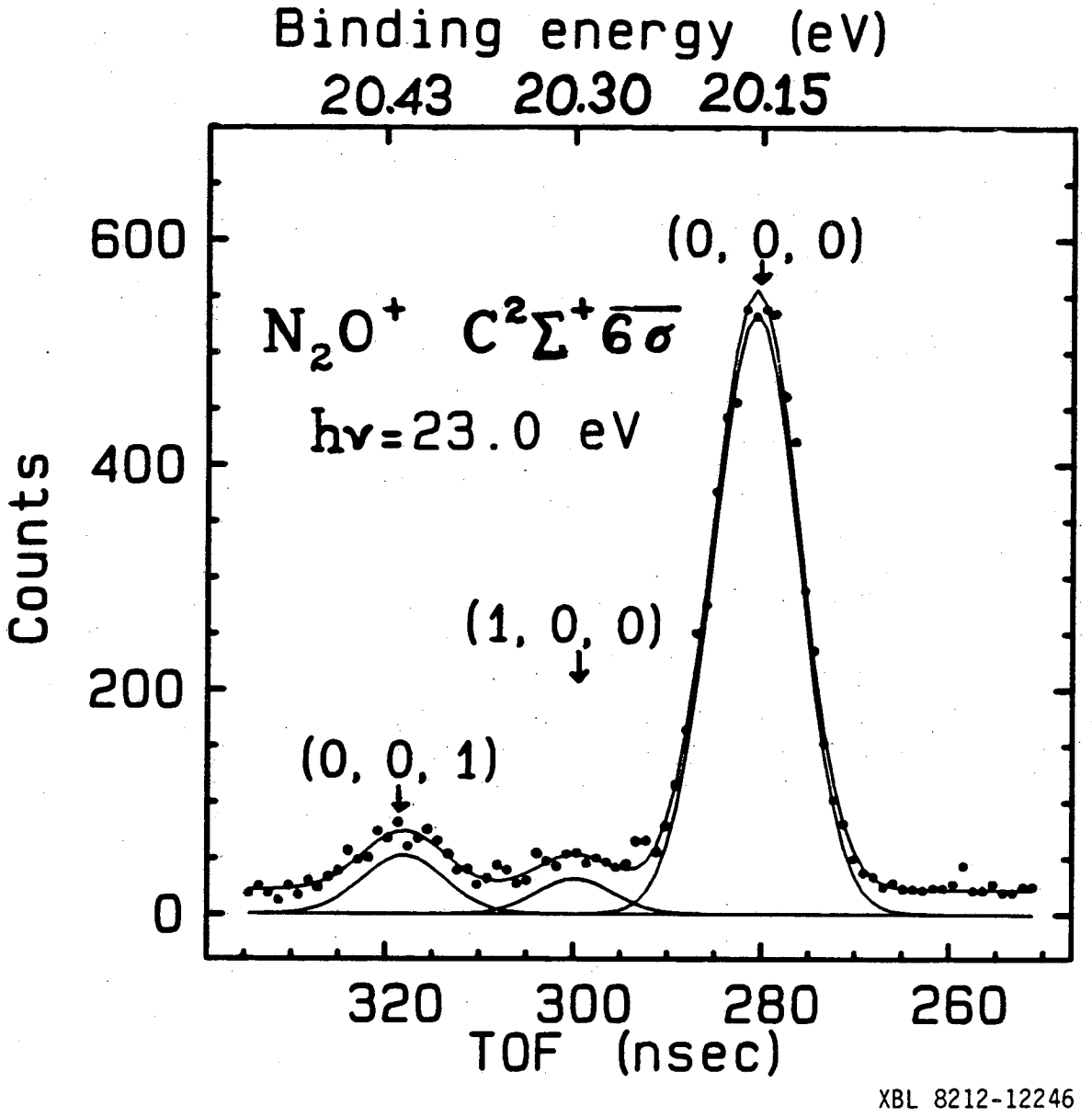

XBL 8212-12246

Fig. 3

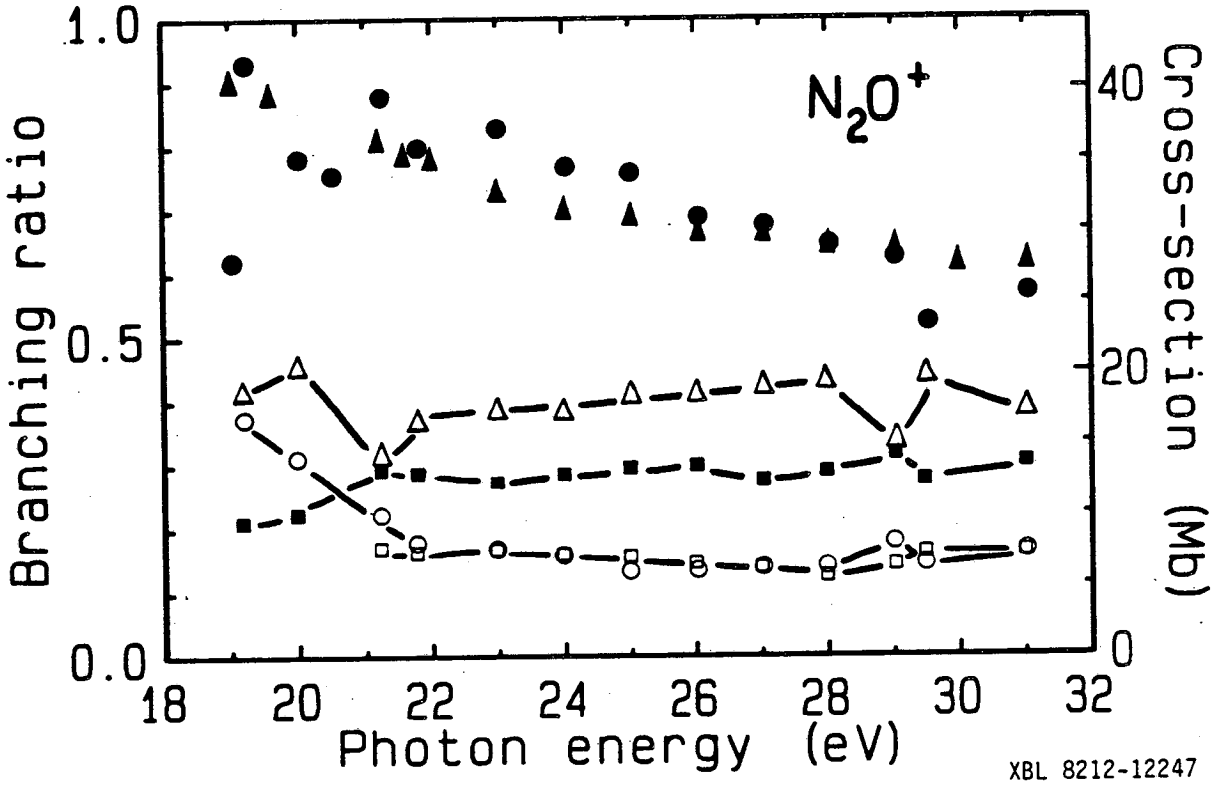
1.0
0.5
0.0
Branching ratio
N_2O^+
40
20
0
Cross-section (Mb)
18
20
22
24
26
28
30
32
Photon energy (eV)
XBL 8212-12247

Fig. 4

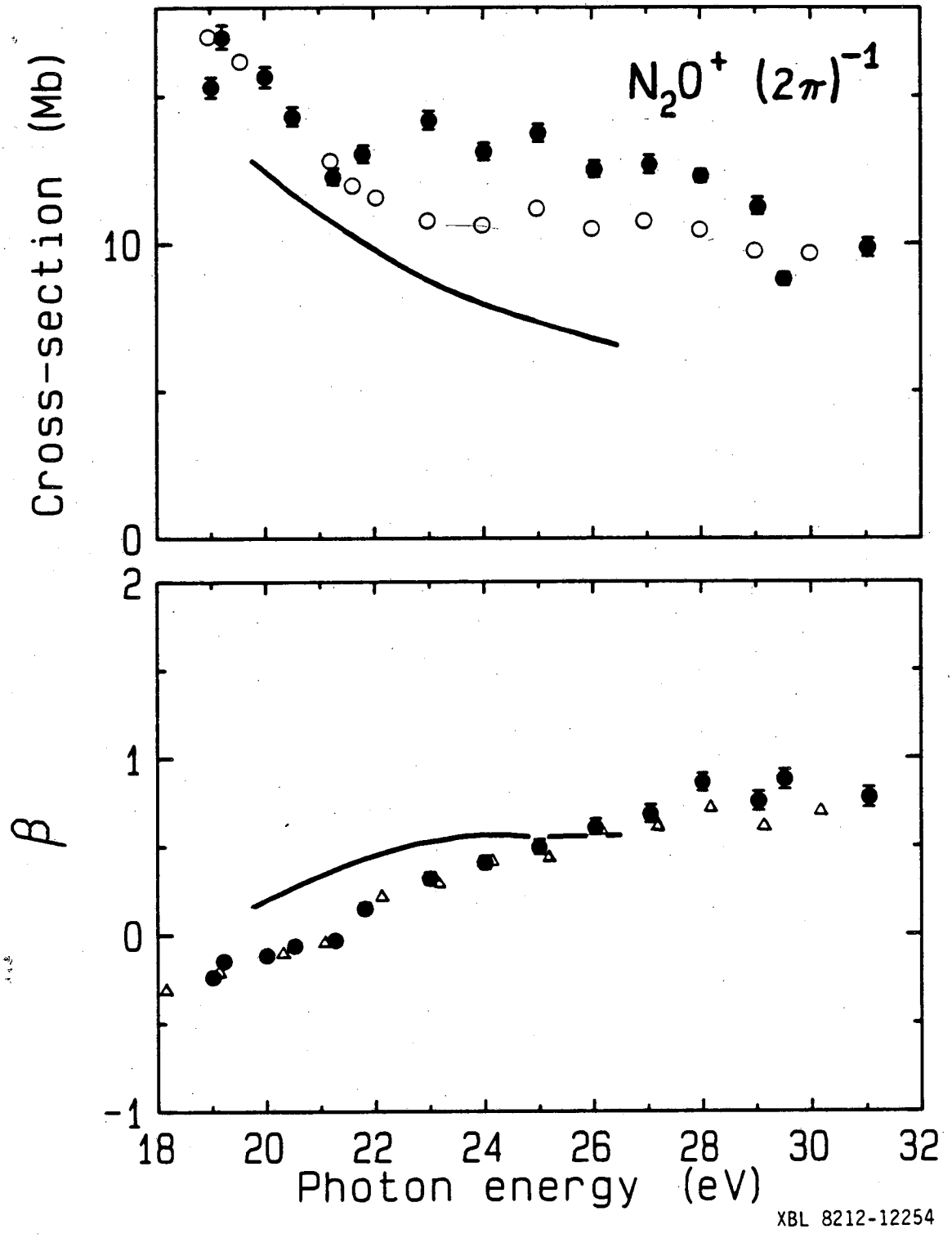
Cross-section (Mb)
N_2O^+ $(2\pi)^{-1}$
10
0
2
1
0
-1
β
18
20
22
24
26
28
30
32
Photon energy (eV)
XBL 8212-12254

Fig. 5

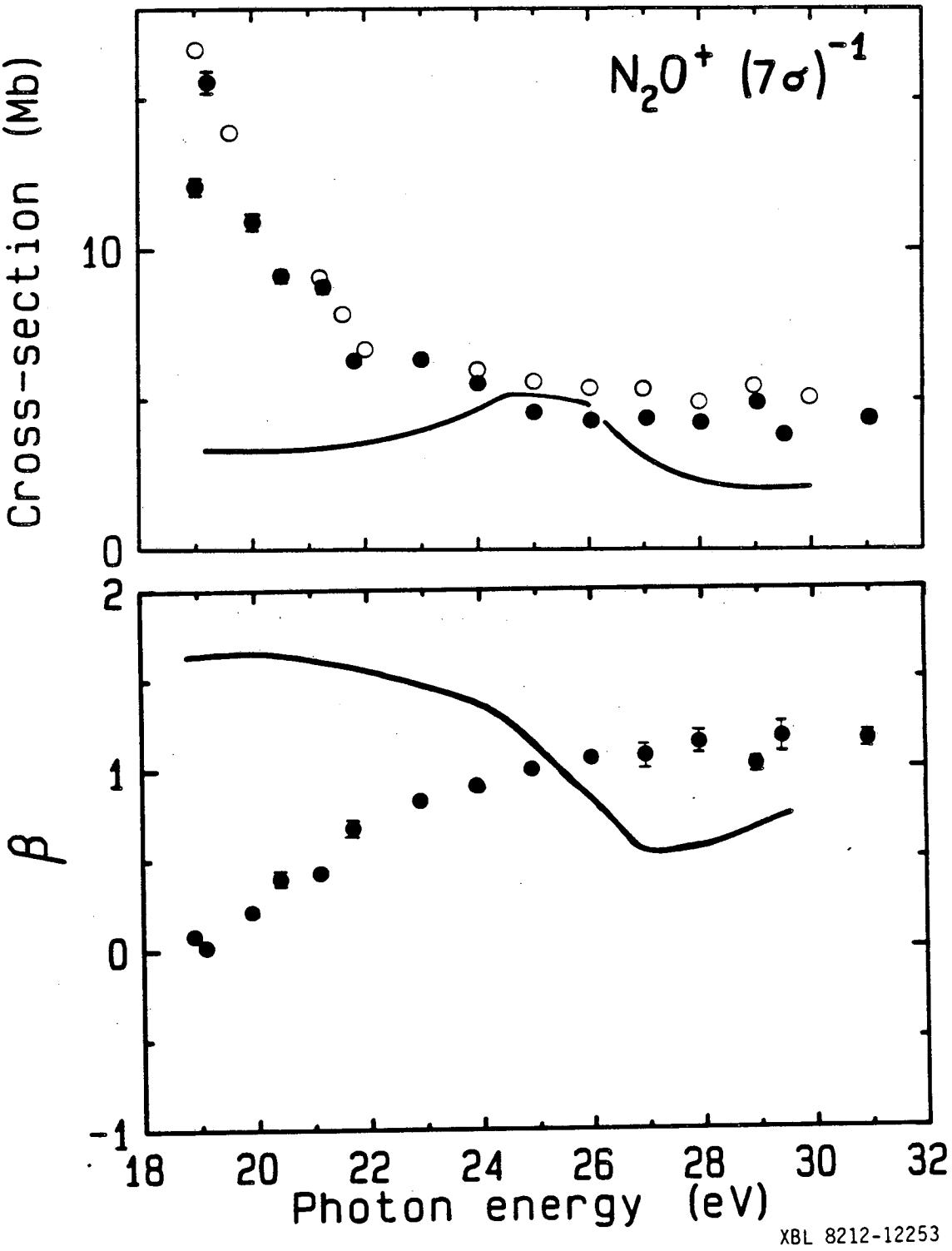
$N_2O^+ (7\sigma)^{-1}$
Cross-section (Mb)
10
0
2
1
0
-1
β
18
20
22
24
26
28
30
32
Photon energy (eV)
XBL 8212-12253

Fig. 6

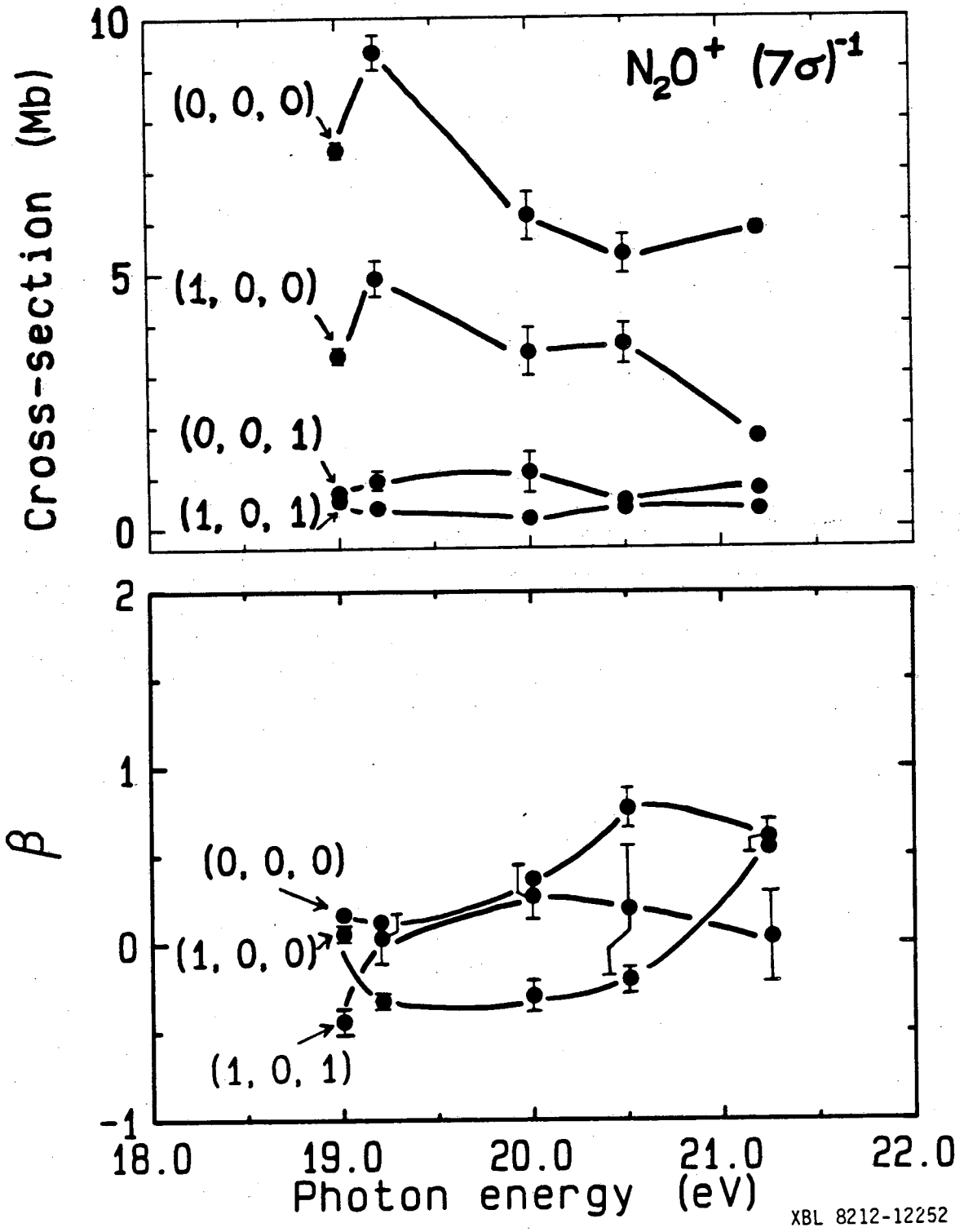
Cross-section (Mb)
10
5
0
N_2O^+ $(7\sigma)^{-1}$
(0, 0, 0)
(1, 0, 0)
(0, 0, 1)
(1, 0, 1)
β
2
1
0
-1
(0, 0, 0)
(1, 0, 0)
(1, 0, 1)
18.0
19.0
20.0
21.0
22.0
Photon energy (eV)
XBL 8212-12252

Fig. 7

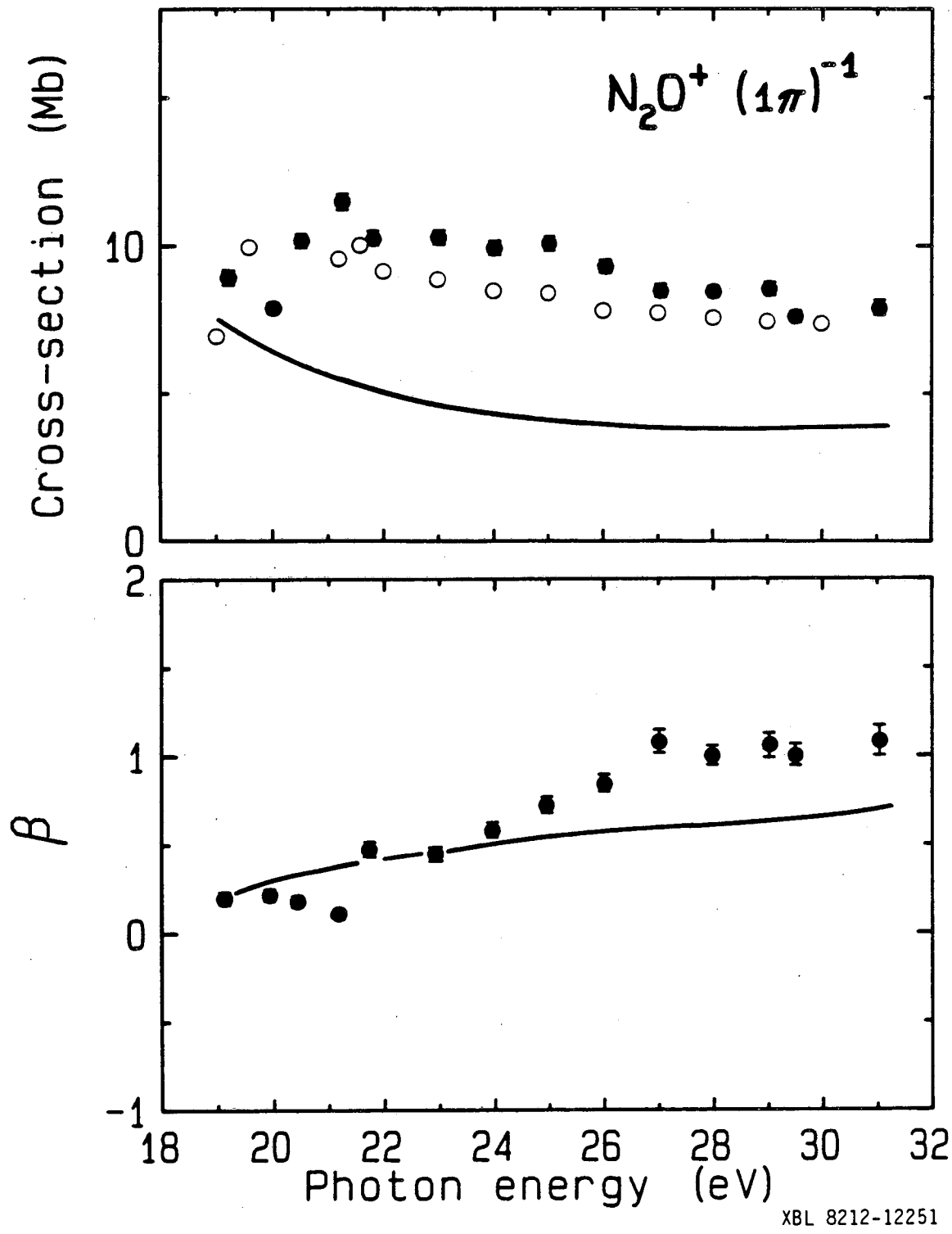
N_2O^+ $(1\pi)^{-1}$
Cross-section (Mb)
10
0
2
1
0
-1
β
18
20
22
24
26
28
30
32
Photon energy (eV)
XBL 8212-12251

Fig. 8

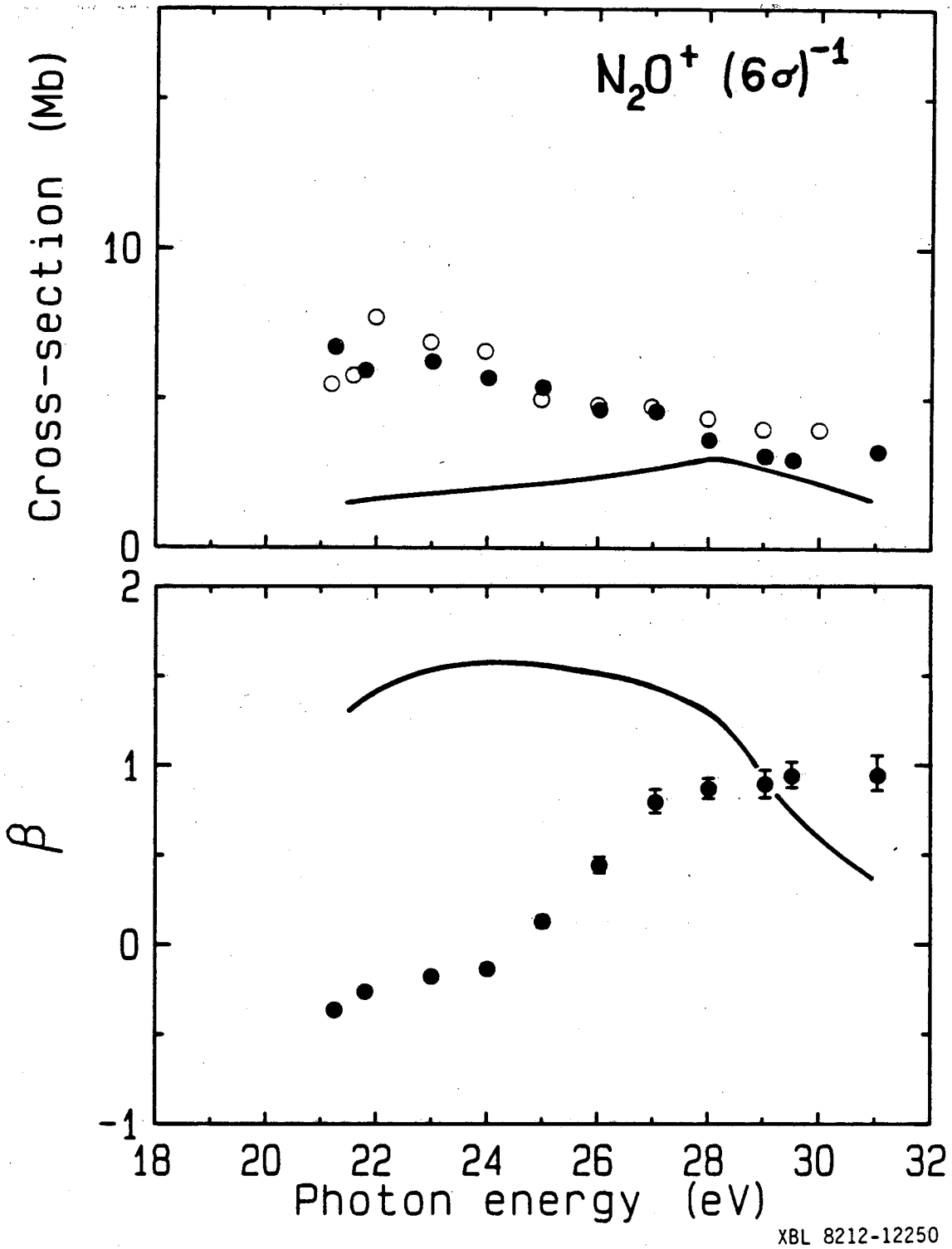
$N_2O^+ (6\sigma)^{-1}$
Cross-section (Mb)
10
0
2
1
0
-1
β
18
20
22
24
26
28
30
32
Photon energy (eV)
XBL 8212-12250

Fig. 9

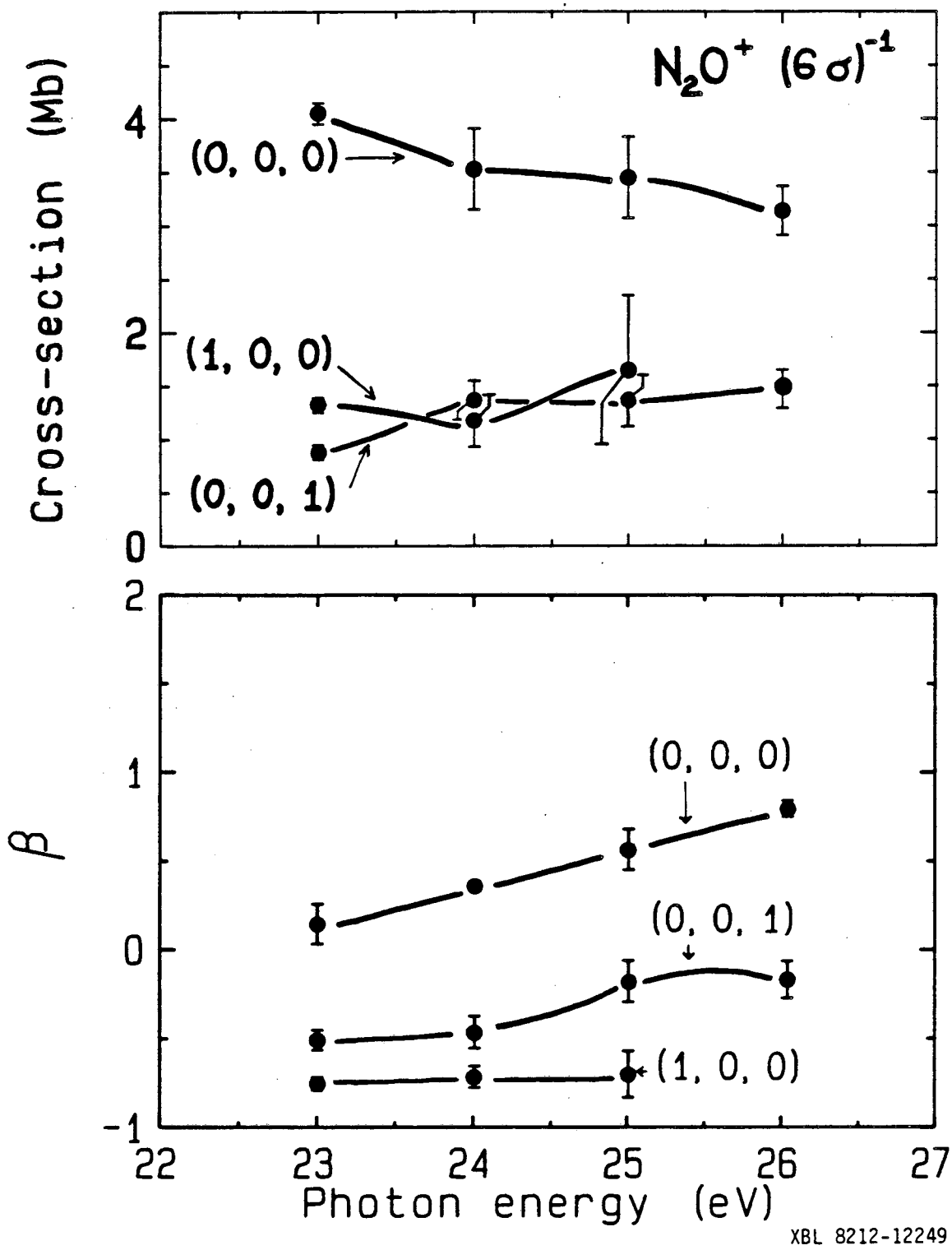
N_2O^+ $(6\sigma)^{-1}$
Cross-section (Mb)
(0, 0, 0)
(1, 0, 0)
(0, 0, 1)
β
(0, 0, 0)
(0, 0, 1)
(1, 0, 0)
Photon energy (eV)
XBL 8212-12249

Fig. 10

V. VIBRATIONALLY ANGLE-RESOLVED PHOTOELECTRON STUDIES OF CO_2 AND OCS*

A. Introduction

Studies of the vibrational levels via photoionization can provide information about internuclear-distance dependent structure[1] and non-Franck-Condon behavior[1-4] for the vibrational intensity distribution and photoelectron asymmetry parameters. The asymmetry parameter $\beta(\epsilon)$, which describes the angular distribution of photoelectrons, is related to the differential cross section $d\sigma/d\Omega$, by[5]

$$\frac{d\sigma(\epsilon,\theta)}{d\Omega} = \frac{\sigma(\epsilon)}{4\pi}[\ 1 + \beta(\epsilon)P_2(\cos\theta)\ ] \quad . \tag{1}$$

Here $P_2(\cos\theta)$ is the second Legendre polynomial $[(3\cos^2\theta-1)/2]$ and θ is the angle of photoelectron emission referenced to the photon beam polarization direction. The total cross section $\sigma(\epsilon)$ and the asymmetry parameter $\beta(\epsilon)$ are functions of the photoelectron kinetic energy ϵ. Two time-of-flight (TOF) detectors, placed at $\theta = 0^\circ$ and 54.7°, can be used to analyze ejected photoelectrons. From equation (1), measurements at these two angles suffice to determine $\sigma(\epsilon)$ and $\beta(\epsilon)$.

---

* C.M. Truesdale, S. Southworth, P.H. Kobrin, U. Becker, D.W. Lindle, and D.A. Shirley, submitted to Phys. Rev. A (1983).

The vibrational branching ratios (R_n) are defined by

$$R_n = \frac{\sigma(v_n)}{\sigma(v_0)} \quad , \tag{2}$$

where $\sigma(v_n)$ is the photoionization cross section of the v_n th vibrational channel and $\sigma(v_0)$ is the cross section of the ground vibrational channel (0,0,0). For the $A^2\Pi_u$ ionic channel of CO_2, v_n will refer to the symmetric stretch vibrational channels (n,0,0). The first quantum number n designates the symmetric stretch modes, where n = 0, 1, 2, 3, and 4. The other quantum numbers refer to the bending and asymmetric stretch vibrational modes. During TOF measurements, all photoelectrons are simultaneously measured. The vibrational branching ratios are inherently more accurate than absolute cross sections, because normalization of photoelectron intensities for sample density and photon flux are not needed.

The purpose of this paper is to report vibrationally-averaged photoionization cross sections and photoelectron asymmetry parameters for the $1\pi_u$ and 8σ orbitals of CO_2 and OCS, which lead to the ionic $A^2\Pi_u$ and $C^2\Sigma^+$ states, respectively. The vibrationally-resolved branching ratios and asymmetry parameters for these ionic channels are also reported. These data are compared to other synchrotron results,[6-10] dipole (e,2e) results,[11] and He I resonance light source results.[12-18] Multiple-scattering model (MSM) calculations[1,6,7,12] for CO_2 and OCS, and Hartree-Fock static-exchange (HF) calculations[19] and Stieltjes-Tchebycheff moment theory (STMT) results[20] for CO_2 are compared to the experimental results.

The photoelectron spectra were obtained with a double-angle-time-of-flight spectrometer. Two detectors, one placed at 0° and another placed at 54.7° with respect to the photon polarization axis, were used to measure ejected photoelectrons by means of microchannel plates. The instrument was described previously.[21] The experiments were performed at the Stanford Synchrotron Radiation Laboratory, on the VUV (8°) beam line with a monochromator resolution of 2.7 Å (FWHM) throughout the entire photon energy range hν = 18-30 eV. The spectrometer kinetic energy resolution $\Delta\varepsilon$ is 3 percent of ε. By retarding the photoelectrons over part of the 28 cm flight path the resolution could be improved significantly.

The intensity measurements at 54.7°, for which $P_2 = 0$, provide angle-independent relative cross sections. The counting period was typically 1000 seconds for the vibrationally-averaged studies of CO_2 and OCS and the vibrationally-resolved studies of CO_2 and 2000 seconds for the OCS vibrationally resolved measurements. The total relative cross section for the photoionization of the four outer valence orbitals of CO_2 and OCS was compared to the dipole (e,2e) total cross sections given by Hitchcock et al.,[22] and White et al.,[23] respectively, in order to determine the scaling factor and place the relative cross sections for the $1\pi_u^{-1}$ and $8\sigma^{-1}$ ionic channels on an absolute scale.

The ratio of photoelectron intensities measured at 0° and 54.7° determines the asymmetry parameter. This ratio was corrected for the relative efficiency of the two detectors in a calibration procedure which has been discussed in detail.[24]

Results and discussion for the $A^2\Pi_u(1\pi_u^{-1})$ channel of CO_2 and the $C^2\Sigma^+(8\sigma^{-1})$ channel of OCS are presented in Sections B and C, respectively.

B. CO_2 $A^2\Pi_u(1\pi_u^{-1})$ Results and Discussion

The ground electronic state of CO_2 can be written $(1\sigma_g)^2(1\sigma_u)^2(3\sigma_g)^2(2\sigma_u)^2(4\sigma_g)^2(3\sigma_u)^2(1\pi_u)^4(1\pi_g)^4\ {}^1\Sigma_g^+$. We present partial cross sections, branching ratios, and asymmetry parameters for the photoionization of CO_2 into the CO_2 $A^2\Pi_u(1\pi_u^{-1})$ channel.

This work addresses the first five symmetric vibrational channels of the $1\pi_u^{-1}$, viz. (n,0,0), for $0 \leq n \leq 4$. From the high-resolution spectra of CO_2, Potts and Fattahallah[25] have assigned these levels binding energies of 17.31, 17.45, 17.59, 17.72, and 17.86 eV, respectively. Time-of-flight spectra of CO_2 taken at 19.3 eV photon energy are shown in Fig. 1. Comparison of intensities measured at 0° and 54.7° shows asymmetries that are vibrational-state dependent.

The vibrationally-unresolved branching ratio for the A/B ionic channels of CO_2 are included in Table I for a few selected photon energies. The A/B branching ratio generally increases monotonically with increasing photon energy. The branching ratio at 21.2 eV measured by Samson and Gardner,[28] including the statistical uncertainty, is within the range of the present results. In Table II the He I resonance lamp asymmetry parameter measurements are presented along with our results. There is excellent agreement by all groups for the vibrationally-

averaged asymmetry parameters. The He I resonance lamp measurements of vibrational branching ratios and asymmetry parameters are also presented in Table II. Good agreement is found among all the data for the vibrationally-resolved asymmetry parameters.

Previous measurements of partial cross sections[8,11] could not completely separate the $A^2\Pi_u$ and $B^2\Sigma_u^+$ peaks, and early experimenters were obliged to sum over the A and B states. The present measurements have significantly higher resolution, with well separated A and B states. To deconvolute the vibrational peaks of the $A^2\Pi_u$ channel, two methods of analysis were performed. A grid search routine[26] was used when the peaks were only slightly overlapping. When the vibrational peaks were more severely overlapping, a simplex algorithm[27] was used to supply the initial guesses of peak parameters for a nonlinear least square fitting routine. In both cases the peak shapes were assumed to be Gaussian.

The vibrationally-averaged results for the $A^2\Pi_u$ channel of CO_2^+ will be presented first, followed by the vibrationally-resolved results. In Fig. 2 the vibrationally-averaged partial cross section and asymmetry parameter are illustrated. The top panel shows the fixed nuclei STMT results,[20] the HF velocity and HF configuration interaction (HFCI) results,[19] and the dipole (e,2e) measurements[11] compared to the present measurements. The (e,2e) experiment could not completely resolve the $A^2\Pi_u$ and $B^2\Sigma_u^+$ ionic channels. Instead, the total cross sections for the $A^2\Pi_u$ and $B^2\Sigma_u^+$ were integrated and the branching ratio of the $A^2\Pi_u$: $B^2\Sigma_u^+$ taken from Samson and Gardner[28]

was used to represent the (e,2e) results for photon energies of 21.2 and 23.1 eV.

The cross section data show a weak maximum near 21 eV and a slow decrease from 20 to 30 eV. The maximum is interpreted as a shape resonance in the $1\pi_u^{-1}$ ionic channel. The MSM calculations of Swanson et al.[1] suggest that the maximum in the cross section near 20 eV is due to a π_g shape resonance. The STMT results of Padial et al.[20] predict a resonance for the $A^2\Pi_u$ ionic channel near 20 eV photon energy, and the HF results of Lucchese and McKoy[19] suggest a resonance at 22 eV. Both theories conclude that the δ ionic channel ($1\pi_u \rightarrow k\delta$) experiences the resonance. The STMT results of Padial et al.[20] predict the position and qualitative shape of the maximum, but their value for the cross section is too high. Both HF calculations overestimate the cross section. Because the STMT calculations used a triplet static-exchange potential for the photoionization of the $1\pi_u$ instead of using a singlet static exchange potential as in the HF calculations, there is a discrepancy in the energy of the maximum in the cross section.[19]

The asymmetry parameter results for the vibrationally-averaged $A^2\Pi_u$ channel of CO_2 based on the fixed-nuclei MSM calculations of Swanson et al.,[1] and Grimm et al.[6], the HF calculations of Lucchese and McKoy,[19], the synchrotron results of Grimm et al.,[6] and the present results are displayed in the bottom panel of Fig. 2. There is good agreement with the theoretical results[6,19] and with the data of Grimm et al.[6] The experimental results, as well as the

theoretical predictions, show an increase in the asymmetry parameter from threshold to an asymptotic value of 1.

Results for the ground vibration channel (0,0,0) of the $A^2\Pi_u$ ionic channel are shown in Fig 3. In the top panel the partial cross section is presented. A maximum near 21 eV is probably evidence of the effect for the shape resonance on the cross section, predicted by Swanson et al.[1]

The asymmetry parameter for the (0,0,0) vibrational channel measured by Grimm et al.[6] is displayed with the present results in the bottom panel of Fig. 3. There is excellent agreement with the measurements of Grimm et al.[6] Both show the weak maximum structure near 21 eV photon energy in the asymmetry parameter, which is proposed to be due to a shape resonance. The theoretical results of Swanson et al.,[1] shown by the solid curve, are also in good overall agreement with experiment.

The remainder of the vibrationally-resolved data for the $A^2\Pi_u$ ionic state of CO_2 are shown in Figs. 4-7. The MSM results of Swanson et al.[1] for vibrationally-resolved branching ratios, which account for both Franck-Condon and non-Franck-Condon effects, are illustrated alongside the present measurements in the top panels of these figures. The vibrationally-resolved asymmetry parameter results of Grimm et al.[6] and the predictions based on a MSM calculation[1] are included in the bottom panels of these figures.

The vibrationally-resolved results for the (1,0,0) vibrational channel of the $A^2\Pi_u$ channel of CO_2 are displayed in Fig 4. The

non-Franck Condon MSM results predict two very shallow maxima in the branching ratio. The Franck-Condon branching ratio is independent of photon energy. The experimental branching ratio shows two large maxima located near 21 and 24 eV photon energy, and the branching ratio is between 2 and 3. We attribute the first feature to the shape resonance effect in the $A^2\Pi_u$ ionic channel. The other feature could result from the σ_u shape resonance as predicted by Swanson et al.[1] or from a resonance in the $1\pi_u \rightarrow k\sigma_g$ subchannel as suggested by Padial et al.[20] and Lucchese and McKoy.[19]

The theoretical results predict vibrational branching ratios higher than the measurements. In addition, the observed modulatation of the branching ratio with photon energy is absent in the Franck-Condon approximation and is very small in the non-Franck-Condon calculation.

The asymmetry parameter for the (1,0,0) channel is presented in the bottom panel of Fig. 4. Again there is excellent agreement with the measurements of Grimm et al.[6] and good agreement with the MSM results of Swanson et al.[1] The experimental results show variations in the 21-22 eV photon energy range, possibly attributable to a shape resonance.

The results for the (2,0,0) vibrational channel are displayed in Fig. 5. The experimental vibrational branching ratio takes values between 2 and 3.5. This channel is the most intense peak over most of the photon energy range of 18-25 eV. The theoretical results are in only fair agreement with the experimental measurements.

The asymmetry parameter for the (2,0,0) channel is displayed in the bottom panel of Fig. 5. The agreement with the MSM predictions and asymmetry parameter measured by Grimm[6] for the (2,0,0) channel are similar to that for the (1,0,0) channel. A possible broad shape resonance falls near 22 eV photon energy. The MSM calculation has significantly higher values near threshold than the data.

Results for the (3,0,0) channel are presented in Fig. 6. The experimental vibrational ratio takes values between 2 and 3. The vibrational branching ratio shows a probable maximum in the 20–21 eV region. Scatter in the data preclude further conclusions.

In the bottom panel of Fig. 6 the asymmetry parameter of the (3,0,0) is displayed. Again there is excellent agreement with the measurements of Grimm et al.[6] and good agreement with the MSM calculations of Swanson et al.[1]. Like the previous vibrational channels the MSM results predict higher asymmetry values than are experimentally measured. A weak feature near 20–21 eV is present in our data and the data of Grimm et al.[6]

The last vibrational channel resolved in the present study of the $A^2\Pi_u$ ionic channel is the (4,0,0) channel, for which results are displayed in Fig. 7. In the top panel the measured vibrational ratio takes values between 1 and 2.3. Similar to all the other vibrational channels, the non-Franck-Condon predictions based on the MSM calculations of Swanson et al.[1] suggest that two maxima are present for the vibrational branching ratio of the (4,0,0) channel. Two maxima appear to be present in our data, near 20 and 24 eV. The maxima are probably due to shape resonances.

In the bottom panel of Fig. 7 the agreement between our results and that of Grimm et al.[6] and the theoretical MSM results of Swanson et al.[1] is similar to the comparisons made for the other vibrational states. The MSM asymmetry parameters, similar to the other channels are higher than the measurements near threshold.

In summary, we can draw a few conclusions about the vibrationally-resolved results for the $A^2\Pi_u$ ionic channel of CO_2.

(1.) The synchrotron radiation results of Grimm et al.[7] are in very good agreement with the present data.

(2.) The vibrationally-resolved branching ratios show non-Franck Condon behavior, as suggested by Swanson et al.[1] Their MSM calculations predict two maxima in the vibrational branching ratios of all the vibrational channels. This is qualitatively confirmed by our results, but quantitative agreement is missing.

(3.) The non-Franck-Condon results of Swanson et al.[1] for the vibrationally-resolved asymmetry parameters for the $A^2\Pi_u$ of CO_2 are generally in good agreement with the present measurements. However, near threshold the theoretical results predict asymmetries higher than the measured asymmetries.

C. OCS $C^2\Sigma^+(8\sigma^{-1})$ Results and Discussion

The ground electronic state of OCS can be written $(1\sigma)^2(2\sigma)^2(3\sigma)^2(4\sigma)^2(S2p)^6(6\sigma)^2(7\sigma)^2(8\sigma)^2(9\sigma)^2(2\pi)^4(3\pi)^4\ {}^1\Sigma^+$. The valence-shell spectrum resulting from the ionization of the last four orbitals has recently been studied theoretically[7,12,29] and experimentally.[7,10,23,31] We present the first vibrationally-resolved studies of the $C^2\Sigma^+$ channel over the photon energy range $h\nu$ = 19-24 eV. The vibrationally-averaged OCS measurements were performed separately, over the photon energy range of 20.5-29 eV.

The OCS $C^2\Sigma^+$ photoelectron peaks were fitted in the same way as the CO_2 $A^2\Pi_u$ peaks. The collection time per spectrum was typically 2000 seconds.

Time-of-flight photoelectron spectra of the $C^2\Sigma^+(8\sigma^{-1})$ ionic channel of OCS, converted to an linear energy scale, are displayed in Fig. 8. From left to right the peaks correspond to the (0,0,2), (1,0,1), (0,0,1), (1,0,0), and (0,0,0) vibrational channels with binding energies of 18.5, 18.34, 18.23, 18.08, and 17.96 eV, respectively.[10] The quality of these spectra are comparable to those obtained by Delwiche et al.[10] It is very apparent that the asymmetry parameter of the (1,0,0) channel is significantly different from all the other channels, as noted by Carlson and McGuire.[16]

Our vibrationally-averaged and vibrationally-resolved asymmetry parameters for the $C^2\Sigma^+$ ionic channel, along with the He I resonance lamp measurements of Carlson and McGuire,[16] are presented in Table III. The two experiments show good agreement.

The vibrationally-averaged partial cross section results for the $C^2\Sigma^+$ ionic channel of OCS from MSM calculations performed by Grimm et al.,[12] synchrotron radiation measurements of Carlson et al.,[7] dipole (e,2e) results of White et al.,[23] and the present results are presented in the top panel of Fig. 9. No obvious structure is apparent in the synchrotron radiation cross section measurements, in contrast to the (e,2e) results. The partial cross section is fairly constant over the photon energy range of 20-29 eV. There is good agreement with the cross section results of Carlson et al.[7] However, there is poor agreement with the (e,2e) results of White et al.[23] and the cross section predicted based on MSM calculations by Carlson et al.[7]

The vibrationally-averaged asymmetry parameter for the $C^2\Sigma^+$ ionic channel measured by Carlson et al.,[7] and by us is presented in the bottom panel of Fig. 9. The measured asymmetry parameter increases slowly with increasing photon energy. There is good agreement with the results of Carlson et al.,[7] but poor agreement with the asymmetry parameter predicted by Grimm et al.[12]

The vibrationally-resolved results for the v_0, (0,0,0) ionic channel are displayed in Fig 10. In the top panel, the partial cross section increases slowly with photon energy. The asymmetry data and the He I resonance line result[16] are illustrated in the bottom panel of Fig. 10.

The OCS $C^2\Sigma^+$ ionic channel vibrational ratios are displayed in the top panels, and the He I resonance line results along with the present results are presented in the bottom panels, of Figs. 11-13.

The vibrationally-resolved results for the (1,0,0) $C^2\Sigma^+$ ionic channel are presented in Fig. 11. In the top panel, the vibrational branching ratio generally decreases with increasing photon energy, with a possible maximum at the low energy end.

The asymmetry parameter for the (1,0,0) channel is presented in the bottom panel of Fig. 11. The asymmetry parameter increases from -0.5 to 0.5 over the photon energy range 19 to 24 eV. There is some discrepancy present between the He I results[16] and the present results. Nonetheless, we confirm that the asymmetry parameter for the (1,0,0) is dissimilar to the (0,0,0) vibrational channel, as discussed by Carlson and McGuire.[16] The reason for this different behavior remains unexplained.

Vibrationally-resolved results for the (0,0,1) asymmetric stretch vibrational channel of the $C^2\Sigma^+$ ionic channel of OCS are displayed in Fig. 12. The vibrational branching ratio for this channel is presented in the top panel. Its behavior is similar to that of the (1,0,0) channel.

The asymmetry parameter for the (0,0,1) channel is displayed in the bottom panel of Fig. 12. The asymmetry parameter increases slowly from 19-24 eV. It is difficult to identify any resonance structure because of the scatter in the data. There is excellent agreement with the He I resonance line measurement[16] for this channel.

The final vibrationally-resolved channel that we studied was the (0,0,2) channel. Measurements for this state from 19-22 eV are presented in the top panel of Fig. 13. The branching ratio is very small (~0.05-0.10), and the scatter of the data preclude identifying any trends.

The asymmetry parameter for the (0,0,2) channel is displayed in the bottom panel of Fig. 13. A flat dependence for the asymmetry parameter is observed. There is excellent agreement with the He I resonance line result.[16] The energy dependence of this asymmetry parameter is very similar to the (0,0,0) and (0,0,1) vibrational channels, in contrast to the (1,0,0) channel.

The conclusions we can draw about the vibrational-resolved results for the $C^2\Sigma^+$ ionic channel of OCS are as follows:

(1.) There is good to excellent agreement with the vibrationally-averaged and vibrationally-resolved He I resonance line results of Carlson and McGuire.[16]

(2.) The synchrotron radiation results of Carlson et al.[7] are in good agreement with present measurements for the vibrationally-averaged partial cross section and asymmetry parameter for the $C^2\Sigma^+$ ionic channel of OCS.

(3.) The vibrationally averaged partial cross sections obtained from (e,2e) measurements of White et al.[23] are in poor agreement, probably because their measurements have lower energy resolution and lower counting statistics than the present measurements.

(4.) The vibrationally-averaged cross section and asymmetry parameter for the $C^2\Sigma^+$ ionic channel of OCS do not appear to have resonance features.

(5.) The vibrationally-averaged results based on MSM calculations of Grimm et al.[12] and Carlson et al.[7] are in poor agreement with the measurements.

(6.) There seem to be maxima in the vibrational branching ratios for the (1,0,0) and (0,0,1) vibrational channels of the $C^2\Sigma^+$ ionic channel of OCS.

(7.) The angular nature of the (1,0,0) vibrational channel in forming the OCS $C^2\Sigma^+$ state is significantly different from that of all the other vibrational channels.

References

1. J.R. Swanson, D. Dill, and J.L. Dehmer, J. Phys. B: At. Mol. Phys. 14, L207 (1981).

2. Ch. Jungen and O. Altebek, J. Chem. Phys. 66, 5584 (1977); Ch. Jungen and D. Dill, J. Chem. Phys. 73, 3338 (1980).

3. Y. Itikawa, Chem. Phys. Lett. 62, 261 (1979); Y. Itikawa, Chem. Phys. 37, 410 (1979).

4. A.C. Parr, D.L. Ederer, B.E. Cole, J.B. West, R. Stockbauer, K. Codling, J.L. Dehmer, Phys. Rev. Lett. 46, 22 (1981); A.C. Parr, D.L. Ederer, J.L. Dehmer, and D.M.P. Holland, J. Chem. Phys. 77, 111 (1982); P. Morin, I. Nenner, M.Y. Adam, M.J. Hubin-Franskin, J. Delwiche, H. Lefebvre-Brion, and A. Giusti-Suzor, Chem. Phys. Lett. 92, 609 (1982); P. Morin, I. Nenner, P.M. Guyon, L.F.A. Ferreira, and K. Ito, Chem. Phys. Lett. 92, 103 (1982); C.M. Truesdale, S. Southworth, P.H. Kobrin, D.W. Lindle, and D.A. Shirley, to be published in J. Chem. Phys. (1983).

5. C.N. Yang, Phys. Rev. 74, 764 (1948); J. Cooper and R.N. Zare, J. Chem. Phys. 48, 942 (1968).

6. F.A Grimm, J.D. Allen, Jr., T.A. Carlson, M.O. Krause, D. Mehaffy, P.R. Keller, and J.W. Taylor, ibid. 75, 92 (1981).

7. T.A. Carlson, M.O. Krause, and F.A. Grimm, J. Chem. Phys. 77, 1701 (1982).

8. T. Gustafsson, E.W. Plummer, D.E. Eastman, and W. Gudat, Phys. Rev. A 17, 175 (1978).

9. T.A. Carlson, M.O. Krause, and F.A. Grimm, J. Chem. Phys. 77,

701 (1982).

10. J. Delwiche, M.J. Hubin-Franskin, P.M. Guyon, and I. Nenner, J. Chem. Phys. 74, 4219 (1981).
11. C.E. Brion and K.H. Tan, J. Electron Spectrosc. Relat. Phenom. 15, 241 (1979).
12. F.A. Grimm, T.A. Carlson, W.B. Dress, P. Agron, J.O. Thomson, and J.W. Davenport, J. Chem. Phys. 72, 3041 (1980).
13. M.H. Kibel, F.J. Leng, and G.L. Nyberg, J. Electron Spectrosc. Relat. Phenom. 15, 281 (1979).
14. W.H. Hancock, J.A.R. Samson, ibid. 9, 211 (1976).
15. T.A. Carlson, G.E. McGuire, A.E. Jonas, K.L. Cheng, C.P. Anderson, C.C. Lu, and B.P. Pullen, in Electron Spectroscopy, ed. D.A. Shirley (North Holland, Amsterdam (1972)) p. 207.
16. T.A. Carlson and G.E. McGuire, J. Electron Spectrosc. Relat. Phenom. 1, 209 (1972/73).
17. S. Katsumata, Y. Achiba, and K. Kimura, ibid. 17, 229 (1979).
18. J. Kriele and A. Schweig, ibid. 20, 191 (1980).
19. R.R. Lucchese and V. McKoy, Phys. Rev. A 26, 1406 (1982).
20. N. Padial, G. Csanak, B.V. McKoy, P.W. Langhoff, ibid. 23, 218 (1981).
21. M.G. White, R.A. Rosenberg, G. Gabor, E.D. Poliakoff, G. Thornton, S.H. Southworth, and D.A. Shirley, Rev. Sci. Instrum. 50, 1288 (1979).
22. A.P. Hitchcock, C.E. Brion, and M.J. van der Wiel, Chem. Phys. 45, 461 (1980).

23. M.G. White, K.T. Leung, and C.E. Brion, J. Electron Spectrosc. Relat. Phenom. 23, 127 (1981).

24. S. Southworth, C.M. Truesdale, P.H. Kobrin, D.W. Lindle, W.D. Brewer, and D.A. Shirley, J. Chem. Phys. 76, 143 (1982).

25. A.W. Potts and G.H. Fattahallah, J. Phys. B: Atom. Molec. Phys. 13, 2545 (1980).

26. P.R. Bevington, Data Reduction and Error Analysis for the Physical Sciences (McGraw Hill, New York, 1969),p. 208.

27. J.A. Nelder and R. Mead, Computer J. 7, 308 (1965); R. O'Neill, Applied Statictics 20, 338 (1971).

28. J.A.R. Samson and J.L. Gardner, J. Geophys. Res. 78, 3663 (1973).

29. J.P.D Cook, M.G. White, C.E Brion, W. Domcke, J. Schirmer, L.S Cederbaum, and W. Von Niesson, J. Electron Spectrosc. Relat. Phenom. 22, 261 (1981).

Table I. Branching ratios of the $A^2\Pi_u(1\pi_u^{-1})$: $B^2\Sigma_u^+$ ionic channels of CO_2.

hν(eV)	A/B[a]	hν(eV)	A/B
18.7	1.13(12)	22.3	0.60(7)
19.3	0.75(8)	22.6	0.81(8)
20.0	0.70(7)	22.8	1.28(15)
20.3	0.70(8)	23.1	0.74(7)[b]
20.6	0.74(9)	23.8	0.89(6)
21.2	0.80(10)	24.3	1.14(10)
	0.65(5)[b]	24.8	1.05(11)
21.6	0.75(8)	26.0	1.15(10)

a. Errors in the last digit given parenthetically.

b. Ref. 28.

Table II. Comparison of He I (21.2 eV) resonance lamp vibrationally-averaged and resolved asymmetry parameter for the $A^2\Pi_u$ channel of CO_2 with the present measurements.

	avg. β	$\beta(v_0)^a$	$\beta(v_1)$	$\beta(v_2)$	$\beta(v_3)$	$\beta(v_4)$
Ref. 12	-----	-----	-----	1.01(5)	-----	-----
Ref. 13	0.80	-----	-----	-----	-----	-----
Ref. 14	-----	0.80(5)	0.80(5)	0.80(5)	-----	-----
Ref. 15	-----	0.70(10)	0.90(7)	-----	-----	-----
Ref. 16	0.80(10)	0.90(20)	-----	0.80(10)	0.70(5)	0.60(10)
Ref. 17	-----	-----	-----	0.83(8)	-----	-----
Ref. 18	0.72(3)	0.72(3)	0.88(5)	0.78(3)	0.63(2)	0.49(2)
Present	0.71(6)	0.85(5)	0.85(5)	0.80(6)	0.55(10)	0.50(7)

a. The $v_0 - v_4$ designations refer to the symmetric modes (0,0,0), (1,0,0), (2,0,0), (3,0,0), and (4,0,0) of the $A^2\Pi_u(1\pi^{-1})$ ionic channel of CO_2.

Table III. Comparison of He I (21.2 eV) resonance source vibrationally-averaged and resolved asymmetry parameter for the $C^2\Sigma^+$ channel of OCS with the present measurements.

	avg. β	$\beta(v_0)^a$	$\beta(v_1)$	$\beta(v_2)$	$\beta(v_3)$
Ref. 16	0.55(10)	0.55	0.25(7)	0.72(8)	0.68(10)
Present	0.54(7)	0.61(6)	-0.18(14)	0.74(7)	0.69(27)

a. The v_0 - v_3 refer to the (0,0,0), (1,0,0), (0,0,1), and (0,0,2) vibrational channels of the $C^2\Sigma^+(8\sigma^{-1})$ ionic channel of OCS.

Figure Captions

Figure 1. Time-of-flight spectra of CO_2 taken at a photon energy of 19.3 eV, showing the vibrationally resolved peaks of the $A^2\Pi_u$ and $B^2\Sigma_u^+$ ionic channels. The vibrational peaks for the $A^2\Pi_u$ from left to right are: (4,0,0), (3,0,0), (2,0,0), (1,0,0), and (0,0,0). The quantum numbers refer to symmetric stretch, bending, and asymmetric stretch modes. The vibrational peaks for the $B^2\Sigma_u^+$ from left to right are (1,0,0) and (0,0,0).

Figure 2. Vibrationally-averaged $\sigma(\epsilon)$ and $\beta(\epsilon)$ for the $A^2\Pi_u$ ionic channel of CO_2. For the $\sigma(\epsilon)$ curves, (--) represents the STMT calculation of Padial et al.,[20] (— —) the HF velocity calculation of Lucchese and McKoy,[19] the solid curve is the HFCI calculation of Lucchese and McKoy,[19] open circles are the dipole (e,2e) measurements of Brion and Tan[10], and filled circles are the present measurements. For the $\beta(\epsilon)$ curves, the solid curve shows the fixed-nuclei MSM calculation of Swanson et al.,[1] the dotted curve the fixed-nuclei HF calculation of Lucchese and McKoy,[19] and the dashed curve the MSM calculation of Grimm et al.[6] Open circles show the measurements of Grimm et al.,[6] and filled circles the present measurements with statistical uncertainties.

Figure 3. Photoionization cross section and asymmetry parameter $\beta(\epsilon)$ for the (0,0,0) vibrational channel of the $A^2\Pi_u$ ionic state of CO_2. Filled circles show the measured photoionization cross

sections. For $\beta(\epsilon)$, the solid curve shows the MSM calculation of Swanson et al.,[1] open circles the measurements of Grimm et al.,[6] and filled circles the present measurements.

Figure 4. The vibrational branching ratio and $\beta(\epsilon)$ for the (1,0,0) vibrational channel of the $A^2\Pi_u$ ionic state of CO_2. For the vibrational branching ratios, the solid curve shows the MSM calculation of Swanson et al.,[19] the dashed curve shows the Franck-Condon prediction,[19] and the experimental results are shown by filled circles. For $\beta(\epsilon)$, the solid curve shows the MSM calculation of Swanson et al.,[1] open circles represent the measurements of of Grimm et al.,[6] and the present measurements are shown by filled circles.

Figure 5. Vibrational branching ratio and $\beta(\epsilon)$ for the (2,0,0) vibrational channel of the $A^2\Pi_u$ ionic state of CO_2. The experimental and theoretical results are denoted as in Fig. 4.

Figure 6. Vibrational branching ratio and $\beta(\epsilon)$ for the (3,0,0) vibrational channel of the $A^2\Pi_u$ ionic state of CO_2. The experimental and theoretical results are denoted as in Fig. 4.

Figure 7. Vibrational branching ratio and $\beta(\epsilon)$ for the (4,0,0) vibrational channel of the $A^2\Pi_u$ ionic state of CO_2. The experimental and theoretical results are denoted as in Fig. 4.

Figure 8. Time-of-flight spectra taken at the He I energy (21.22 eV), with a 2 V retarding potential, for the $C^2\Sigma^+(8\sigma^{-1})$ ionic channel of OCS, after conversion to a linear energy scale. The

photoelectron peaks from left to right are the (0,0,2), (1,0,1), (0,0,1), (1,0,0), and (0,0,0) vibrational channels, with binding energies 18.5, 18.34, 18.23, 18.08, and 17.96 eV, respectively.

Figure 9. Vibrationally-averaged $\sigma(\epsilon)$ and $\beta(\epsilon)$ for the $C^2\Sigma^+$ ionic channel of OCS. For the $\sigma(\epsilon)$ curves, O are the dipole (e,2e) measurements of White et al.,[23] ϕ are the measurements of Carlson et al.,[7] and $\blacklozenge$ are the present measurements. For the $\beta(\epsilon)$ results in the bottom panel, ϕ are the measurements of Carlson et al.,[7] and $\blacklozenge$ are the present measurements.

Figure 10. $\sigma(\epsilon)$ and $\beta(\epsilon)$ for the (0,0,0) vibrational channel for the $C^2\Sigma^+$ ionic channel of OCS. In both panels filled circles are the present measurements. In the bottom panel the open circle is the He I resonance lamp measurement of Carlson and McGuire.[16]

Figure 11. Vibrational branching ratio and $\beta(\epsilon)$ for the (1,0,0) vibrational channel for the $C^2\Sigma^+$ ionic channel of OCS. The experimental results are denoted as in Fig. 10.

Figure 12. Vibrational branching ratio and $\beta(\epsilon)$ for the (0,0,1) vibrational channel for the $C^2\Sigma^+$ ionic channel of OCS. The experimental results are denoted as in Fig. 10.

Figure 13. Vibrational branching ratio and $\beta(\epsilon)$ for the (0,0,2) vibrational channel for the $C^2\Sigma^+$ ionic channel of OCS. The experimental results are denoted as in Fig. 10.

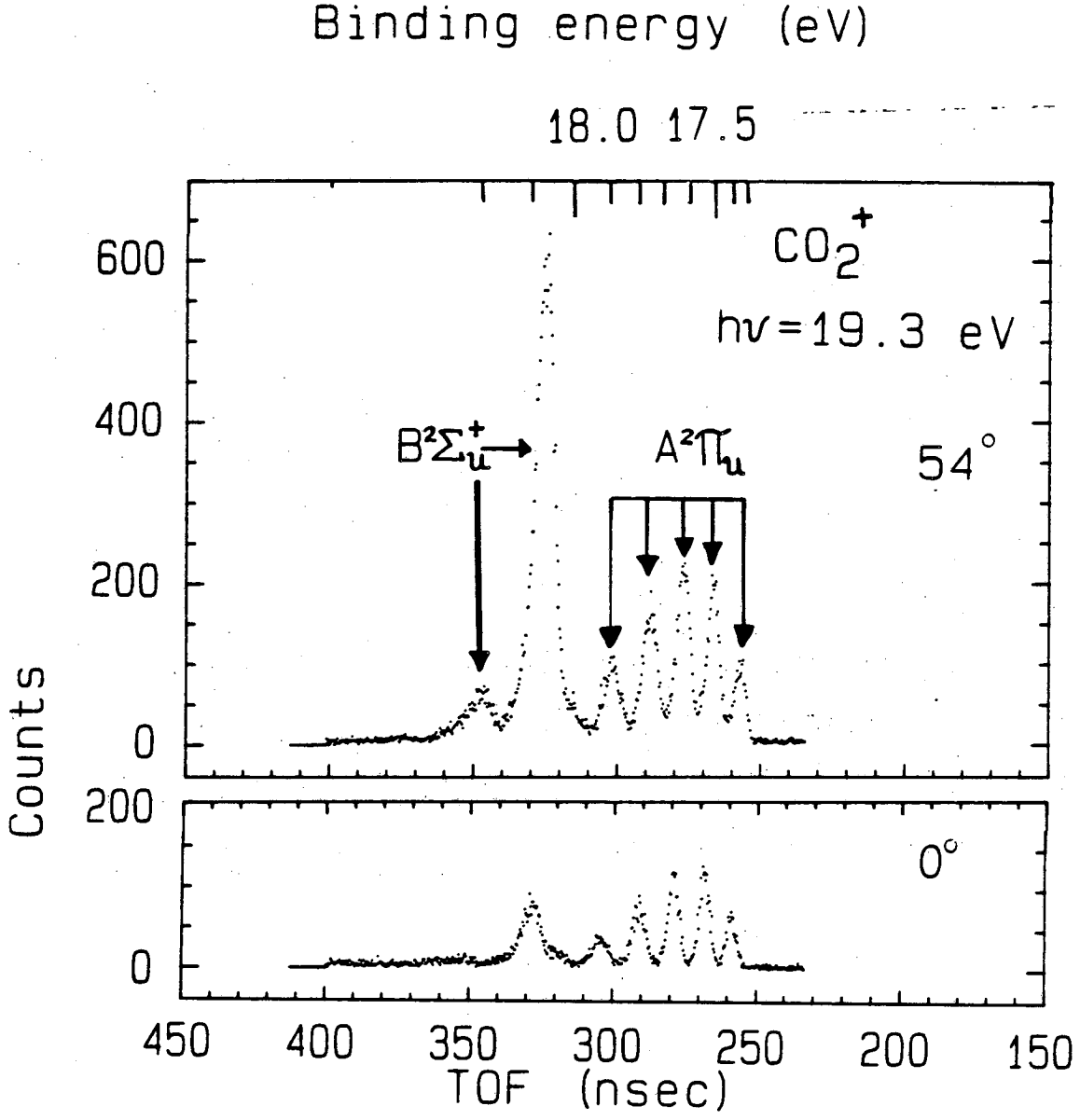

XBL 833-8542

Fig. 1

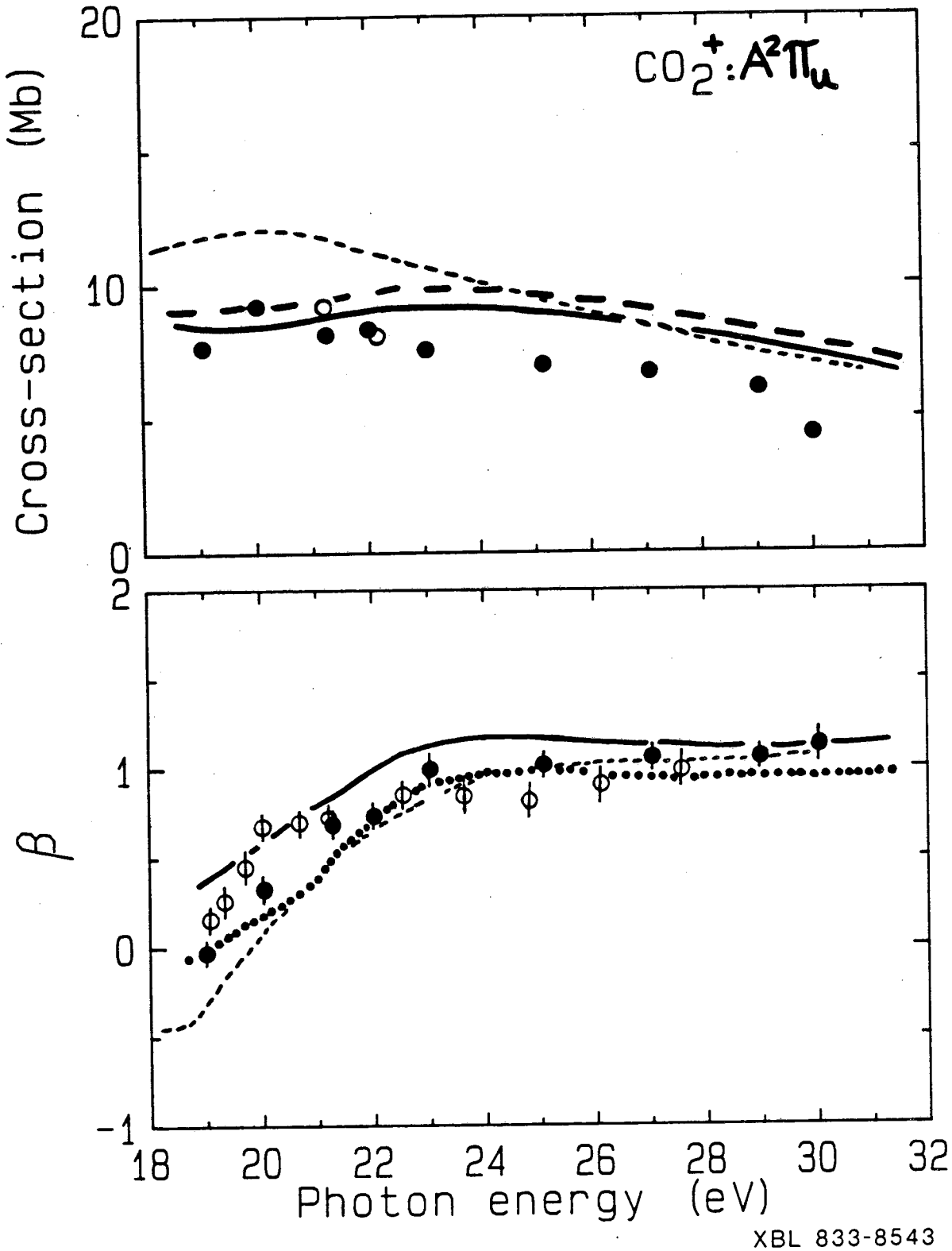
$CO_2^+:A^2\Pi_u$
Cross-section (Mb)
20
10
0
2
1
0
-1
β
18
20
22
24
26
28
30
32
Photon energy (eV)
XBL 833-8543

Fig. 2

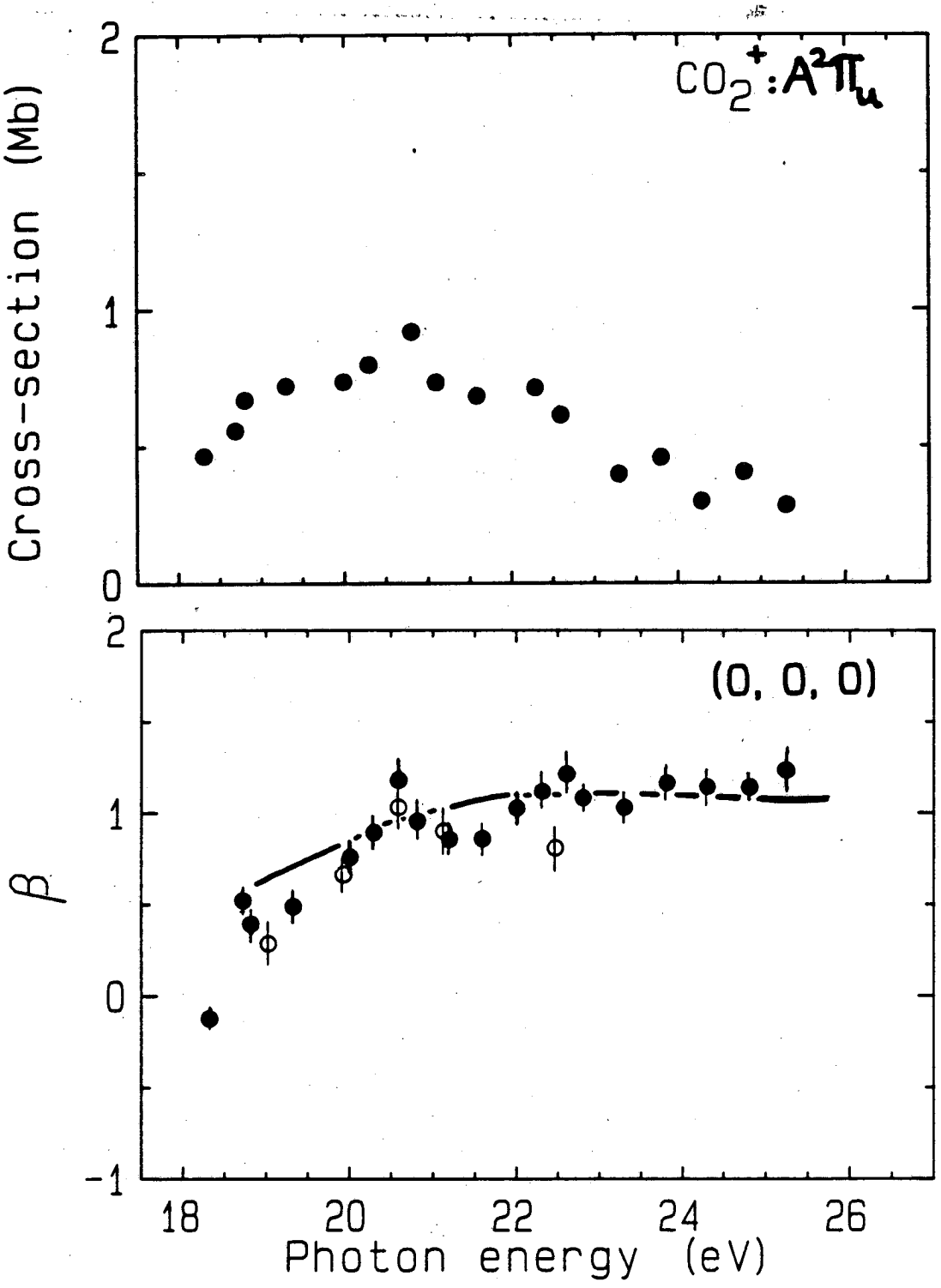

XBL 833-8545

Fig. 3

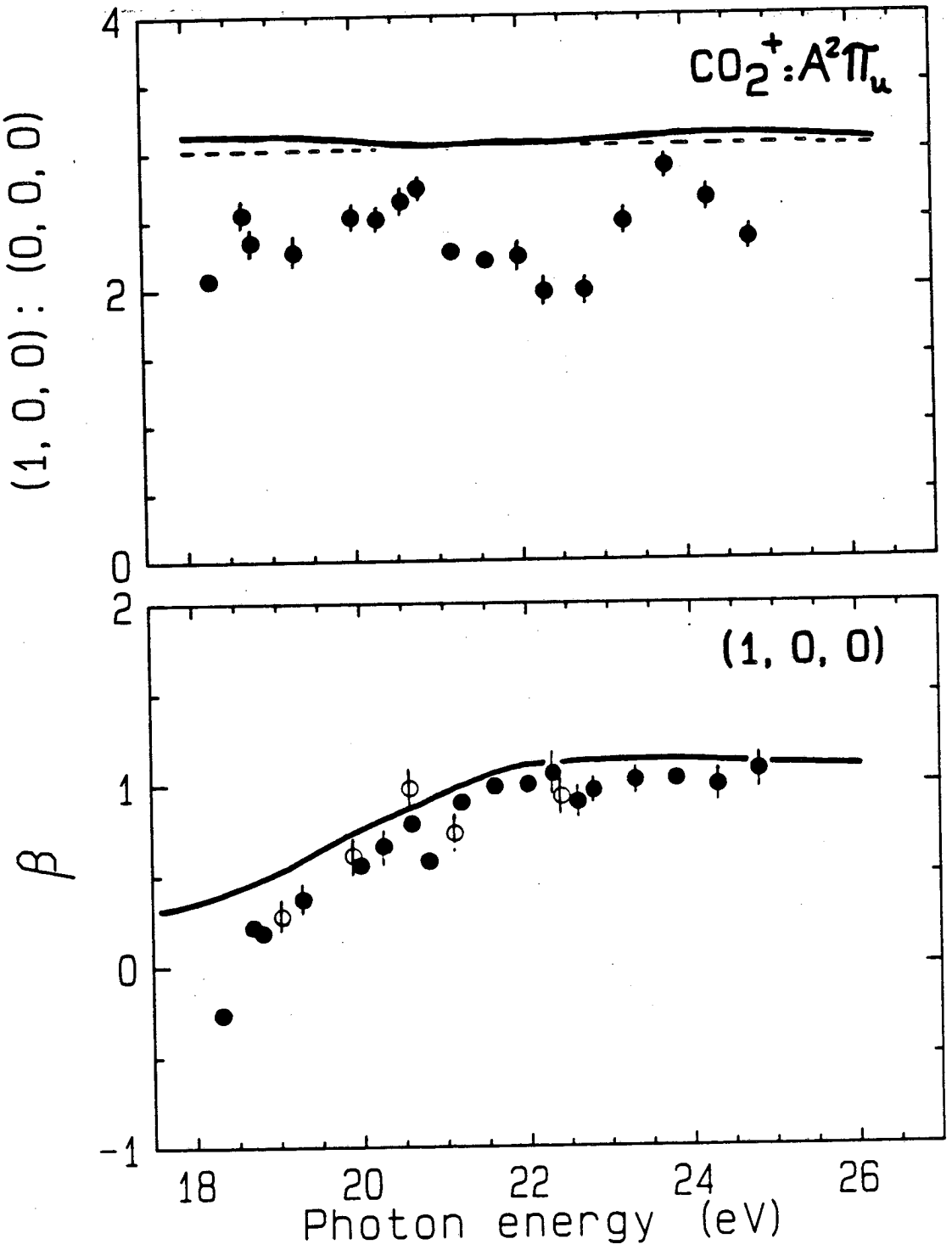

XBL 833-8544

Fig. 4

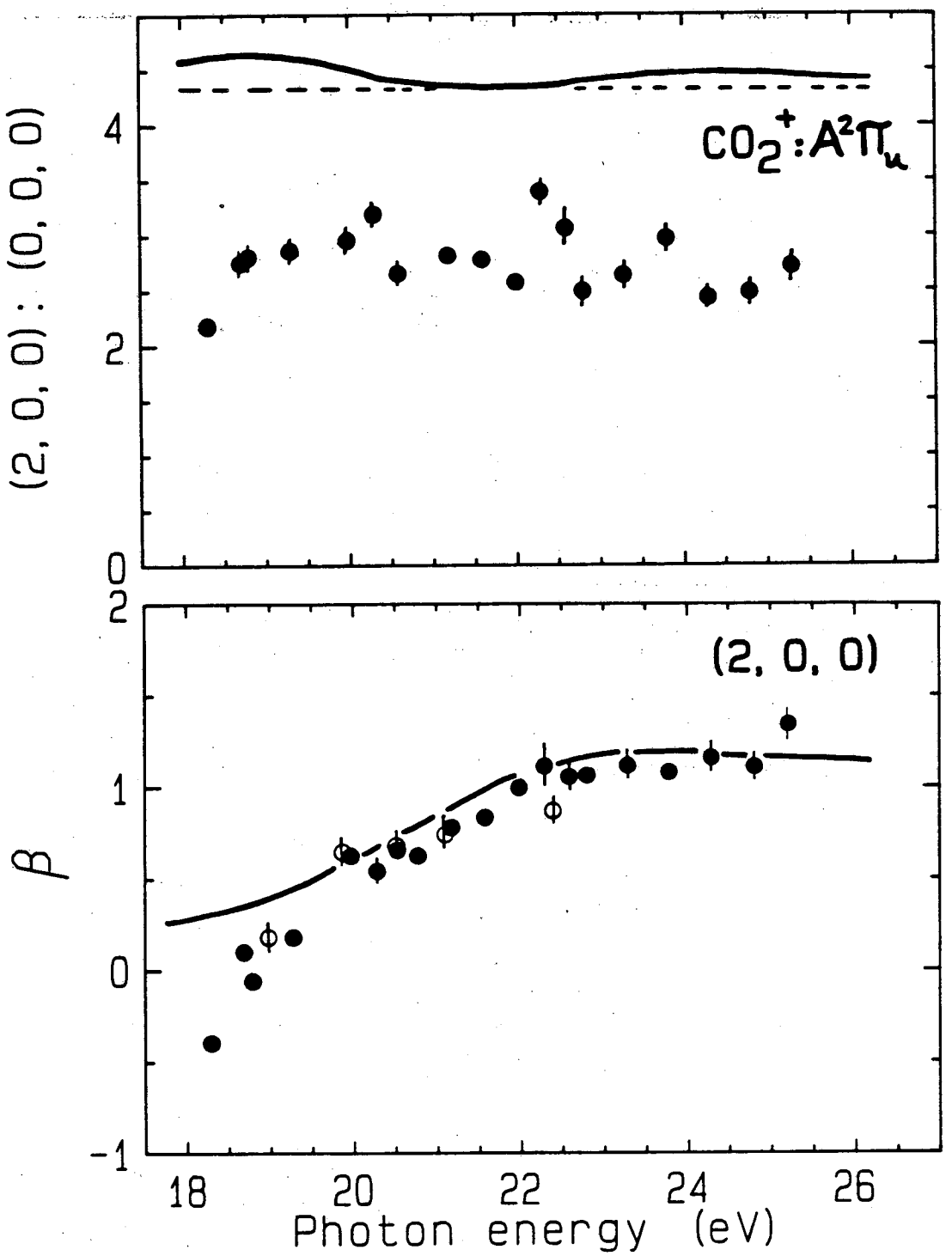

XBL 833-3546

Fig. 5

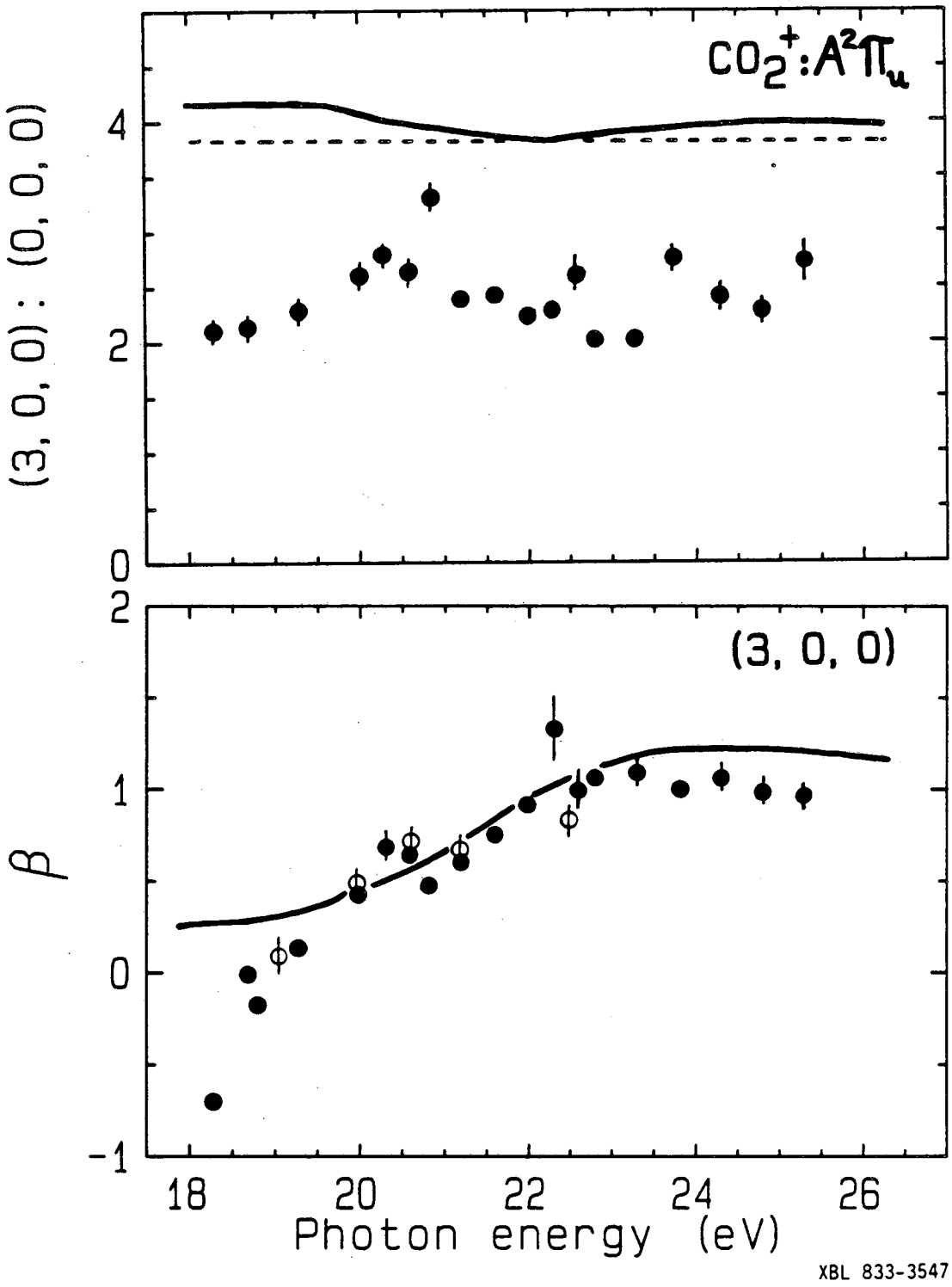
$CO_2^+:A^2\Pi_u$
(3, 0, 0) : (0, 0, 0)
4
2
0
2
1
0
−1
β
(3, 0, 0)
18
20
22
24
26
Photon energy (eV)
XBL 833-3547

Fig. 6

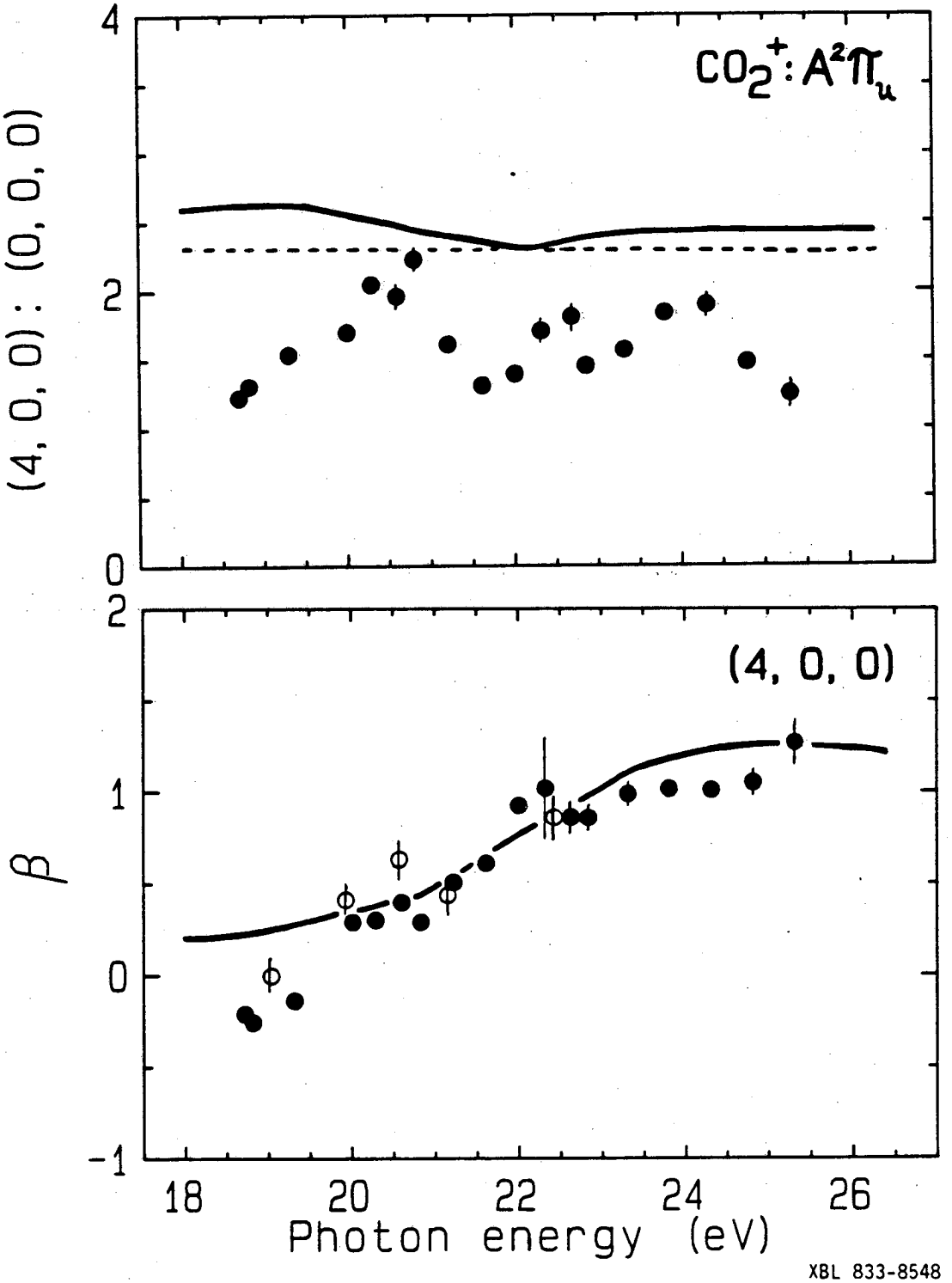
$CO_2^+: A^2\Pi_u$
(4, 0, 0) : (0, 0, 0)
4
2
0
(4, 0, 0)
β
2
1
0
−1
18
20
22
24
26
Photon energy (eV)
XBL 833-8548

Fig. 7

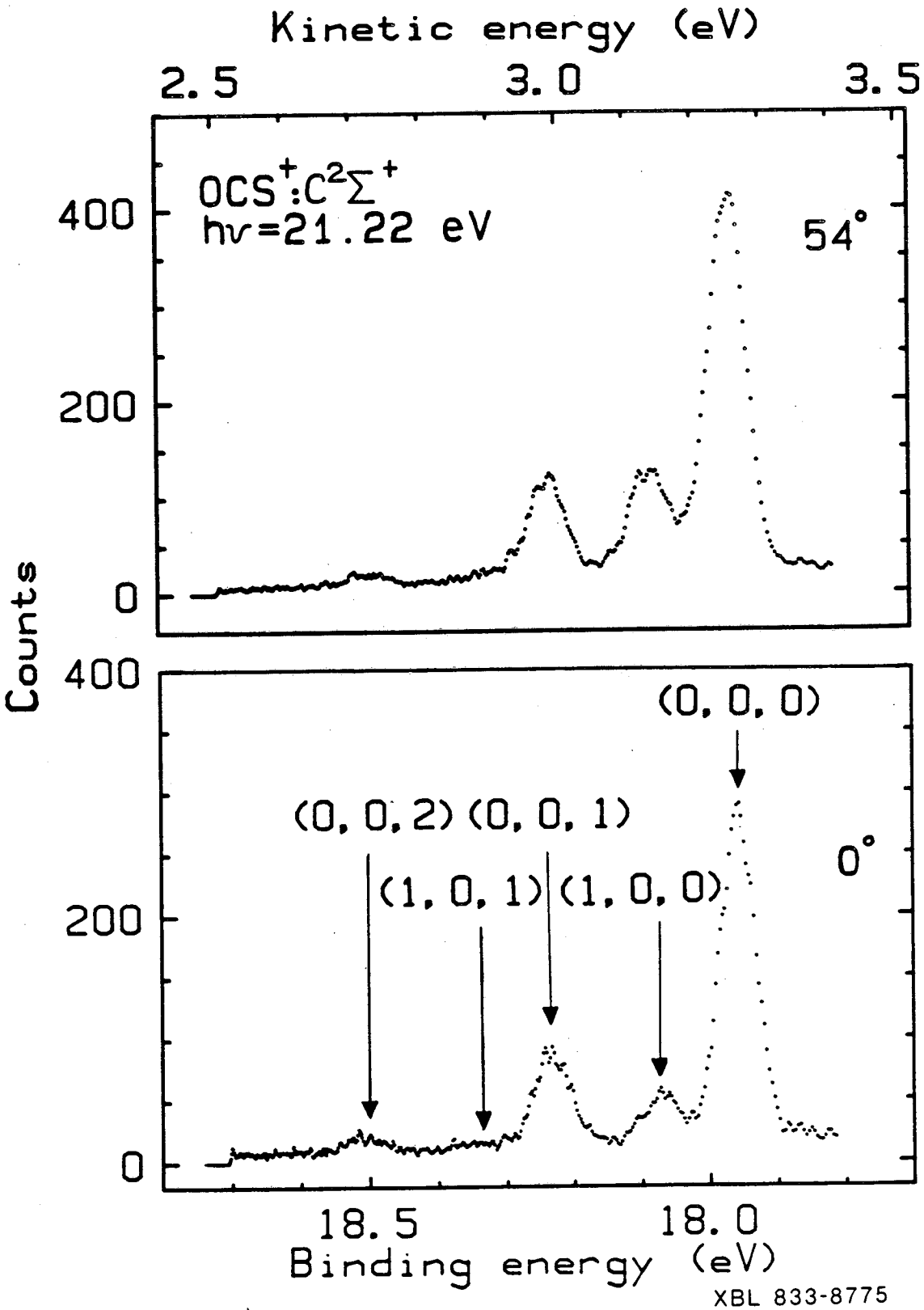
Kinetic energy (eV)
2.5
3.0
3.5
$OCS^+:C^2\Sigma^+$
hν=21.22 eV
54°
400
200
0
Counts
400
200
0
(0, 0, 0)
(0, 0, 2)
(0, 0, 1)
(1, 0, 1)
(1, 0, 0)
0°
18.5
18.0
Binding energy (eV)
XBL 833-8775

Fig. 8

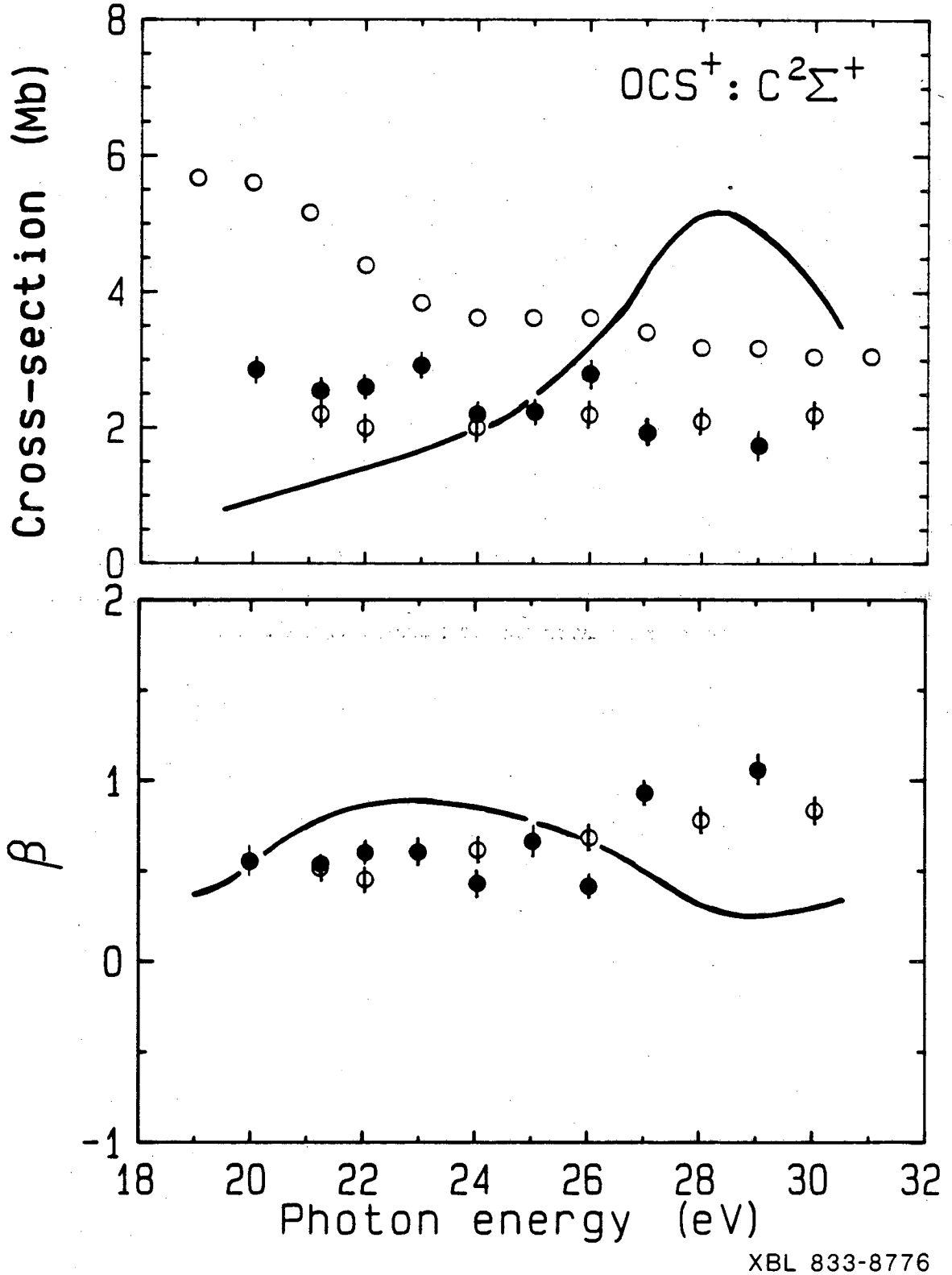
OCS+: C 2Σ+
Cross-section (Mb)
β
Photon energy (eV)
8
6
4
2
0
2
1
0
-1
18
20
22
24
26
28
30
32
XBL 833-8776

Fig. 9

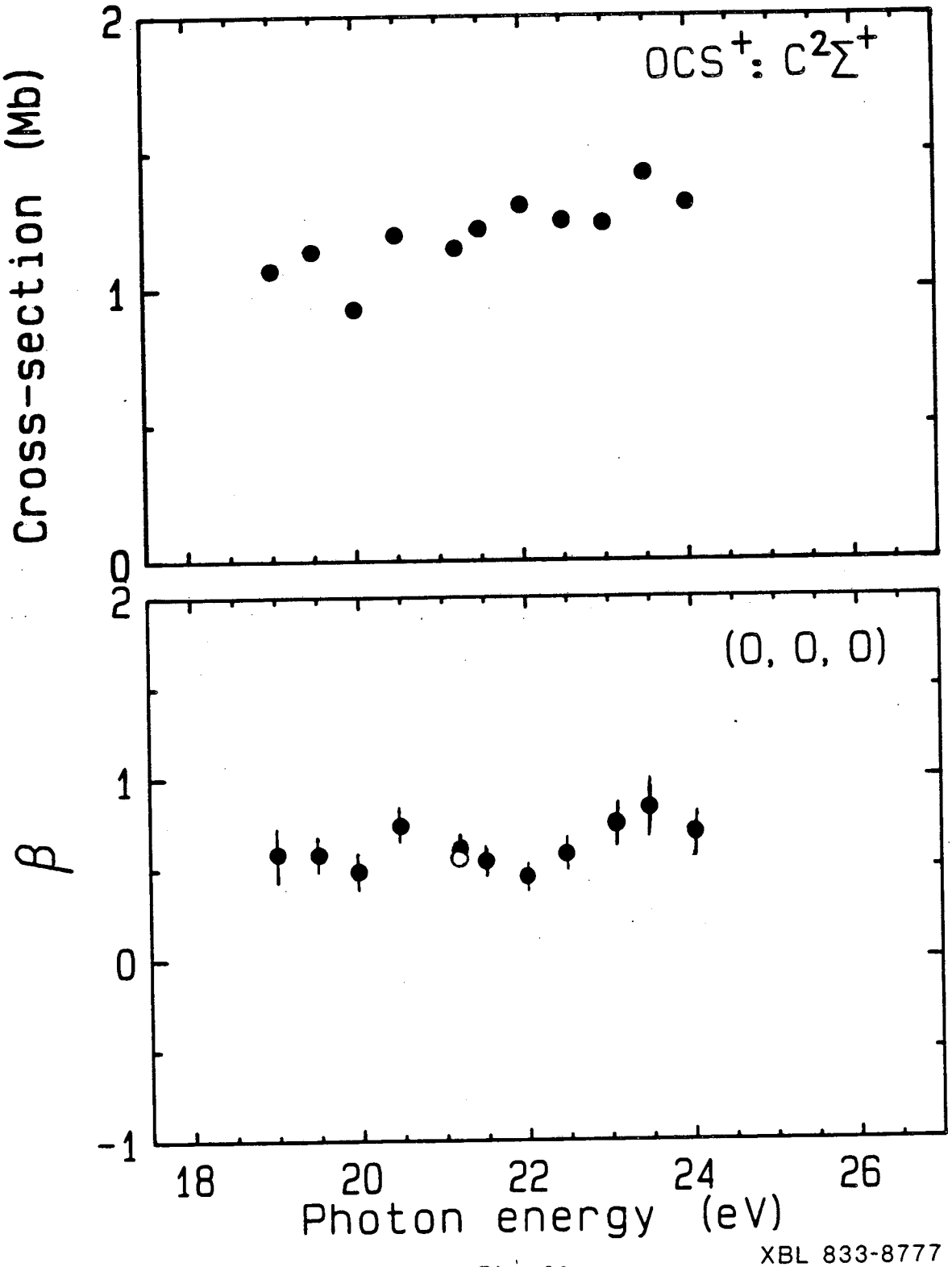
OCS+: C2Σ+
Cross-section (Mb)
2
1
0
(0, 0, 0)
β
2
1
0
-1
18
20
22
24
26
Photon energy (eV)
XBL 833-8777

Fig. 10

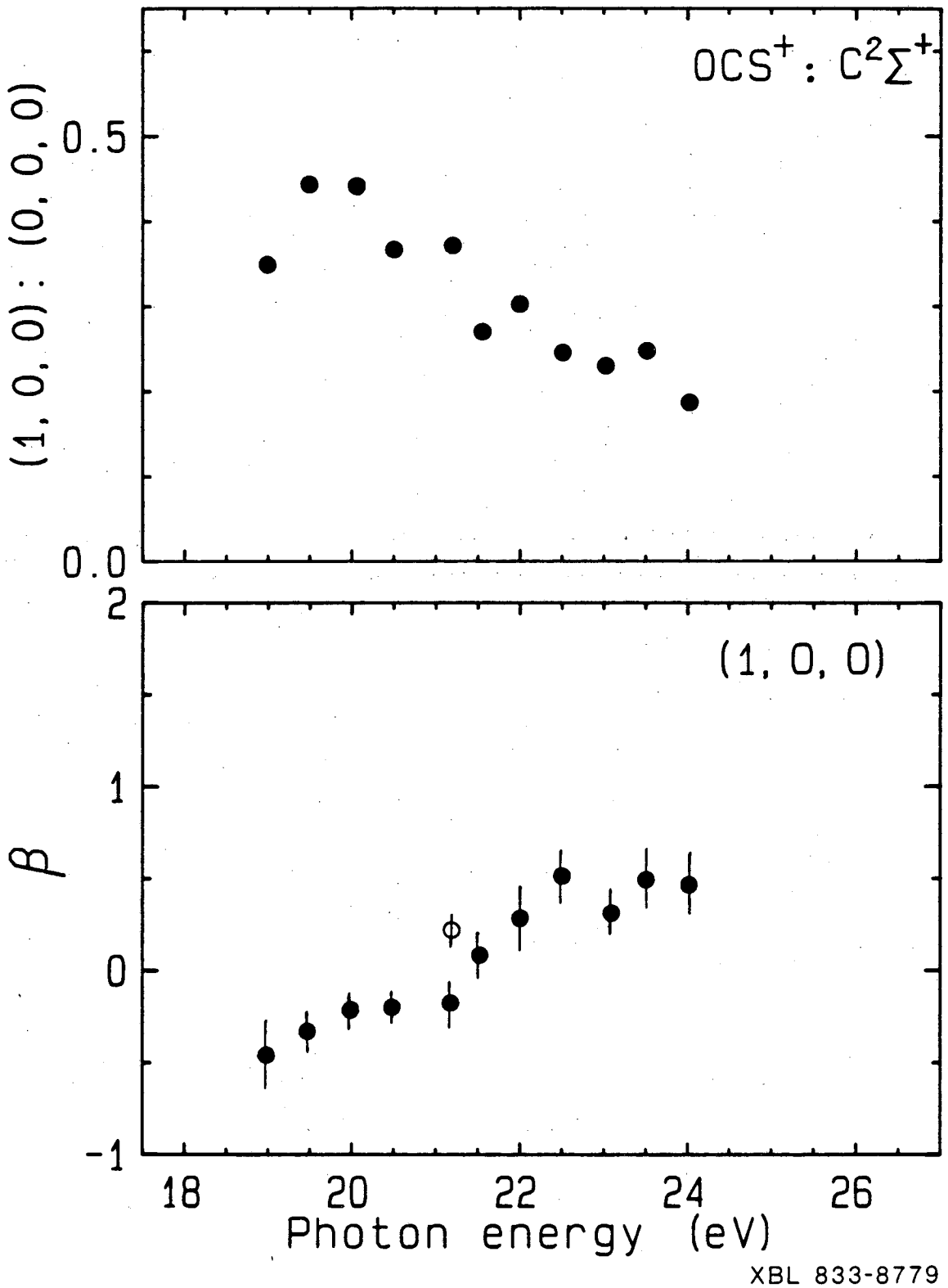
OCS+ : C2Σ+
(1, 0, 0) : (0, 0, 0)
0.5
0.0
(1, 0, 0)
β
2
1
0
−1
18
20
22
24
26
Photon energy (eV)
XBL 833-8779

Fig. 11

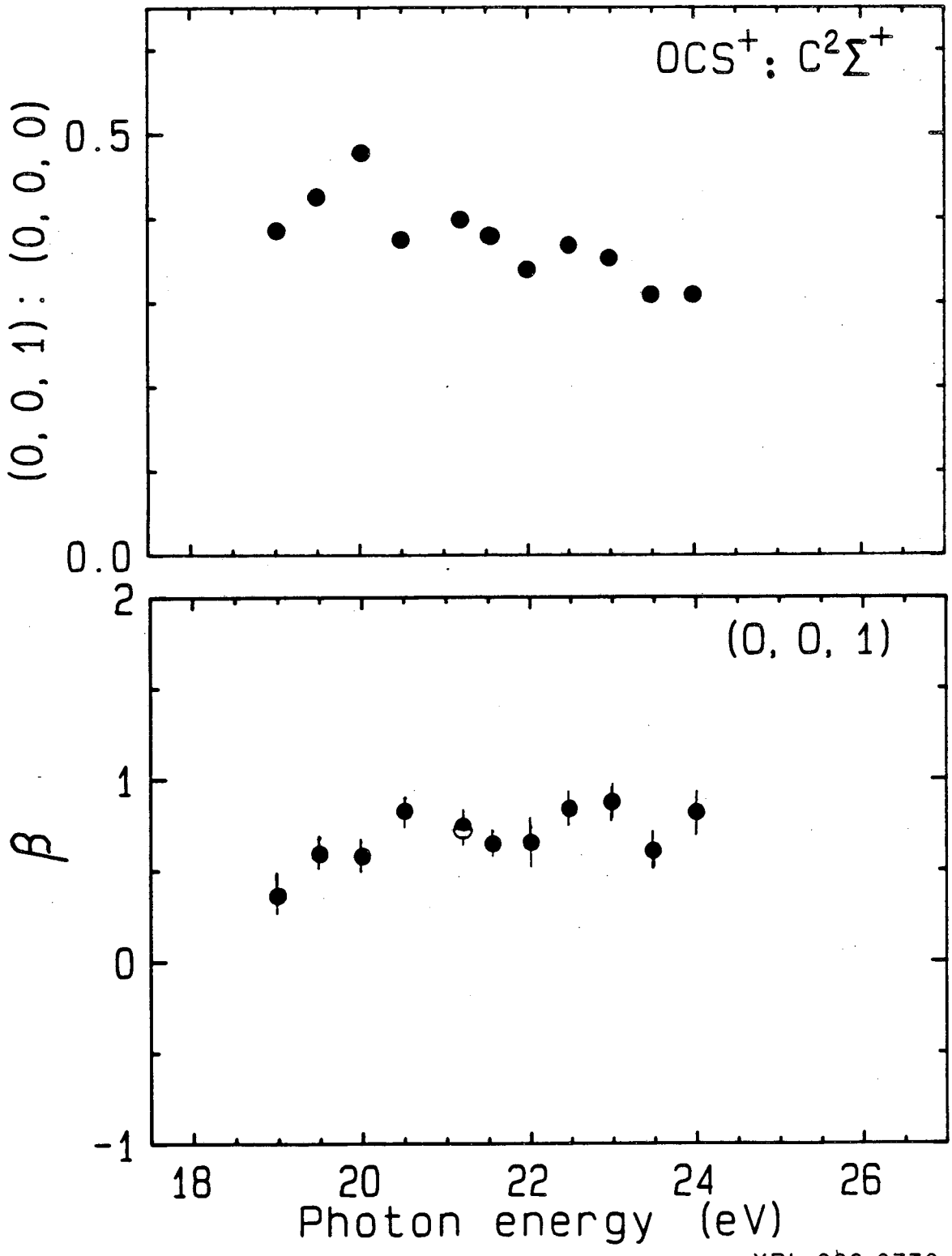
OCS+: C2Σ+
(0, 0, 1): (0, 0, 0)
0.5
0.0
(0, 0, 1)
β
2
1
0
-1
18
20
22
24
26
Photon energy (eV)
XBL 833-8778

Fig. 12

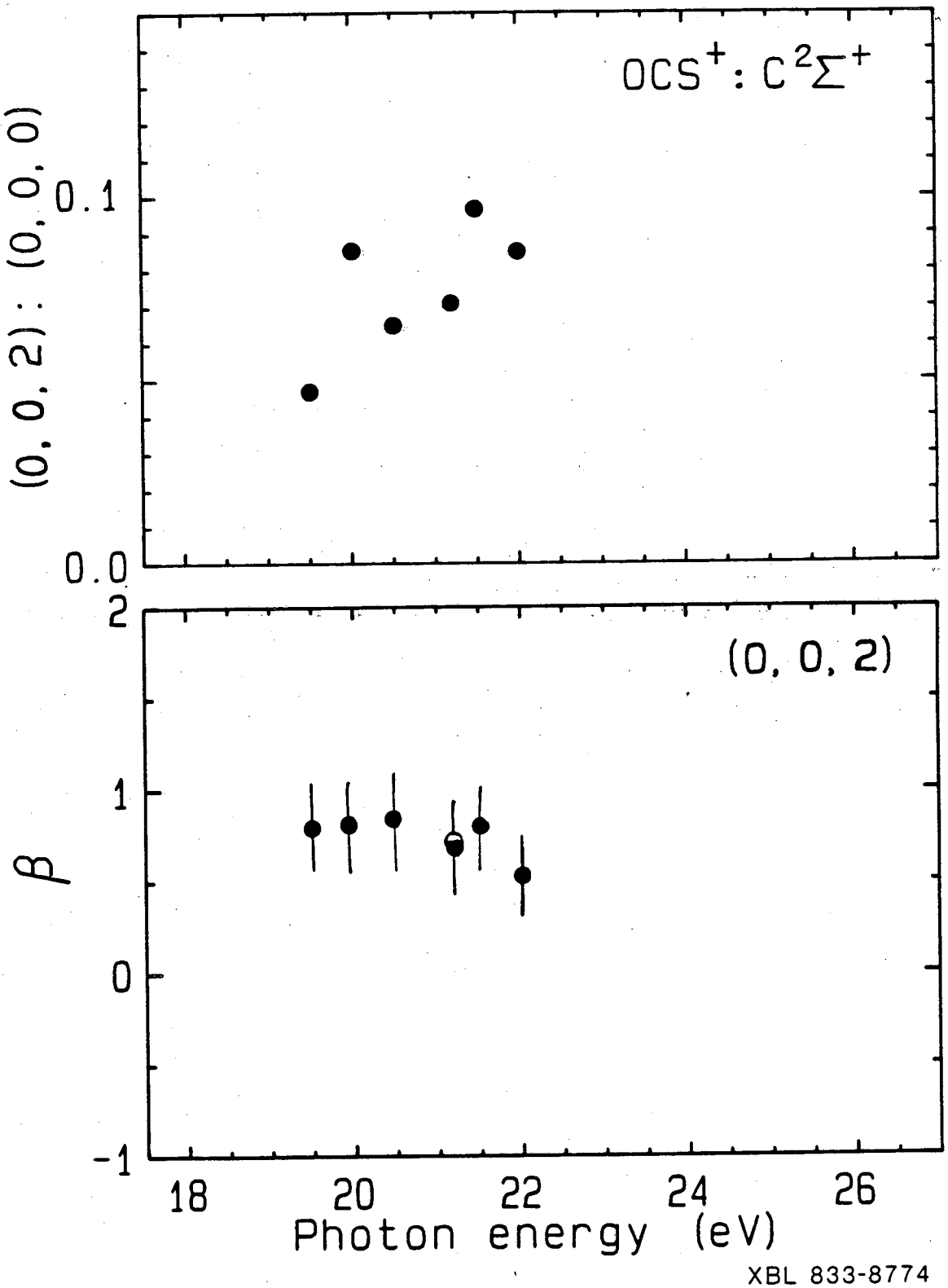
OCS+: C 2Σ+
(0, 0, 2): (0, 0, 0)
0.1
0.0
(0, 0, 2)
β
2
1
0
-1
18
20
22
24
26
Photon energy (eV)
XBL 833-8774

Fig. 13

VI. CORE LEVEL PHOTOELECTRON AND AUGER SHAPE RESONANCE PHENOMENA IN CO, CO_2, CF_4, AND OCS*

A. Introduction

Direct photoexcitation of molecular core levels by variable-energy synchrotron radiation yields photoelectrons and Auger electrons. The differential cross section for ejecting electrons by either process should vary as

$$\frac{d\sigma(h\nu,\theta)}{d\Omega} = \frac{\sigma(h\nu)}{4\pi}[\ 1 + \beta(h\nu)P_2(\cos\theta)\ ] \qquad (1)$$

provided that the initial photoionization mechanism has electric dipole character and the initial system is randomly oriented.[1] Here $P_2(\cos\theta)$ is the second Legendre polynomial, θ is the angle between the polarization direction of the exciting light and the electron propagation direction, and $h\nu$ is the photon energy. The present work addresses experiments in which the electron yields are recorded as functions of electron kinetic energy. Most of the spectral features of interest are peaks in the electron yield associated with either photoelectrons or Auger electrons. For the former, the kinetic energy ε of a peak corresponding to a given orbital of binding energy E_B is

---

* C.M. Truesdale, S. Southworth, P.H. Kobrin, U.E. Becker, D.W. Lindle, H.G. Kerkhoff, P.A. Heimann, T.A. Ferrett, and D.A. Shirley, submitted to Phys. Rev. A (1983).

given by $\epsilon = h\nu - E_B$. For the latter, the kinetic energy of a given Auger channel is invariant with photon energy (post-collision interaction is negligible in this work). In both cases a complete description of the differential cross section can be given by the two functions $\sigma(h\nu)$ and $\beta(h\nu)$, which are called the "cross section" and "asymmetry parameter", respectively. They in turn can be determined by measuring $d\sigma(h\nu,\theta)/d\Omega$ at two known angles θ. Given the close relationship between $h\nu$ and ϵ, these parameters are often listed as $\sigma(\epsilon)$ and $\beta(\epsilon)$ for photoelectrons. Sometimes the notation $\sigma_A(h\nu)$ and $\beta_A(h\nu)$ is used to denote properties of Auger transitions. In addition, Dill et al.[2] have used the notation $\beta_m(h\nu)$ to denote the alignment in the initial state of an Auger transition. The asymmetry of each Auger transition is described by the product of an orientation parameter $\beta_m(h\nu)$ and a term dependent on the Auger decay process represented by the symbol A, where

$$\beta_A(h\nu) = \beta_m(h\nu)A. \qquad (2)$$

Here the A parameter is independent of the excitation energy $h\nu$.

For photon energies near the core-level binding energies of electrons in molecules, resonances in cross sections and associated variations in the asymmetry β are expected. A certain class of these resonances is associated with the scattering of the outgoing photoelectron by the molecular potential in a quasi-bound state. These are termed "shape resonances", and are expected to constitute

sensitive probes of the molecular potential. Although shape resonances for core-electron excitation in molecules have been the subject of extensive theoretical investigation, notably by Dehmer, Dill, and co-workers,[2] they have not to our knowledge been observed by a direct experiment. We define a "direct" experiment as one in which both the energy and direction of the incoming photon and the outgoing electron are defined. In this paper, and an earlier preliminary report on CO, we describe the first direct measurements of the core-level shape resonances in the photoelecton cross section $\sigma(\varepsilon)$ and Auger cross section $\sigma_A(h\nu)$ for several molecules, and the first measurements of any kind on the photoelectron asymmetry $\beta(\varepsilon)$ and Auger asymmetry $\beta_A(h\nu)$ of these same transitions.

Our results can be compared with related measurements in several cases. These include photoabsorption,[3,4] electron energy loss,[5-10] electron-ion coincidence,[11] Auger yield,[12] and valence-orbital photoemission.[13]

Several theoretical predictions are available in addition to the MSMXα results. The Stieltjes-Tchebycheff Moment Theory (STMT) constructs ground state wavefunctions of Hartree-Fock quality from which static exchange potentials are approximated to account for the nonlocal properties of the core hole states. Pseudospectra are then produced that account for the frequencies and oscillator strengths of various transitions to discrete valence and continuum valence-like orbital channels. Padial et al.[14-15] used the STMT formalism to calculate the partial cross sections for C1s and O1s photoemission

from CO and CO_2. Recently a Hartree-Fock static exchange calculation by Lucchese and McKoy[16] has yielded the C1s and O1s cross sections $\sigma(\epsilon)$ and asymmetry parameters $\beta(\epsilon)$ for CO_2. This calculation comes near to determining the correct ab-initio ground state and continuum wavefunctions.

Our spectrometer has been described previously.[17] A double-angle-time-of-flight (TOF) spectrometer detects ejected electrons by means of microchannel plates. The gas samples are excited by photons delivered to Beam Line III-1 at the Stanford Synchrotron Radiation Laboratory. One detector is placed at 0° and another is placed at 54.7° relative to the photon polarization axis. Relative cross sections are determined from the electron intensities measured with the 54.7° detector, and the asymmetry parameters are found from the ratio of signals measured at 0° and 54.7°.

Cross sections and asymmetry parameters are corrected in a calibration procedure explained in Ref. 18. Briefly, the asymmetry parameters are corrected for the relative efficiency of the two detectors as a function of the kinetic energy of detected electrons. Comparisons are made between accepted literature values for the asymmetry parameters of Ne 2s and Ne 2p photoelectrons for photon energies of 50-300 eV and the ratio of their measured intensities at 0° and 54.7°.[19] A small (up to several percent) unpolarized component of the synchrotron radiation and any small misalignment of the photon beam that intersects the gas sample in the interaction region would thereby be corrected for in the final determination of

the asymmetry parameters.[18] Likewise, our measured relative cross sections have been corrected for the (energy-dependent) transmission characteristics of the 54.7° detector by a comparison with known experimental cross sections and partial cross sections of Ne 2s and Ne 2p photoionization channels.[19]

Second-order light corrections for the C(KVV) Auger cross section $\sigma_A(h\nu)$ and asymmetry parameter $\beta_A(h\nu)$ were negligible because of the small observed intensity for the second-order C1s photoelectron peak. The cross sections $\sigma(\epsilon)$ and $\sigma_A(h\nu)$ for the O1s and the O(KVV) peaks measured with the second-order component of the light, and the first-order results, were scaled separately to the photoabsorption cross sections of Barrus and co-workers.[3]

Most spectra were collected for 1000 sec, the exceptions being those of the S2p and S(LVV) Auger peaks of OCS, for which the spectra were collected for 300 sec. In the CO, CO_2, CF_4, and OCS carbon and oxygen K-shell experiments, an aluminum window (1500Å thickness) isolated our chamber from the port of the ultra-high vacuum monochromator. A vitreous carbon window (1000Å) was used for the OCS sulfur L-shell experiments.

Stanford Synchrotron Radiation Laboratory provided tunable radiation from the grazing-incidence "grasshopper" monochromator,[20] which was operated with a 1200 line/mm holographic ruled grating. Second-order light was used to measure the O1s and O(KVV) electron peaks while simultaneously measuring the C1s and C(KVV) electron peaks with first-order light for CO and CO_2.

Excitation spectra of discrete subthreshold resonances (e.g., the $\sigma \rightarrow \pi^*$ type) for CO, CO_2, and OCS, and ($\sigma \rightarrow 3sa_1$) for CF_4 were used to calibrate the monochromator energy scale. The overall experimental resolution was determined by the observed widths of these resonances, which were larger than the natural line widths. The entrance and exit slit settings of the monochromator for the CO measurements (275 eV $\leq h\nu \leq$ 315 eV) were 20μ and 50μ, which yielded band passes of 0.5 and 2.0 eV FWHM. The 0.5 eV resolution measurements (275 eV $\leq h\nu \leq$ 290 eV) were performed over the Auger $\sigma \rightarrow \pi^*$ discrete transition. During the CO_2 measurements (270 eV $\leq h\nu \leq$ 340 eV) 50μ slits were used. The S2p and S(LVV) Auger experiments (155 eV $\leq h\nu \leq$ 190 eV) on OCS used 100μ slits with a monochromator resolution of 1 eV, and the remaining studies used 100μ slits which corresponds to a bandpass of 4 eV. In each case an additional 3 percent of the kinetic energy of the electrons arising from the geometry of our spectrometer must be factored in to calculate the overall resolution of our measurements. The oxygen measurements performed with first-order light for CO were carried out with a monochromator bandpass of 5 eV, and the second-order oxygen measurements for CO and CO_2 were performed with 4.0 eV monochromator resolution. For some spectra, the electrons were retarded for 14.4 cm of the total 28 cm path length of travel, before being detected by the microchannel plates, by means of retarding cages inside the flight tubes of our detectors. The resolution and separation of photoelectron and Auger peaks were significantly improved by this procedure.

There are five sections to follow. The results and discussion for CO, CO_2, CF_4, and OCS will be presented in Sections B-E, respectively, and conclusions will be presented in Section F.

B. CO Results and Discussion

Some of the CO shape resonance results reported here were presented and discussed in an earlier report.[21] We include them here for completeness, but refer the reader to that report for its complementary discussion.

The ground state electronic configuration of CO is $(1\sigma^2 2\sigma^2 3\sigma^2 4\sigma^2 1\pi^4 5\sigma^2)\ ^1\Sigma^+$. The 1σ orbital is basically O1s-like (E_B = 541.2 eV), the 2σ is C1s (E_B = 295.9 eV[22]), and the other four orbitals are the valence orbitals of CO.

Two time-of-flight (TOF) spectra, converted to kinetic energy scales, are shown in Figs. 1 and 2. The spectrum in Fig. 1 was collected with a retarding voltage of 150 eV. The $(5\sigma^{-1})$, $(1\pi^{-1})$, and the $(4\sigma^{-1})$ photoelectron peaks, with binding energies of 14.9, 17.6, and 20.5 eV, respectively, are unresolved, but the $(3\sigma^{-1})$ peak is distinct, with a binding energy of 35.4 eV. Peaks corresponding to the C(KVV), the C1s(from 2nd order), the O1s(from 3rd order), and the O(KVV) peaks are also observed. A spectrum taken with no retarding potential is shown in Fig. 2. The C1s and O1s peaks are evident, and the identities of the other features can be inferred from Fig. 1.

We note that the C(KVV) Auger peaks have kinetic energies of ~220

to 273 eV. Using the notation of Moddeman et al.,[23] the B-1 peak ($5\sigma^{-1}$, $1\pi^{-1}$ final state) with a kinetic energy of ~255 eV is convoluted with B-3 ($5\sigma^{-2}$) and the weak B-2 Auger band ($4\sigma^{-1}$, $5\sigma^{-1}$).[24,25] The other structures observed by Moddeman, et al. (B-6 to B-10, and C-1 to C-3) are grouped together into the peaks shown by the B and C labels. The Auger bands labeled by Moddeman et al. as A-1 to A-11 (autoionization) have final kinetic energies corresponding to the kinetic energies of the ionized valence states, and cannot be unambiguously identified because of the presence of the valence ionic channels. The oxygen Auger peaks have kinetic energies of ~ 413 to 517 eV. The largest O(KVV) peaks have been identified as the B-5 ($1\pi^{-2}$) and B-7 ($4\sigma^{-1}$, $1\pi^{-1}$) bands.[24] Our peak at a kinetic energy of ~ 495 eV corresponds to B-5 convoluted with B-7 (shake-up) and B-4, and the shoulder at ~ 500 eV is the B-1 ($5\sigma^{-1}$, $1\pi^{-1}$) band.[24] The results of ab-initio molecular Auger calculations by Agren[25] suggest that the large C(KVV) Auger peaks arise from the vacancies in the 5σ orbital, and that vacancies in the 3σ, 4σ, and 1π orbitals dominate the O(KVV) Auger spectrum for CO.

Asymmetry parameters for the C(KVV) Auger electrons of CO are shown in Fig. 3. The asymmetry parameters are set out in Table I. Spectra excited by photons of energies near the C1s edge energy contained valence orbital photoelectron peaks that overlapped with, and were unresolvable from, the Auger peaks. However, extrapolation from spectra taken with photon energies too low to excite the C1s discrete resonances enabled us to estimate with some confidence the

effects of the valence photoelectrons on the Auger partial cross sections. In some cases a partial deconvolution of these peaks was attempted, but in most cases the peaks arising from higher order light and the first three valence photoelectron peaks could be only partially deconvoluted from the C(KVV) peaks, and some $(3\sigma^{-1})$ component is unavoidably still included in the C(KVV) results. The effective asymmetry parameter $\beta_T(h\nu)$ for the sum of the C(KVV), the valence states, and the small second order C1s peak is also given in Table I. Of course the transitions represented by $\beta_T(h\nu)$ vary with $h\nu$. For example, for $h\nu < 280$ eV, $\beta_T(h\nu)$ corresponds to the effective asymmetry parameter for the sum of the valence states, because at these photon energies the C(KVV) Auger transitions do not exist.

The cross section $\sigma_A(h\nu)$ for the $2\sigma \rightarrow 2\pi(\pi^*)$ resonance, at 287.3 eV photon energy,[5,6,10,11] has been scaled to the integrated oscillator strength over this resonance given by Tronc et al.[5] This discrete resonance is over an order of magnitude more intense than the continuum excitations, which lie above the C1s binding energy of 295.9 eV. For photon energies above the discrete resonance, the C(KVV) curve was scaled by a constant factor, to agree with the C1s photoelectron cross section at 315 eV, which was normalized to the electron-ion coincidence measurements, shown by the dashed curve. The continuum region shows structure arising from the C1s photoelectron shape resonance, as discussed before. In normalizing the Auger yield to the C1s cross section we have neglected the fluorescence yield,

which could be accounted for in a more precise study.

The asymmetry parameter $\beta_A(h\nu)$ for the C(KVV) channel in CO is nearly zero over the entire region where measurements were taken. The exception is near 295 eV. The published electron energy loss measurements[10] showed a strong discrete resonance near this energy. Our data indicate that in this resonance the excited CO molecule is strongly oriented, leading to an asymmetry in the C(KVV) Auger channel. No further interpretation is warranted, because the nature of the discrete resonance at 295 eV is not well established. Turning now to the 287.3 eV resonance, the orientation parameter for the excited state following the $\sigma \rightarrow \pi^*$ transition is predicted to have a value of -1.[2] This prediction has essentially been confirmed by Stöhr et al.[12] for CO adsorbed and oriented on a surface. It seems inescapable that CO^* is strongly oriented in the π resonance excited state. There are two possible ways to reconcile this orientation with our observations that the kinetic energy-integrated C(KVV) asymmetry parameter $\beta_A(h\nu)$ is essentially zero at $h\nu$ = 287.3 eV. First, the A_j factors for the various Auger transitions of fractional strength f_j could have values that would average out the Auger asymmetry parameter $\beta_A(h\nu)$ to zero, according to

$$\overline{\beta_A(h\nu)} = \beta_m(h\nu)\sum_j A_j f_j(h\nu) \qquad \left(\frac{-1}{2} \leq A_j \leq 1\right) \quad (3)$$

This can also explain the discrepancy between the calculated orientation parameter $\beta_m(h\nu)$ and our asymmetry parameter $\beta_A(h\nu)$

values for the C(KVV) channel above the C1s threshold at 295.9 eV. Well-resolved Auger spectra will have to be measured to test this possibility. Our own attempts to obtain such spectra will be described below, after we address the alternative explanation for a near-zero asymmetry.

The above idea that the Auger asymmetry β_A is near zero because of cancellation of asymmetries strains our credulity, especially if it must be invoked twice; i.e., for the π resonance and again for the continuum states. An attractive alternative explanation for the near-zero β of the π resonance is the "spectator" model, in which the excited electron retains the orientation information in a π^* orbital but is not significantly involved in subsequent Auger decays. The molecular "core" would then behave somewhat like an atom with a K-shell hole and exhibit no asymmetry in its Auger decay. This model was discussed earlier.[21]

In an attempt to test the first explanation, we used selected retarding potentials to study the kinetic energy distribution of the Auger electrons for photon energies above and below the C1s threshold at 295.9 eV. Two typical spectra, excited by photons on resonance at 287.8 eV and above threshold at 296.8 eV, are shown in Fig. 4. Retarding potentials of 100 V and 150 V were applied to collect the 287.8 eV and 296.8 eV spectra, respectively. The large C(KVV) peak in the 287.8 eV spectrum, which corresponds to the B-1 band $(5\sigma^{-1},1\pi^{-1})$ in the 296.8 eV spectrum, has a kinetic energy of around 12.5 eV higher than its counterpart, because the initially excited electron is

still present. An electron-electron coincidence measurement by T.D. Thomas et al.[26] has shown a similar shift between high resolution C(KVV) Auger spectra for CO and for comparable measurements by Ungier et al.[27] for the N(KVV) Auger of N_2 spectra with and without the excited electron present. Because of the low resolution of our spectra we could only confirm that the mean energies and overall shapes of the spectra were different. We could not establish whether or not the asymmetry varies with kinetic energy across a spectrum.

The results for the C1s photoelectron channel are presented in Fig 5. Our relative cross sections were scaled to the electron-ion coincidence measurements of Kay et al.,[11] shown by the open circles. The C1s cross section shows a weak shape resonance maximum centered around 306 eV, in good agreement with the results of Kay et al.[11] and with predictions of the STMT calculation,[14] shown by the solid curve. In the STMT work two major subchannel excitations were invoked to describe the 2σ K-shell excitations. Those were the $2\sigma \rightarrow k\sigma$ and the $2\sigma \rightarrow k\pi$ continuum transitions. The $\ell=3$ partial wave in the $\sigma \rightarrow k\sigma(\epsilon f)$ transition has been suggested as being responsible for the σ shape resonance.[28-31] Also shown in Fig. 5 is a dashed curve representing the MSMXα prediction.[31] This curve shows a maximum at the right energy, but its width exceeds the experimental value and its contrast ratio is about twice the experimental result.

The asymmetry parameter $\beta(\epsilon)$ for the C1s photoelectron confirms the existence of a shape resonance with a weak minimum at 303 eV. The variation of the measured $\beta(\epsilon)$ falls between the predictions of the

localized-hole MSMXα calculations of Dill et al.[30], shown by the solid curve, and Grimm,[32] shown by the dashed curve. The overall shapes of the calculated $\beta(\varepsilon)$ curves are in very good agreement with the present results, except for predicting a contrast ratio larger than is observed.

The cross section and asymmetry parameter of the unresolved peak, which included the X, A, and B states of CO^+ derived by ionization of 5σ, 1π, and 4σ electrons, and the C1s peak in second order, was also derived from our data. The cross section showed little variation with photon energy in the range $h\nu$ = 270–315 eV, and β ranged between 1.5 and 2. The data showed a lot of scatter because of the difficulty of deconvoluting these peaks from the Auger structure, but their overall behavior assured us that the curves derived for the Auger peaks were entirely due to the behaviour of those peaks.

The C1s(2nd order) peak could be deconvoluted in our spectra for $h\nu$ = 308–314 eV; i.e., for 2nd order photon energies ranging from 616 to 628 eV. In those five spectra the asymmetry parameter $\beta(\varepsilon)$ was determined, the mean value being $\beta = 2.03 \pm 0.11$. Of course $\beta = 2$ is expected for an atomic $ns \rightarrow \varepsilon p$ transition. In the high kinetic energy regime it may be plausible to treat the C1s excitations in molecular CO in an atomic model, because the scattering dynamics should not include resonances and the outgoing electron would have little interaction with the molecular potential.

The oxygen Auger results are dispayed in Fig. 6. The data are incomplete because the oxygen edge was a low-priority secondary

objective of this study, as a consequence of the poor performance of the monochromator at this energy. Our results were derived by using both first-order and second-order light. No data were taken below $h\nu$ = 540 eV in either order, and the range $h\nu$ = 550–570 eV was largely missed, thereby precluding a definitive study of shape resonance phenomena. The results are nonetheless of some interest.

The O(KVV) cross section closely mimics the O1s cross section (to be discussed later), as it should. The O(KVV) asymmetry parameter was easy to work up because the peak fell at a high kinetic energy and was well separated from other features. Throughout the range $h\nu$ = 560–630 eV the data lie in the range β = -0.1 to 0.3 with no real trends, and a horizontal straight line fits the data within their statistical accuracy, yielding the value $\beta = 0.10 \pm 0.02$.

Our six points near threshold, in the range $h\nu$ = 545–555 eV, show a larger β, in the range 0.3–0.5. It seems probable that these points provide the first evidence for an Auger shape resonance, as predicted by Dill et al.[2] Their calculated curve for the orientation parameter β_m is shown in Fig 7. Clearly more work is needed on this question.

The results for the O1s peak are presented in Fig. 7. There is general agreement among our cross section $\sigma(\varepsilon)$ data, photoabsorption measurements,[3] and the STMT calculation of Padial et al.[14] Our measurements based on first-order and second-order light, after being corrected for transmission efficiency, were scaled to the photoabsorption data at 545 eV, and 562 eV, respectively, because of a

small overlap in energies for the two sets of measurements. The O1s cross section $\sigma(\epsilon)$ clearly shows a shape resonance near 550 eV.

The dearth of measurements between 550 and 570 eV prevents our observing the minimum in the O1s asymmetry $\beta(\epsilon)$ predicted by the localized-hole MSMXα calculations of Grimm[32] and Dill et al.[30]. However, we find that $\beta(\epsilon)$ increased rapidly from 0.7 at $h\nu$ = 545 eV toward an asymptotic value above 1.5 by $h\nu$ = 570 eV. Whether there is more structure in the range $h\nu$ = 550–570 eV is unknown. At higher energies our data appear to approach an asymptotic value of β = 1.6 ± 0.1. The MSMXα calculations[30,32] show good agreement with this result, approaching an asymptote this high or higher. Similar behavior was observed both experimentally and theoretically for the C1s asymmetry.

Shake-up structure is observed near the O1s peak. A TOF spectrum taken with second-order light at $h\nu$ = 630 eV, converted to an energy scale, is shown in Fig. 8. The shake-up structure labeled "S" is probably the $1\pi \rightarrow 2\pi$ shake-up transition. We find that this structure is present at 13.0 ± 3.0 percent of the O1s main-line intensity. Carlson et al.[33] reported that this state has ~10 percent of the O1s intensity. Aarons et al.[34] performed an unrestricted Hartree-Fock (UHF) calculation to assign shake-up thresholds and intensities in the high-energy limit. They predicted that the $1\pi \rightarrow 2\pi$ shake-up peak should lie 16 eV above the O1s peak and would have 15.4 percent of the O1s intensity. The agreement between this calculation and our measurements is very good.

C. CO_2 Results and Discussion

The ground state electronic configuration of CO_2 can be written $1\sigma_g^2 1\sigma_u^2 2\sigma_g^2 3\sigma_g^2 2\sigma_u^2 4\sigma_g^2 3\sigma_u^2 1\pi_u^4 1\pi_g^4 \quad {}^1\Sigma_g^+$. The $1\sigma_g$ and $1\sigma_u$ orbitals (unresolved in this work) are linear combinations of atomic O1s orbitals with an average binding energy of 541.2 eV. The $2\sigma_g$ orbital is basically a C1s atomic orbital with a binding energy of 297.5 eV. The remaining molecular orbitals have binding energies below 50 eV, and were not studied in this work. A spectrum is shown in Fig. 9. The C1s photoelectron and C(KVV) Auger cross section results were scaled at 305 and 302 eV, respectively, to the C1s partial cross sections derived by the electron energy loss studies of Wight and Brion,[8] which were themselves scaled to agree at 300 eV with the STMT calculations of Padial et al.[15]. As in CO, all of the O1s and O(KVV) measurements in CO_2 were taken with the second-order light, and our relative partial cross sections were scaled to the photoabsorption measurements of Barrus et al.[3]

Results for the C(KVV) asymmetry parameter are presented in Table II. The C(KVV) peak is convoluted with the valence photoelectron peaks: a partial deconvolution was achieved. The Auger asymmetries for the C(KVV) and O(KVV) channels of CO_2 are effective values integrated over the unresolved KVV Auger channels, similar to the results for the Auger peaks in CO. As for the CO C(KVV) $\beta_A(h\nu)$ results, the effective asymmetry parameter in CO_2 for the sum of the C(KVV) peak, the valence states, and the second-order C1s peak,

$\beta_T(h\nu)$, is also found in Table II. To our knowledge, there are no published integrated cross sections over the discrete $2\sigma_g \rightarrow 2\pi_u(\pi^*)$ transition against which we can normalize our Auger cross sections.

The time-of-flight spectrum of CO_2 in Fig. 9 has been converted to a linear kinetic energy scale, with the various peaks identified in the Figure. The dominant C(KVV) peaks have been assigned as having mainly $(1\pi_u^{-2})$ and $(4\sigma_g^{-1},1\pi_g^{-1})$ final states.[25] Some of the O(KVV) peaks of CO_2 still do not have unambiguous assignments, but the $1\pi_g^{-2}$ hole states should account for most of the high kinetic energy Auger peaks.[25]

The derived parameters for CO_2 are plotted in Figures 10-13. The format remains the same, where filled circles represent the present experimental measurements. The open circles with the C1s $\sigma(\varepsilon)$ results and the dashed curve with C(KVV) Auger cross section $\sigma_A(h\nu)$ are the electron energy loss measurements of Wight and Brion,[8] and the open circles shown with the $\sigma_A(h\nu)$ for the O(KVV) channel denote photoabsorption measurements.[3] The solid curves presented with the $\sigma(\varepsilon)$ and $\sigma_A(h\nu)$ data are the STMT results,[15] and the dashed curves represent the HF static exhange calculations.[16] For the $\beta(\varepsilon)$ curves, the solid curve represents the HF static exchange results, the dotted curve represents the localized MSM calculation of Grimm,[32] and the dashed curve represents the unlocalized-hole MSMXα calculations of Grimm.[32]

In Fig. 10 the CO_2 C(KVV) Auger cross section $\sigma_A(h\nu)$ shows a discrete resonance transition [$2\sigma_g \rightarrow 2\pi_u(\pi^*)$] centered near 290 eV and the broad shape resonance [$2\sigma_g \rightarrow 4\sigma_u(\sigma^*)$] with its maximum near 310 eV. Our C(KVV) Auger cross section $\sigma_A(h\nu)$ results were scaled to the electron energy loss results at 302 eV.

The CO_2 C(KVV) Auger asymmetry parameter $\beta_A(h\nu)$ is also shown in Fig. 10. At the $2\pi_u(\pi^*)$ resonance $\beta_A(h\nu)$ is small, similar to the result for the C(KVV) channel of CO at the $2\pi(\pi^*)$ resonance, but apparently nonzero. As in CO, the remainder of the asymmetry points must be interpreted carefully. The highest asymmetry values fall at energies for which the Auger peak intensity is very weak; i.e., $h\nu$ = 296, 300, and > 330 eV. These high values cannot be interpreted with any confidence, but probably arise from other channels, e.g., valence orbitals. In the range $300 < h\nu < 325$ eV, $\beta_A(h\nu)$ shows scatter well outside of statistics, but again (as for CO) appears to be slightly positive. The discussion given for the CO C(KVV) Auger asymmetry would also be appropriate for CO_2.

The results for the C1s photoelectron channel are presented in Fig. 11. The cross section $\sigma(\varepsilon)$ for the C1s peak of CO_2 was scaled in the same way as was the C(KVV) cross section. The σ shape resonance peaking at 312 eV is more evident than that of CO. Both of the theoretical models (HF static exchange and MSMXα) are fairly accurate in determining the shape of the peak in the cross section, but the energy of the broad shape resonance is calculated to lie 5–6 eV closer to threshold; i.e., at ε ~8 eV rather than the experimental

value of ϵ ~14 eV. Wight and Brion [8] suggested that the structure present at 301 eV is attributable to $1\pi_u$ shakeup ($1\pi_u \rightarrow 2\pi_u$). Both theories miss this structure.

The asymmetry $\beta(\epsilon)$ of the C1s peak in CO_2 is also more dramatic than for CO, appearing as a broad minimum centered around 318 eV. The HF static exchange calculation[16] (solid curve) is in better agreement in predicting the overall shape of $\beta(\epsilon)$ than is the unlocalized-hole MSMXσ calculation,[32] shown by the dashed curve. Nonetheless, the unlocalized-hole MSMXα predicts the energy position for the shape resonance minimum very close to our measurements. The localized-hole MSM calculation of $\beta(\epsilon)$ (dotted curve) for the C1s channel given by Grimm[32] predicts the shape resonance too close to threshold. Grimm suggested the C1s shape resonance is attributable to the ℓ=2,3 channels in the $2\sigma_g \rightarrow 4\sigma_u(\sigma^*)$ continuum transition.

The O(KVV) results are presented in Fig. 12. The cross section of the O(KVV) channel should be directly related to the O1s partial cross section when the photon energy used is above the O1s threshold. We shall use the Auger yield $\sigma_A(h\nu)$ for the O(KVV) channel of CO_2 to make comparisons to previous O1s cross section measurements and O1s theoretical models. The partial cross sections for the CO_2 O(KVV) were scaled to the O1s photoabsorption measurements of Barrus et al.[3] at 555 eV to yield absolute partial cross sections. The Auger yield $\sigma_A(h\nu)$ for the O(KVV) peak is then in excellent agreement in its energy dependence with the photoabsorption measurments. Barrus et al. stated that they observed a weak structure at ~580 eV in their absorption curve,

which was proposed to be related to shake-up structure. There also seems to be a weak structure present in our yield data. The $\sigma_A(h\nu)$ data are in total agreement with the photoabsorption results. Both theoretical studies predict the energy of the C1s shape resonance to be near 560 eV, but the STMT calculation is in closer quantitative agreement with the experiment in predicting the shape of the cross section.

The measured O(KVV) asymmetry parameter $\beta_A(h\nu)$, shown by the filled circles in Fig. 12, starts at a value near 0.3 at 550 eV, decreases to near zero at 575 eV, has a weak maximum at near 580 eV, and remains close to 0.1 from 600 eV to 680 eV. The possible structure near 580 eV corresponds to the same feature observed in the yield $\sigma_A(h\nu)$, and may be a result of shake-up.[3]

The asymmetry parameter $\beta(\varepsilon)$ for the O1s channel is shown in Fig. 13. It rises from 0.7 at 550 eV, to ~1.3 at 555 eV, continues to increase to 1.5, and remains at this value from 560 to 680 eV. Our results are sparse at the low energies (the region where both the HF static exchange and the localized-hole MSMXα calculations predict minima in $\beta(\varepsilon)$) and the monochromator resolution was poor in this region. Therefore, we cannot infer anything about a possible minimum for the asymmetry parameter.

After expanding the spectra around the O1s peak, O1s satellite structure was again observed. In Fig. 14 we present TOF spectra converted to an energy scale for a spectrum collected with the second-order light with an energy of 630 eV. The largest O1s shakeup

peak is located at about 16 eV above the O1s threshold. Allan et al.[35] have attempted an assignment of the total O1s shakeup structure of CO_2. They suggest that the two shake-up peaks at around 13.8 eV and 16.0 eV (referenced to the O1s main-peak) may arise from transitions between the excitations $4\sigma_g \rightarrow 5\sigma_g$ (14.5 eV), $1\pi_u \rightarrow 2\pi_u$ (15.2 eV), and the $3\sigma_u \rightarrow 4\sigma_u$ (15.5 eV). The branching ratio for the total O1s shake up intensity to the O1s main-line intensity is tabulated in Table III. Theoretical calculations[34] have indicated that ~20 percent of the intensity of the O1s main line is borrowed to produce the O1s satellite structures. The present average value for the branching ratio of the satellite peaks from ~11 to 22 eV above the O1s binding energy for photon energies between 592 and 632 eV is about 20 percent. Allan and co-workers[35] found that when CO_2 was excited by Mg Kα radiation (1254.6 eV) the sum of the O1s shake-up peaks accounted for about 17.5 percent of the intensity of the O1s photoelectron peak.

D. CF_4 Results and Discussion

The ground state electronic configuration of this tetrahedral molecule can be written: $1t_2^6 1a_1^2 2a_1^2 3a_1^2 2t_2^6 4a_1^2 3t_2^6 1e^4 4t_2^6 1t_1^6$, $^1A_1$.[36] The $1t_2$ and $1a_1$ molecular orbitals are described by a linear combination of F1s atomic orbitals. The $2a_1$ molecular orbital is formed almost entirely from a C1s atomic orbital with a binding energy of 301.8 eV. An electron spectrum of CF_4 excited by a photon beam of nominal (first-order) energy 318.8 eV is shown in Fig. 15. The

features present are the C1s peak, the C(KVV) peak, the valence photoionization channels, and the F(KVV) Auger peaks which arise from third-order light. We shall discuss only the C1s and C(KVV) peaks, which were observed in spectra taken at photon energies between 280 eV and 350 eV.

A discrete resonance occurs at 298 eV, which has been assigned as arising mostly from the $2a_1 \rightarrow 3sa_1$ Rydberg-type excitation, with small contributions from 3p and 3d Rydberg orbitals.[9] The derived parameters for the C1s and C(KVV) peaks of CF_4 are plotted in Fig. 16 and Fig. 17. In these figures, our derived partial cross sections are compared to the electron energy loss measurements of Wight and Brion[9], shown as open circles, and the photoabsorption results of Bachrach et al.,[4] illustrated by the solid lines. There are no theoretical or other experimental $\beta(\varepsilon)$ results for the C1s and C(KVV) channels of CF_4. A solid line is drawn through our data to show their trends more clearly.

The measured C(KVV) Auger cross sections $\sigma_A(h\nu)$ were scaled to the results of Bachrach et al.[4] at 302 eV. To account for the valence contributions to their results, their cross section below the discrete resonance energy (298 eV) was assumed to be the valence orbital contribution to the absorption curve and was subtracted prior to scaling our results. There is good agreement between the photoabsorption study and the present work. Differences observed between the two could be a result of our using a 4 eV bandpass in the monochromator, or the flux may not be well enough determined for the

1200 line/mm grating at the carbon edge in the CF_4 and OCS carbon K-shell experiments, which were performed 3 months after the CO and CO_2 experiments. The incident photon flux during the CF_4 and OCS experiments showed a stronger decrease at the carbon edge than observed for the CO and CO_2 measurements for which a new grating was used. The gratings become contaminated with carbon from hydrocarbon residuals in the vacuum of the SSRL beam lines. The intensity ratio of the discrete resonance to the continuum σ shape resonance in CF_4 lies between those observed in CO and CO_2.

The C(KVV) Auger asymmetry parameter $\beta_A(h\nu)$ for CF_4 is also shown in Fig. 16. The value of $\beta_A(h\nu)$ at the discrete resonance (298 eV) is near zero, as was the case for the C(KVV) peak in CO and CO_2. The apparent C(KVV) Auger asymmetry $\beta_A(h\nu)$ for photon energies above the C1s threshold in CF_4 lies in the range 0.2-0.3. It shows no strong variation in alignment in the proposed continuum shape resonance region around 315 eV. Because the $3a_1$ and $2t_2$ molecular orbitals are inextricably convoluted in our "Auger" peak, we are inclined tentatively to conclude that the nonzero value of the observed asymmetry of this peak may be largely ascribed to these orbitals.

The results for the C1s peak are presented in Fig. 17. The C1s relative cross section was scaled in a fashion similar to the C(KVV) yield, but at 310 eV. The yield $\sigma(\varepsilon)$ for the C1s peak has a broad shape resonance centered at 315 eV. The width of the resonance agrees with the electron impact measurements. Because of the difficulty in

digitizing the weak shape resonance region of the carbon K-shell for the electon impact measurements, those data are not plotted below 310 eV.

The C1s asymmetry parameter $\beta(\epsilon)$ of CF_4 starts at a value of ~0.6 at 305 eV, goes through a broad minimum value of about 0.3, steadily increases, and remains above 1.0 from 330 eV to 350 eV. The width of the minimum falls between the CO and CO_2 C1s results. This width is related to the depth of the potential barrier for the C1s photoelectron, and the ordering CO < CF_4 < CO_2 is consistent with the C1s molecular shape resonance contrast ratio having the same order. Theoretical studies of the C1s cross section $\sigma(\epsilon)$ and asymmetry parameter $\beta(\epsilon)$ are needed. These experimental results appear to be useful in qualitatively describing the systematics of shape resonance phenomena.

E. OCS Results and Discussion

The ground state electronic configuration of OCS can be written : $1\sigma^2 2\sigma^2 3\sigma^2 4\sigma^2 S2p^6 6\sigma^2 7\sigma^2 8\sigma^2 9\sigma^2 2\pi^4 3\pi^4$, $^1\Sigma^+$. We present angle resolved studies of the 3σ orbital, which corresponds to the C1s shell with a binding energy of 295.2 eV, and the sulfur $L_{2,3}(2p)$ doublet, with edges located at 170.6 and 171.6 eV. We have not attempted to resolve the two sulfur photoelectron peaks, and will adopt an average ionization threshold of 171 eV for this shell, which we henceforth denote as S2p. The carbon K-shell studies will be presented first, followed by the S2p and the S(LVV) results. Spectra of OCS can be found in Fig. 18 and Fig. 19.

The C(KVV) and C1s results are shown in Fig. 20 and Fig. 21. Our measurements will be compared to the electron energy loss measurements of Wight and Brion[37] and to the MSMXα calculation on the C1s channel given by Grimm[32]. From our earlier results, the $\beta(\varepsilon)$ values calculated for the localized hole potential model was expected to show better agreement with our measurements than the unlocalized-hole MSM calculation of Grimm, and indeed this is the case.

The $3\sigma \rightarrow 4\pi(\pi^*)$ discrete resonance have been observed by the electron energy loss measurements,[37] where the largest is centered at 288 eV. Wight and Brion have also observed discrete structure in the continuum range.[37] Grimm[32] has predicted that the excitations of the C1s electron into the continuum would show two shape resonances. The $\ell=3,4$ partial waves are expected to have delayed onsets. We therefore sought evidence to test this prediction.

The OCS C(KVV) Auger cross section $\sigma_A(h\nu)$, shown in Fig. 20, shows a large discrete transition below the C1s threshold. Above threshold there seems to be evidence for two maxima in the cross section, near 305 eV and 310 eV, which could be the f and g partial wave shape resonance features predicted by Grimm. The electron impact measurements,[37] which correspond to the solid curve have been scaled to our data at 291.2 eV. The electron energy loss measurements of Wight and Brion[37] are expanded (x3) to show the pre-edge discrete transitions for the C1s shell of OCS. The valence peaks intensities are apparent in the measurements below 285 eV photon energy. The

results of Wight and Brion[37] show a much smaller intensity for energies above the carbon K-edge than do the present data, probably because our measurements were performed with a 4 eV monochromator bandpass (FWHM) compared with the 0.5 eV electron energy resolution measurements of Wight and Brion.[37]

The C(KVV) Auger asymmetry parameter $\beta_A(h\nu)$ is presented in the bottom panel of Fig. 20. Again $\beta_A(h\nu)$ is nearly zero at the discrete π^* resonance, as was true for all the other molecules. The value of $\beta_A(h\nu)$ generally is between -0.2 and zero through the entire energy range, although there is an increase near the C1s threshold. This also is a common feature for the C(KVV) Auger peaks. It may be the consequence either of an alignment caused by other discrete transitions or of the valence contributions under the Auger peaks. A broad minimum is present in the asymmetry parameter near 310 eV, which may be a result of an alignment caused by a shape resonance.

The C1s cross section $\sigma(\varepsilon)$, shown in Fig. 21, has two maxima near 305 eV and 310 eV. Because these features were also observed for the C(KVV) peak, we are inclined to believe that these two maxima are really present. If the first and second maxima are indeed the f and g partial wave shape resonances, respectively, then the g-wave experiences a stronger resonance.

In the bottom panel of Fig. 21 the C1s asymmetry parameter $\beta(\varepsilon)$ data are shown. The localized-hole MSMXα results of Grimm are represented by the solid curve. We have lowered Grimm's curve by 0.3 units in beta. Although scatter is present in the data, it is clear

that the MSMXα calculation predicts the shape of our results. Two minima are observed, which would agree with the two shape resonances predicted by the MSMXα calculation.

The sulfur 2p shell has been studied previously in the region of the sulfur-L edges by optical absorption[38,39] and electron impact methods.[37] Our work is the first photoemission investigation for the sulfur 2p shell of carbonyl sulfide near the sulfur-L edges. We shall present results for the S2p and the S(LVV) channels. The S2p shell of OCS closely resembles the S2p shell in atomic sulfur. Deviations from atomic theoretical predictions might therefore highlight specifically molecular effects in S2p photoemission. The S(LVV) results will complement and test these interpretations.

The S2p photoemission measurements were performed over the photon energy range 160-190 eV. For these measurements, the time structure of the synchrotron radiation source was poor. It had a period of 195 ns between equally spaced bunches. Each bunch contained four pulses, spaced by ~2.8 ns. As a consequence the low kinetic energy peaks were substantially broadened. Because of the high count rate in these studies, spectra were obtained after 300 sec, yielding data with excellent counting statistics. The data are presented in Figs. 22 and 23, along with the electron energy loss results.[37] The solid curves in these figures are used only to connect data points. We have scaled the electron impact data to ours as previously described.

There is excellent agreement between the electron energy loss measurements and the relatively sparse data for the S(LVV) Auger

channel, as shown in Fig. 22. The large discrete resonances are associated with the excitation of the S2p electron to the $4\pi(\pi^*)$ unoccupied molecular orbital. The S(LVV) Auger cross section $\sigma_A(h\nu)$ has a maximum near 176 eV and slowly decreases at higher energies, following the electron loss curve quite well. There is a small feature near 179 eV. Wight and Brion reported observing a feature near 191 eV which they suggested might be caused by shake-up structure. We note these features because Allan et al.[35] have shown that S2p shake-up states lie 9.6 and 15.3 eV above the sulfur $L_{2,3}$ edges in OCS.

The $\beta_A(h\nu)$ results for the S(LVV) channel are also presented in Fig. 22. Table IV lists $\beta_A(h\nu)$ and $\beta_T(h\nu)$ values. The $\beta_A(h\nu)$ parameter includes contributions from OCS valence ionic channels, which could not be resolved out. It is therefore appropriate to note the trends in $\beta_A(h\nu)$, but not to draw any conclusions based solely on its precise value. The asymmetry parameter starts at a value near 1.0 below the S2p threshold and decreases sharply to near zero at 165 eV. Then $\beta_A(h\nu)$ has a small maximum near 167 eV (possibly due to alignment), decreases back to zero and varies little from 172 to 179 eV. The data near 179 eV suggest there is evidence for a small degree of alignment.

The S2p results are shown in Fig. 23. In the top panel the results of Wight and Brion[37] are again shown. The cross section of the S2p has a maximum at 176 eV and slowly decreases over the rest of the energy range. The comparisons made with this work have been

discussed in connection with the S(LVV) cross sections. Therefore those findings are identical for the S2p when the excitation energy is above the sulfur $L_{2,3}$ edges.

The OCS S2p asymmetry $\beta(\varepsilon)$ is presented in the bottom panel of Fig. 23. The data are connected by the solid curve only to emphasize trends. The asymmetry parameter has a minimum near 179 eV, increases to about 0.1, and again drops toward zero above 185 eV. The S(LVV) Auger cross section $\sigma_A(h\nu)$ showed a weak feature near 180 eV, which coincides with a threshold for a S2p shake-up state.

The changes of the S2p asymmetry parameter $\beta(\varepsilon)$ near 180 eV and above 185 eV suggests that $\beta(\varepsilon)$ might be sensitive to the population of shake-up states. In Fig. 24 a spectrum taken at 190 eV clearly shows the S2p shake-up peaks. We have determined that the binding energies of these states are about 9.5 (S2) and 15.0 eV (S1) above the sulfur 2p edges with intensities that are 6.3 ± 0.6 percent and 11.7 ± 0.7 percent of the S2p peak, respectively. Using Mg Kα radiation, Allan et al.[30] found that the shake-up peaks were 4.8 ± 1.5 percent and 6.4 ± 2.4 percent of as intense as the S2p peak.

We shall treat the molecular photoionization of the S2p shell in OCS in a "quasi-atomic" model, as if it were the ionization of an atomic 2p subshell. We exercise caution due to limitations in this approach because of molecular dynamical effects such as shape resonances, anisotropic ion interactions arising from the asymmetric molecular field, and higher angular momentum states must be included to describe fully the molecular system. In particular, we shall

discuss the dynamics of the measured $\beta(\varepsilon)$ parameter, using the atomic model presented by Manson.[40]

In the Cooper-Zare (C-Z) formalism,[41] the asymmetry parameter $\beta(\varepsilon)$ can be written

$$\beta(\varepsilon) = \frac{(\ell-1)R^2_{\ell-1}(\varepsilon) + (\ell+1)(\ell+2)R^2_{\ell+1}(\varepsilon) - 6\ell(\ell+1)R_{\ell-1}(\varepsilon)R_{\ell+1}(\varepsilon)\cos\Delta(\varepsilon)}{(2\ell+1)[\ell R^2_{\ell-1}(\varepsilon) + (\ell+1)R^2_{\ell+1}(\varepsilon)]} \tag{8}$$

The radial dipole matrix elements are given by $R_{\ell\pm1}$, where ℓ is the angular momentum of the specific orbital that is ionized and $\Delta(\varepsilon)$ accounts for the algebraic sum of the two phase differences for the interfering $\ell\pm1$ channels:

$$\Delta(\varepsilon) = [\delta_{\ell+1}(\varepsilon) - \delta_{\ell-1}(\varepsilon)] + [\eta_{\ell+1}(\varepsilon) - \eta_{\ell-1}(\varepsilon)] \tag{9}$$

The $\delta_{\ell\pm1}$ and $\eta_{\ell\pm1}$ terms correspond to the non-Coulomb and Coulomb phase shifts, respectively. It is assumed that both of the $\delta_{\ell\pm1}$ vary slowly with energy.[40] The Coulomb phase shift given by Manson is expressed as

$$\eta_{\ell+1}(\varepsilon) - \eta_{\ell-1}(\varepsilon) = \tan^{-1}[-(2\ell+1)/(\varepsilon^{1/2}\ell(\ell+1) - \varepsilon^{-1/2})] \tag{10}$$

For 2p ionization, $p \rightarrow \varepsilon d$ and $p \rightarrow \varepsilon s$ channels are allowed by the dipole selection rules. Using Eqs. (8) and (10) and defining the ratio $\rho(\varepsilon)=R_0(\varepsilon)/R_2(\varepsilon)$, we have

$$\beta(\varepsilon) = \frac{1 - 2\rho(\varepsilon)\cos\Delta(\varepsilon)}{1 + .5\rho(\varepsilon)^2} \quad . \tag{11}$$

Assuming $\delta_s(0) \approx 2\pi$ and $\delta_d(0) \approx 0$, and that both vary slowly with energy, the $\cos\Delta(\varepsilon)$ can be written approximately as

$$\cos\Delta(\varepsilon) = \cos[\tan^{-1}(-3\varepsilon^{1/2})/(2\varepsilon-1)] \tag{12}$$

Hence the radial matrix element ratio $\rho(\varepsilon)$ can be determined as the solution of the quadratic equation

$$\rho(\varepsilon)^2 + \rho(\varepsilon)\frac{4\cos\Delta(\varepsilon)}{\beta(\varepsilon)} + 2 - \frac{2}{\beta(\varepsilon)} = 0 \tag{13}$$

which are

$$\rho(\varepsilon) = \frac{-2\cos\Delta(\varepsilon)}{\beta(\varepsilon)} \pm \left[\frac{4\cos\Delta(\varepsilon)^2}{\beta(\varepsilon)^2} + \frac{2}{\beta(\varepsilon)} - 2 \right]^{1/2} \tag{14}$$

An examination of $\rho(\varepsilon)$ requires that the positive root be taken. Using this solution for $\rho(\varepsilon)$, together with our $\beta(\varepsilon)$ values, we have determined that the value of $\rho(\varepsilon)$ is about 0.5. This confirms that the matrix element for the $p \rightarrow \varepsilon s$ channel is always smaller than for the $p \rightarrow \varepsilon d$ channel, as suggested by Manson.[40]

The coulomb phase shift difference and asymmetry parameter determined using the quasi-atomic model is shown in Fig. 25. The values for radial matrix element branching ratio $\rho(\varepsilon)$ lie between 0.40 and 0.54. The $p \rightarrow \varepsilon s$ channel contribution to photoionization should

generally decrease slowly with increasing excitation energy. Therefore deviations from that behavior probably arise from explicit molecular structural effects. In Fig. 25 it is evident that the radial matrix branching ratio $\rho(\epsilon)$ shows abrupt increases near 179 eV and 186 eV, energies that correspond to the edge energies of the two strong satellites.

Using the atomic non-Coulomb phase shifts provided by Manson[42] the same quasi-atomic calculation was performed. It was determined that the radial matrix element ratio increased very rapidly over the photon energy range of 174-190 eV. By 187 eV the ratio of the dipole matrix elements is larger than 10. This suggests that the rise in the $p \rightarrow d$ non-Coulomb phase shift predicted from the atomic calculation of Manson[42] is increasing too rapidly, which may show that the potential barrier in OCS prevents the rise in the $p \rightarrow d$ non-Coulomb phase shift from occuring over the energy range of $h\nu$ = 174-190 eV. The Coulomb phase shift differences, asymmetry parameter, and the radial matrix element ratio calculated by the two above methods are listed in Table V.

If the $p \rightarrow \epsilon d$ channel is correlated with the S2p satellite states, the radial matrix branching ratio $\rho(\epsilon)$ could possibly increase as these new channels were opened. This would imply either that the $p \rightarrow \epsilon d$ channel had decreased or that the $p \rightarrow \epsilon s$ channel was enhanced. Correlation effects for the $5p^6$ sub-shell of Xe have been observed experimentally.[43,44] Amusia and Ivanov[45] have accounted for the correlation effects on the $5p \rightarrow \epsilon s$ and $5p \rightarrow \epsilon d$ channels using the random-phase approximation with exchange. It was found that the

photoionization cross section for the 5p shell was only weakly affected by correlation to the 4d shell, but larger changes were observed in the angular asymmetry parameter $\beta(\epsilon)$ of the 5p.[46] A similar correlation for OCS in the S2p shell and the 3π and 8σ molecular orbitals could explain the peculiar variation of $\rho(\epsilon)$ and $\beta(\epsilon)$ at the S2p satellite threshold energies. A theoretical study of the effect of shake-up states on the S2p ionization channels is warranted to explain fully the observed variation in cross section $\sigma(\epsilon)$ and angular asymmetry parameter $\beta(\epsilon)$.

F. Conclusions

Many conclusions could be drawn from our experimental studies of the carbon K-shells of CO, CO_2, CF_4, and OCS, the oxygen K-shells of CO and CO_2, and the S2p shell of OCS. The following conclusions are representative rather than exhaustive.

(1.) The near-threshold electron distributions for the C1s, O1s, C(KVV) Auger, and O(KVV) Auger peaks of CO and CO_2, the C1s and C(KVV) Auger peaks of CF_4 and OCS, and the S2p and S(LVV) Auger peaks of OCS have been determined by measuring the cross sections and asymmetry parameters for these molecular systems.

(2.) Shape resonances were observed in both the cross section and asymmetry parameter for all of the C1s photoionization channels in every molecule. The C1s cross section and asymmetry parameter for CO_2 shows the most dramatic effects, in the ℓ=2,3 shape resonance region. The C1s measurements of OCS may show two shape resonances, where ℓ=3,4 partial waves would be the successive dominant ionic channels. The C1s results of CF_4 are described in the scope of shape resonance phenomena, although no theoretical predictions are available, because of similarities to the other molecules in the variation of the cross section and the asymmetry parameter.

(3.) The C(KVV) partial cross sections show both the discrete resonances below the C1s ionization thresholds and the shape resonances in the continuum. The Auger asymmetry parameter shows no strong alignment at the π discrete resonances of CO, CO_2, and OCS and the $3sa_1$ resonance of CF_4. Two alternative explanations were offered, of which a "spectator" excited electron is the more appealing. Higher-resolution experiments are clearly needed. All the C(KVV) Auger peaks show small net alignments between the largest discrete resonance and the C1s ionization threshold which may be caused by other discrete resonances, although interference from valence shells is a problem. The shape resonances have small effects, or no effect, in the continuum region on the asymmetery parameter of the C(KVV) in all of the molecules. Small, but nonzero, asymmetries are observed. Again valence-shell interference cannot be ruled out.

(4.) The partial cross sections for the O(KVV) and O1s peaks of CO and CO_2 clearly show the O1s shape resonance. The asymmetry parameter of the O(KVV) of CO shows an alignment in the shape resonance region.

(5.) The C1s photoionization cross section of CO_2 given by the electron-ion coincidence measurements of Kay et al.[11] is in good agreement with our results.

(6.) The electron energy loss results of Wight et al.[6] and Wight and Brion[8,9,37] in the vicinity of the carbon K-edge, oxygen K-edge, and sulfur $L_{2,3}(2p)$ edges, for the cross sections are in good agreement with the present measurements.

(7.) The photoabsorption measurements of Barrus et al.[3] for the oxygen 1s shell of CO and CO_2 are in excellent agreement with the present results.

(8.) The STMT partial cross sections of Padial et al.[14] for the C1s and O1s channels of CO are in excellent agreement with the results. For CO_2 the C1s shape resonance is located too close to threshold,[15] and the O1s cross section shape is only in qualitative agreement with the present results.

(9.) The partial cross sections and asymmetry parameters $\beta(\epsilon)$ predicted from the MSMXα calculations are in qualitative agreement with the experimental results.[30-32] This model works well in identifying possible shape resonance features and in some cases predicts the location of the shape resonances in good agreement with the experimental measurements, but some discrepancies are noticed in particular between the calculated O1s asymmetries in CO and CO_2 and the present results. The MSMXα results of Grimm[32] using the localized-hole potential model is generally in better

agreement with the results than is the unlocalized hole potential model.

(10.) The HF static exchange calculations by Lucchese and McKoy[16] for CO_2 show promise in correctly describing the C1s asymmetry parameter. The C1s photoionization cross section is predicted with the correct shape, but the maximum is located too close to threshold.

(11.) Our measured intensity ratio of an O1s shake-up feature to the O1s main line of CO at a photon energy of 630 eV is very nearly the same as that measured with Mg Kα radiation by Allan et. al.[35] The unrestricted Hartee-Fock calculation by Aarons et al.[34] predicted the ratio of the total shake-up peak intensity to the O1s main-line photoelectron peak to be about 20%, in reasonably good agreement with experiment.

(12.) The asymmetry parameter for the S2p channel of OCS may be sensitive to the production of S2p satellite peaks. We observed a peculiar variation in the asymmetry parameter at photon energy corresponding to threshold energies of satellite states.

(13.) A quasi-atomic calculation for the S2p channel in OCS, using the Cooper-Zare model, was useful in determing the ratio of

the two radial matrix elements $\rho(\varepsilon)$ from the asymmetry parameter and the phase shift differences for the εs and εd ionization channels. The unusual behavior of $\rho(\varepsilon)$ may be related to correlation effects between the S2p and the 3π and 8σ molecular orbitals, by analogy to similar phenomena in atoms.

References

1. C.N. Yang, Phys. Rev. 74, 764 (1948).
2. D. Dill, J.R. Swanson, S. Wallace, and J.L. Dehmer, Phys. Rev. Lett. 45, 1393 (1980).
3. D.M. Barrus, R.L. Blake, A.J. Burek, K.C. Chambers, and A.L. Pregenzer, Phys. Rev. A 20, 1045 (1979).
4. R.Z. Bachrach, F.C. Brown, A. Bianconi, and H. Petersen, Stanford Synchrotron Radiation Report No. 77/16.
5. M. Tronc, G.C. King, R.C. Bradford, and F.H. Reed, J. Phys. B: Atom. Molec. Phys. 9, L555 (1976).
6. G.R. Wight, C.E. Brion, and M.J. van der Wiel, J. Electron Spectrosc. Relat. Phenom. 1, 457 (1972/73).
7. M.J. van der Wiel, Th. M. El-Sherbini, and C.E. Brion, Chem. Phys. Lett. 7, 161 (1970).
8. G.R. Wight and C.E. Brion, J. Electron Spectrosc. Relat. Phenom. 3, 191 (1974).
9. G.R. Wight and C.E. Brion, J. Electron Spectrosc. Relat. Phenom. 4, 327 (1974).
10. A.P. Hitchcock and C.E. Brion, J. Electron Spectrosc. Relat. Phenom. 18, 1 (1980).
11. R.B. Kay, Ph. E. van der Leeuw, and M.J. van der Wiel, J. Phys. B: Atom. Molec. Phys. 10, 2513 (1977).

12. J. Stöhr, K. Baberschke, R. Jaeger, R. Treichler, and S. Brennan, Phys. Rev. Lett. 47, 381 (1981).

13. C.L. Allyn, T. Gustaffson, and E.W. Plummer, Chem. Phys. Lett. 4, 127 (1977); C.L. Allyn, T. Gustaffson, and E.W. Plummer, Solid State Commun. 24, 531 (1977).

14. N. Padial, G. Csanak, B.V. McKoy, and P.W. Langhoff, J. Chem. Phys. 69, 2982 (1978).

15. N. Padial, G. Csanak, B.V. McKoy, and P.W. Langhoff, Phys. Rev. A 23, 218 (1981).

16. R.R. Lucchese and B.V. McKoy, Phys. Rev. A 26, 1406 (1982).

17. M.G. White, R.A. Rosenberg, G. Gabor, E.D. Poliakoff, G. Thornton, S. Southworth, and D.A. Shirley, Rev. Sci. Instrum. 50, 1288 (1979).

18. S. Southworth, C.M. Truesdale, P.H. Kobrin, D.W. Lindle, W.D. Brewer, and D.A. Shirley, J. Chem. Phys. 76, 143 (1982).

19. F. Wuilleumier and M.O. Krause, J. Electron Spectrosc. Relat. Phenom. 15, 15 (1979).

20. F.C. Brown, R.Z. Bachrach, and N. Lien, Nucl. Instrum and Meth. 152,73 (1978).

21. C.M. Truesdale, S. Southworth, P.H. Kobrin, U. Becker, H.G. Kerkhoff, and D.A. Shirley, submitted to Phys. Rev. Lett.

22. K. Siegbahn, C. Nordling, G. Johannson, J. Hedman, P.F. Heden, K. Hamrin, U. Gelius, T. Bergmark, L.O. Werme, R. Manne, and V. Baer, ESCA Applied to Free Molecules, North-Holland Publ. Co., Amsterdam, 1969.

23. W.E. Moddeman, T.A. Carlson, M.O. Krause, B.P. Pullen, W.E. Bull, and G.K. Schweitzer, J. Chem. Phys. 55, 2317 (1971).

24. J.A. Kelber, D.R. Jennison, and R.R. Rye, J. Chem. Phys. 75, 652 (1981).

25. H. Agren, J. Chem. Phys. 75, 1267 (1981).

26. Private communication with T. Darrah Thomas, Oregon State University, Corvallis, Oregon 97331.

27. L. Ungier, J.K. Gimzewski, and T.D. Thomas, Proc. X-82 Conf. on Atomic Inner Shell Phys. Eugene, Abstracts, 245 (1982).

28. J.L. Dehmer and D. Dill, Phys. Rev. Lett., 35, 213 (1975).

29. J.L. Dehmer and D. Dill, J. Chem. Phys. 65, 5327 (1976).

30. D. Dill, S. Wallace, J. Siegel, and J.L. Dehmer, Phys. Rev. Lett. 42, 411 (1979).

31. J.L. Dehmer and D. Dill, Argonne National Laboratory Report (ANL-77-65) p. 65.

32. F.A. Grimm, Chem. Phys. 53, 71 (1980).

33. T.A. Carlson, M.O. Krause, and W.E. Moddeman, J. de Physique 32, C4-76 (1971).

34. L.J. Aarons, M. Barber, M.F. Guest, I.H. Hillier, and J.H. Mc Cartney, Mol. Phys. 26, 1247 (1973).

35. C.J. Allan, U. Gelius, D.A. Allison, G. Johansson, H. Siegbahn, and K. Siegbahn, J. Electron Spectrosc. Relat. Phenom. 1, 131 (1972/73).

36. C.R. Brundle, M.B. Robin, and H. Basch, J. Chem. Phys. 53, 2196 (1970).

37. G.R. Wight and C.E. Brion, J. Electron Spectrosc. Relat. Phenom. 4, 327 (1974).

38. L.N. Mazlov, A. P. Sadovskii, V.M. Bertenev, K.E. Mironov, T.I. Guzhavina, and L.I. Chernyavskii, Zh. Struct. Chem. 13, 859 (1972); (J. Struct. Chem. 13, 802 (1972))

39. A.S. Vinogradov and T.M. Zimkina, Opt. Spectrosk. 31, 685 (1971) (Opt. Spectrosc. (U.S.S.R.) 31, 364 (1971)).

40. S.T. Manson, J. Electron Spectrosc. Relat. Phenom. 1, 413 (1972/73).

41. J. Cooper and R.N. Zare, Lectures in Theoretical Physics, edited by S. Geltman, K.T. Mahanthappa, and W.E. Britten (Gordon and Breach, New York) Vol XI. - C pp. 317-337 (1969).

42. S.T. Manson, Phys. Rev. 182, 97 (1969).

43. G.V. Marr, in Photoelecton Emission: Proceedings of the Daresbury Study Weekend, 6-7 March 1976, DL/SRF/128 p. 81.

44. S. Southworth, U. Becker, C.M. Truesdale, P. Kobrin, D.W. Lindle, and D.A. Shirley, to be published in Phys. Rev. A.

45. M. Ya. Amusia and N.A. Cherepkov, Case Studies in Atomic Physics 5, 47 (1975).

46. M. Ya. Amusia and N.A. Cherepkov, Phys. Lett. 59A, 194 (1976).

Table I. CO C(KVV) Auger asymmetry parameter.

$h\nu$(eV)	$\beta_A(h\nu)$	$\beta_T(h\nu)$
275.8	------	1.08(9)[a]
280.8	------	1.28(6)
284.8	------	1.07(6)
285.8	0.17(2)	0.24(2)
286.8	0.13(8)	0.46(3)
287.1	0.03(3)	0.30(3)
287.3	0.08(3)	0.10(1)
289.0	0.32(3)	0.42(4)
293.0	0.12(5)	0.25(5)
294.9	0.30(5)	0.45(5)
296.0	0.37(5)	0.53(5)
296.7	0.24(3)	0.59(4)
296.8	0.37(4)	0.54(6)
298.0	0.09(4)	0.24(4)
300.0	0.08(3)	0.42(3)
300.9	0.12(3)	0.35(3)
301.8	0.13(3)	0.30(3)
302.0	0.18(3)	0.37(3)
302.9	0.10(3)	0.24(3)
303.8	0.14(2)	0.35(2)
305.0	0.10(3)	0.38(3)
305.8	0.10(2)	0.28(3)
307.0	0.16(2)	0.28(3)
309.0	0.00(2)	0.27(2)
310.0	0.06(2)	0.31(3)
311.0	0.11(3)	0.30(3)
313.0	0.08(3)	0.31(3)
315.0	-0.09(2)	0.32(3)

[a] Errors in the last digit are given parenthetically.

Table II. CO_2 C(KVV) Auger asymmetry parameter.

hν(eV)	$\beta_A(h\nu)$	$\beta_T(h\nu)$
270.0	---	1.40(1)
273.0	---	1.53(1)
279.7	---	1.28(1)
282.7	---	1.33(1)
284.7	---	1.42(1)
286.7	---	1.42(1)
287.7	---	0.99(1)
289.2	0.27(2)	---
290.0	0.21(2)	---
291.7	0.35(3)	0.45(3)
295.7	0.77(4)	0.84(4)
299.7	0.50(4)	0.68(4)
301.7	0.20(2)	0.58(3)
302.7	0.17(2)	0.55(5)
303.7	0.16(1)	0.48(3)
305.7	0.25(1)	0.56(3)
306.7	0.15(1)	0.45(3)
308.7	0.05(1)	0.30(3)
309.7	0.12(1)	0.37(2)
311.7	0.12(1)	0.27(2)
313.2	0.10(1)	0.31(2)
314.7	0.17(2)	0.39(3)
316.7	0.15(1)	0.35(3)
318.7	0.15(1)	0.36(3)
320.7	0.07(1)	0.42(3)
322.7	0.07(1)	0.38(3)
324.7	0.05(1)	0.33(3)
330.7	0.13(1)	0.41(4)
335.7	0.36(4)	0.30(4)
340.7	0.37(3)	---

Table III. Total O1s shake-up intensity relative to the O1s main line of CO_2.

hν(eV)	branching ratio(percent)
593.0	17.1 ± 1.9
609.0	20.4 ± 2.6
615.0	23.9 ± 3.1
625.0	21.1 ± 2.4
631.0	21.9 ± 2.6

(The average value for these results is 20.8 ± 2.7 percent).

Table IV. OCS S(LVV) Auger asymmetry parameter β_A.

$h\nu$(eV)	$\beta_A(h\nu)$	$\beta_T(h\nu)$
160.0	1.13(7)	1.00(7)
164.0	0.41(4)	0.85(5)
165.5	0.14(3)	0.58(4)
166.5	0.08(3)	0.61(4)
167.0	0.18(3)	0.66(4)
168.0	0.15(3)	0.67(4)
170.0	0.06(3)	0.62(4)
172.0	0.01(2)	0.43(3)
174.0	0.00(2)	0.37(2)
176.0	-0.05(1)	0.30(2)
177.0	-0.06(1)	0.31(2)
178.0	-0.07(2)	0.33(2)
178.5	-0.05(2)	0.33(2)
179.0	-0.07(2)	0.33(2)
179.5	-0.02(2)	0.37(2)
180.0	-0.13(1)	0.30(2)
182.0	-0.08(2)	0.38(2)
185.0	-0.19(2)	0.35(3)
187.0	-0.23(2)	0.36(3)
190.0	-0.16(1)	0.38(2)

Table V. The Coulomb phase shift difference $\Delta(\varepsilon)$, where the non-Coulomb phase difference (-2π) has been suppressed, the S2p asymmetry parameter $\beta(\varepsilon)$ of OCS, and the ratio of the two radial matrix elements $\rho(\varepsilon)$ calculated with constant non-Coulomb phase shifts (*) and atomic non-Coulomb phase shifts calculated by Manson (**).[42]

$h\nu$(eV)	$\Delta(\varepsilon)$[a]	$\beta(\varepsilon)$[b]	$\rho(\varepsilon)^*$	$\rho(\varepsilon)^{**}$
174.0	-0.26	0.27(4)	0.51(3)	0.36(2)
175.0	-0.23	0.27(3)	0.46(2)	0.37(2)
176.0	-0.20	0.25(3)	0.45(2)	0.40(2)
177.0	-0.19	0.29(3)	0.41(2)	0.41(2)
178.0	-0.18	0.13(3)	0.50(2)	0.60(2)
178.5	-0.17	0.14(3)	0.49(2)	0.62(3)
179.0	-0.16	0.07(3)	0.53(2)	0.75(3)
179.5	-0.16	0.05(3)	0.54(2)	0.85(3)
180.0	-0.15	0.12(3)	0.49(2)	0.86(4)
182.0	-0.14	0.11(3)	0.48(2)	1.34(11)
185.0	-0.13	0.13(3)	0.46(2)	2.42(11)
187.0	-0.12	0.01(3)	0.53(2)	11.23(42)
190.0	-0.10	0.03(3)	0.51(2)	13.27(52)

[a] The Coulomb phase shift is given in units of π.

[b] The errors are given to the last digit parenthetically.

Figure Captions

Figure 1. Electron time-of-flight spectrum from CO, after conversion to a kinetic energy scale. The sample was irradiated with photons of $h\nu$ = 305.8 eV energy (first-order), with some 2nd and 3rd-order radiation also present. Auger peaks are labelled B-1, etc., following the notation of Moddeman et al. For this spectrum the electrons were retarded by 150 volts over 60 percent of their 28 cm flight path.

Figure 2. Electron time-of-flight spectrum similar to Fig. 1, but with $h\nu$ = 315 eV and a retarding voltage of only 5 volts, allowing the C1s and O1s(2nd-order) peaks to be recorded.

Figure 3. The C(KVV) Auger results. Top panel: open circles show the total Auger intensity scaled to the results of Tronc et al.[5] The π resonance at $h\nu$ = 287.3 eV is striking. Filled circles show the region above $h\nu$ = 290 eV, times 16. The dashed curve represents the electron-ion coincidence measurements of Kay et al.,[11] times 16. The σ resonance, peaking at 306 eV, is evident, as is precursor structure below the 295.9 eV threshold. Bottom panel: filled circles show our asymmetry results. Curve shows the orientation parameter β_m calculated by Dill et al.[2]

Figure 4. The C(KVV) Auger spectra, taken at the π resonance ($h\nu$ = 287.3 eV) with a retarding potential of 100 volts, and at $h\nu$ = 296.8 eV, above the C1s threshold, with a 150 volt retarding potential.

Figure 5. The C1s photoelectron results. Top panel: our $\sigma(\varepsilon)$ values are represented by filled circles, while open circles show the electron-ion coincidence results of Kay et al.[11] The solid curve shows the STMT calculation of Padial et al.,[14] and the dashed curve the MSMXα calculation by Dehmer and Dill.[31] Bottom panel: filled circles show our asymmetry results. The solid and dashed curves are results from localized-hole MSMXα calculations by Dill et al.[30] and Grimm,[32] respectively.

Figure 6. The O(KVV) results for CO. Top panel: the experimental cross section (points) and the absorption results of Barrus et al.[3] (solid curve). Bottom panel: the experimental asymmetry parameter (points) and the β_m curve given by Dill et al.[2]

Figure 7. The O1s results for CO. Top panel: cross section results. Filled circles are our data, open circles represent the absorption results of Barrus et al.,[3] and the solid curve represents the STMT calculation of Padial et al.[14] Bottom panel: asymmetry data (points), compared with localized-hole MSMXα calculations by Grimm[32] (solid curve) and by Dill et al.[30] (dashed curve).

Figure 8. TOF spectrum of CO expanded around the O1s peak. Shake-up structure is evident. The peak labelled "S" is 13 percent as intense as the main peak.

Figure 9. Time-of-flight spectrum of CO_2, after conversion to a linear energy scale. A retarding voltage of 5 V was used in collecting this spectrum, but kinetic energies shown were corrected.

Figure 10. The C(KVV) Auger results for CO_2. Top panel: our results (filled circles) and electron energy loss results of Wight and Brion,[8] to which our data were normalized at 315 eV. Bottom panel: asymmetry values. Note that some of the asymmetry points fall at energies for which there is very little spectral intensity (cf top panel) and are therefore very questionable.

Figure 11. The C1s results for CO_2. Top panel: the cross section. Filled circles are present results, open circles the electron energy loss results of Wight and Brion.[8] The dashed curve is the STMT prediction by Padial et al.,[15] and the solid curve represents the HF static exchange prediction by Lucchese and McKoy.[16] Bottom panel: the asymmetry parameter. Filled circles are present results, the solid curve is the HF calculation of Lucchese and McKoy,[16] the dotted curve is the localized-hole MSM calculation by Grimm,[32] and the dashed curve is the unlocalized-hole MSMXα calculation of Grimm et al.[32]

Figure 12. Results for the O(KVV) peak in CO_2. Top panel: cross sections. Filled circles are present results; open circles are photoabsorption results of Barrus et al.[3] The dashed

curve and full curve display the theoretical predictions by Padial et al.[15] and by Lucchese and McKoy,[16] respectively. Bottom panel: the asymmetry parameter. Filled circles are the present results, connected by a line to guide the eye.

Figure 13. The asymmetry parameter for the O1s peak in CO_2. The present results are shown as points. The solid and dashed curves represent predictions from localized-hole MSMXα calculations by Grimm[32] and Dill, et al.,[30] respectively.

Figure 14. The O1s peaks of CO_2 on an expanded scale, to show shake-up structure.

Figure 15. The TOF electron spectrum from CF_4 excited at a nominal photon energy of 318.8 eV. The peaks are (left to right): C1s, C(KVV) plus inner valence states, $4a_1 + 3t_2$, $1e + 4t_2 + 1t_1$, C1s(second-order), and F(KVV)(third-order).

Figure 16. The CF_4 C(KVV) results, shown as filled circles. Top panel: the cross section curve of Bachrach et al.,[14] corrected for valence-electron contributions to the photoabsorption cross section, is shown as a curve. Our data were normalized to this curve at 302 eV. Bottom panel: experimental asymmetry. The line through the points is shown to guide the eye.

Figure 17. The C1s photoelectron results for CF_4. Our data are shown as filled circles. Open circles in the top panel

show some of the electron energy loss results of Wight and Brion,[9] to which our data are normalized at 328 eV, and the solid curve represents photoabsorption results by Bachrach et al.[4] The curve in the lower panel is drawn through the data.

Figure 18. TOF electron spectrum of OCS excited at a photon energy of 311.0 eV. The peaks are (left to right): C1s, S2s ($6\sigma^{-1}$), S2p (with the left shoulder being the S(LVV) Auger peak), C(KVV) Auger plus valence states, and O(KVV) Auger.

Figure 19. TOF electron spectrum of OCS excited at a photon energy of 179.0 eV. Four electron pulses separated by 2.8 ns were present, which caused the S(LVV) Auger to look like four structures and the S2p to be broadened (in time).

Figure 20. Cross section and asymmetry parameter for the C(KVV) of OCS. A small portion of valence peak intensity is included in the results. The solid curve in the top panel represents the electron energy loss (and x3) results of Wight and Brion[37] and the present measurements correspond to the filled circles. The measured asymmetry parameter is shown in the bottom panel.

Figure 21. Cross section and asymmetry parameter for the C(1s) of OCS. The relative cross section is shown in the top panel. The measured asymmetry parameter, shown by the filled circles, and the localized-hole MSMXα calculation of Grimm is illustrated in the bottom panel.

Figure 22. The S(LVV) results from OCS. Our data are represented by filled circles in both panels. Open circles in the top panel are electron energy loss yield results of Wight and Brion,[37] scaled to our data. Solid curves are drawn to connect the points.

Figure 23. The S2p results from OCS. The notation is the same as in Figure 22.

Figure 24. An expanded TOF spectrum around the S2p peak region showing the two satellite peaks. Note that the satellites are more intense relative to the main peak than they appear, because of their greater data density.

Figure 25. Phase-shift differences and radial matrix element ratio for S2p in OCS, calculated from the measured asymmetry parameter according to a "quasi-atomic" model described in the text. The non-Coulomb relative phase difference equal to -2π has been suppressed to show variation of the Coulomb relative phase shift differences for the εs and εd channels.

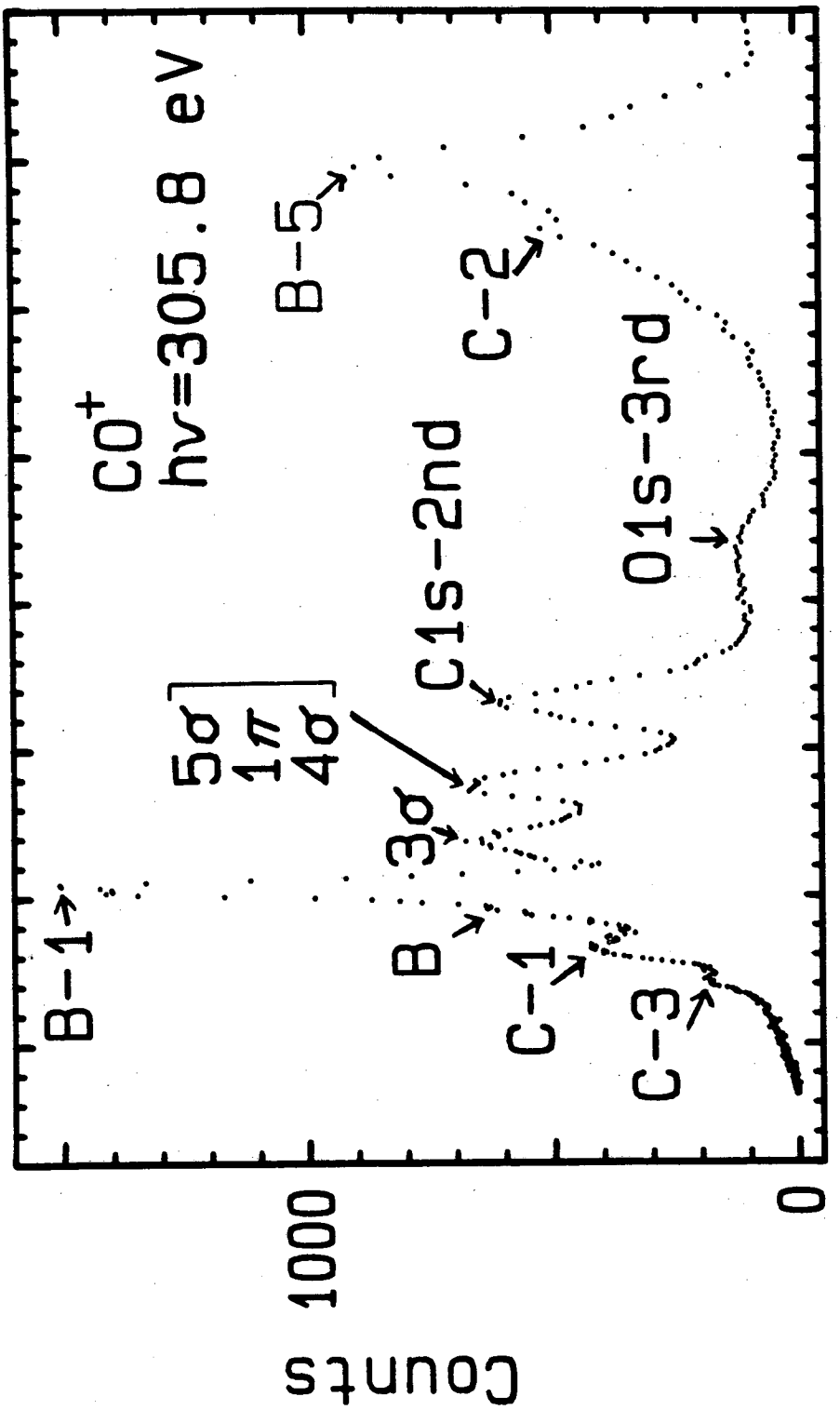

XBL 831-7879

Fig. 1

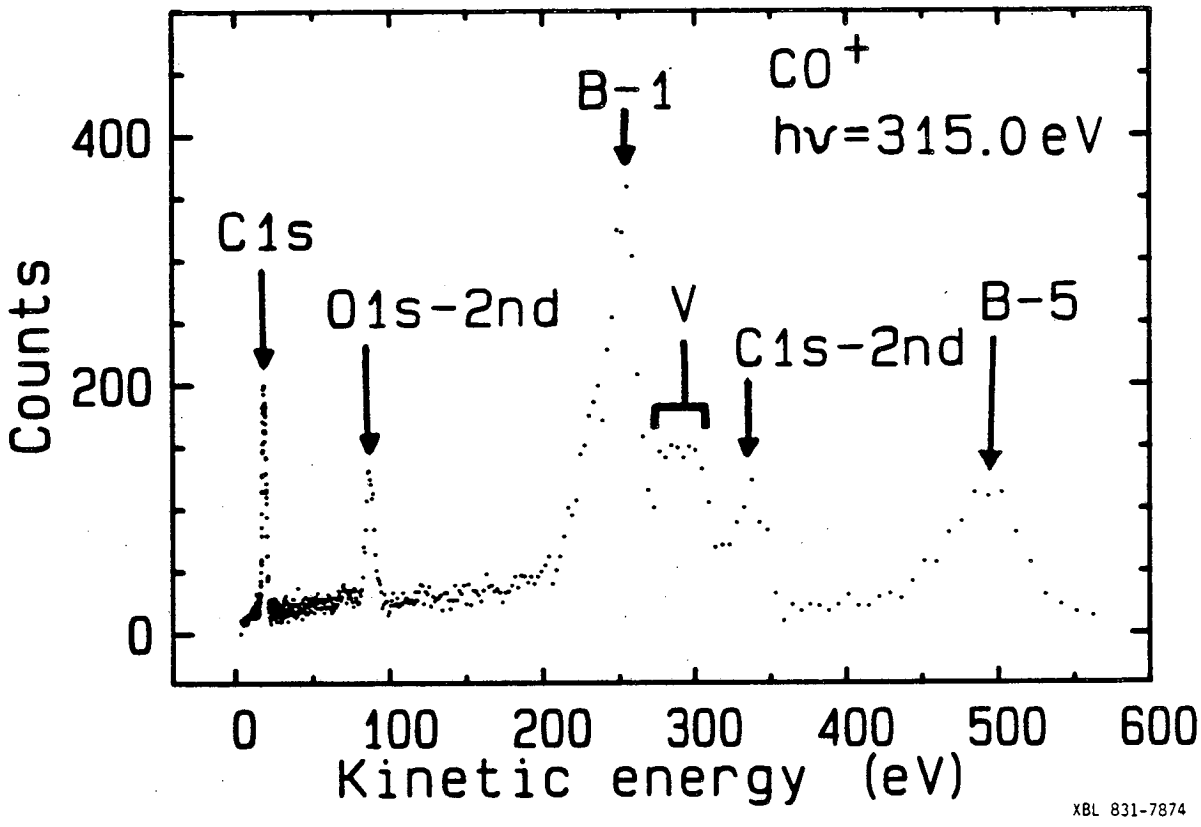
CO+
hν=315.0 eV
B-1
C1s
O1s-2nd
V
C1s-2nd
B-5
Counts
400
200
0
0
100
200
300
400
500
600
Kinetic energy (eV)
XBL 831-7874

Fig. 2

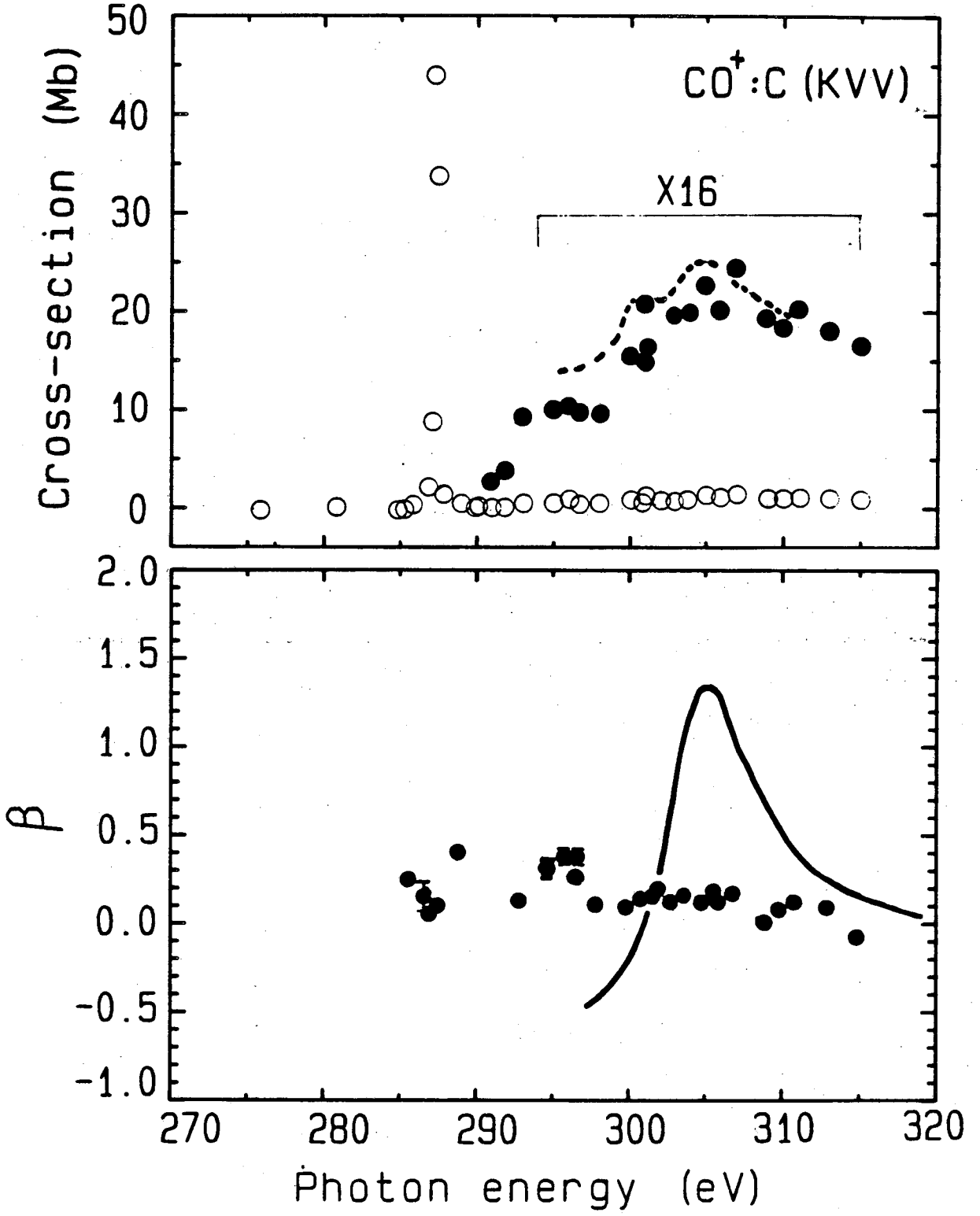

Fig. 3

XBL 8212-12256

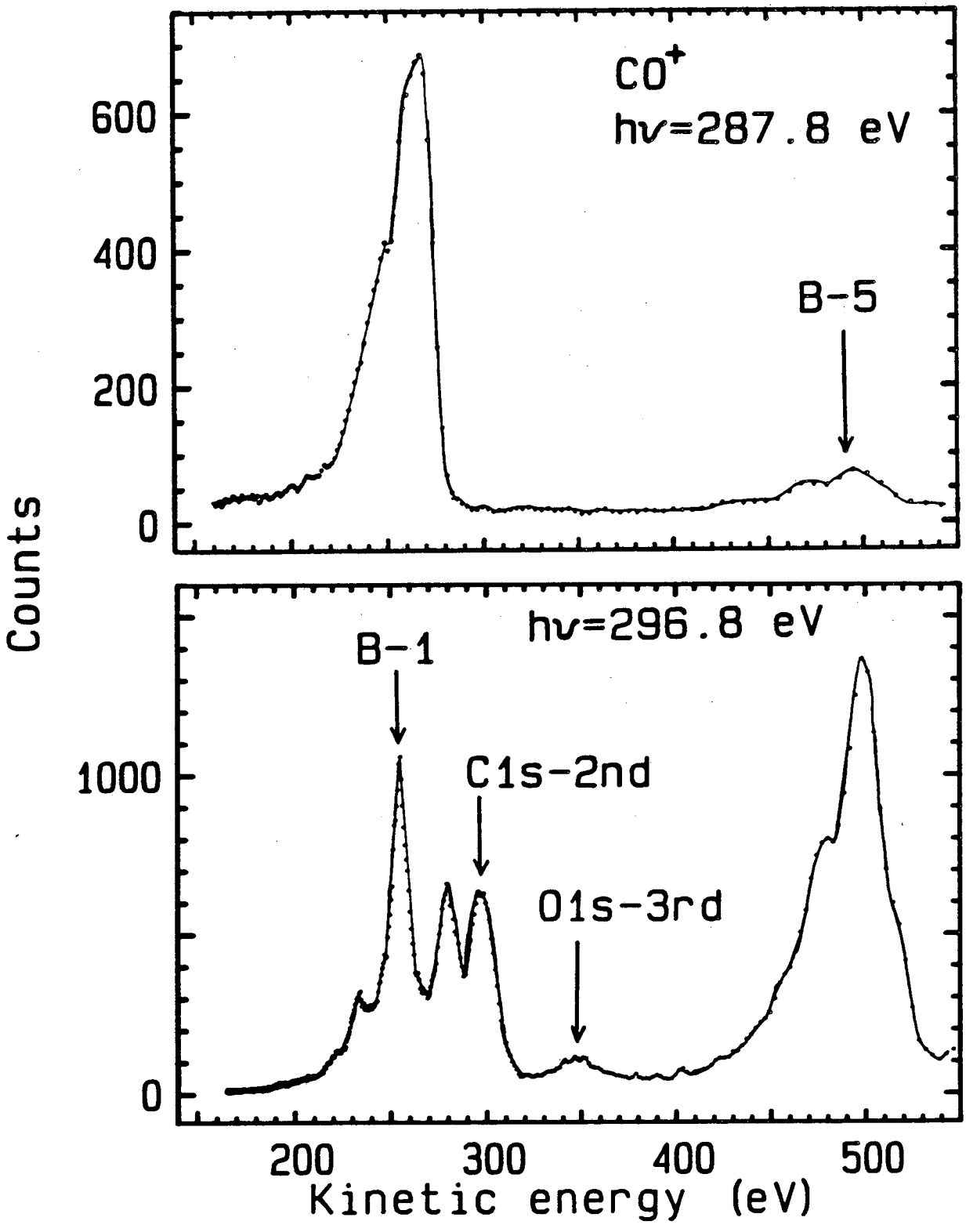

Fig. 4

XBL 832-8338

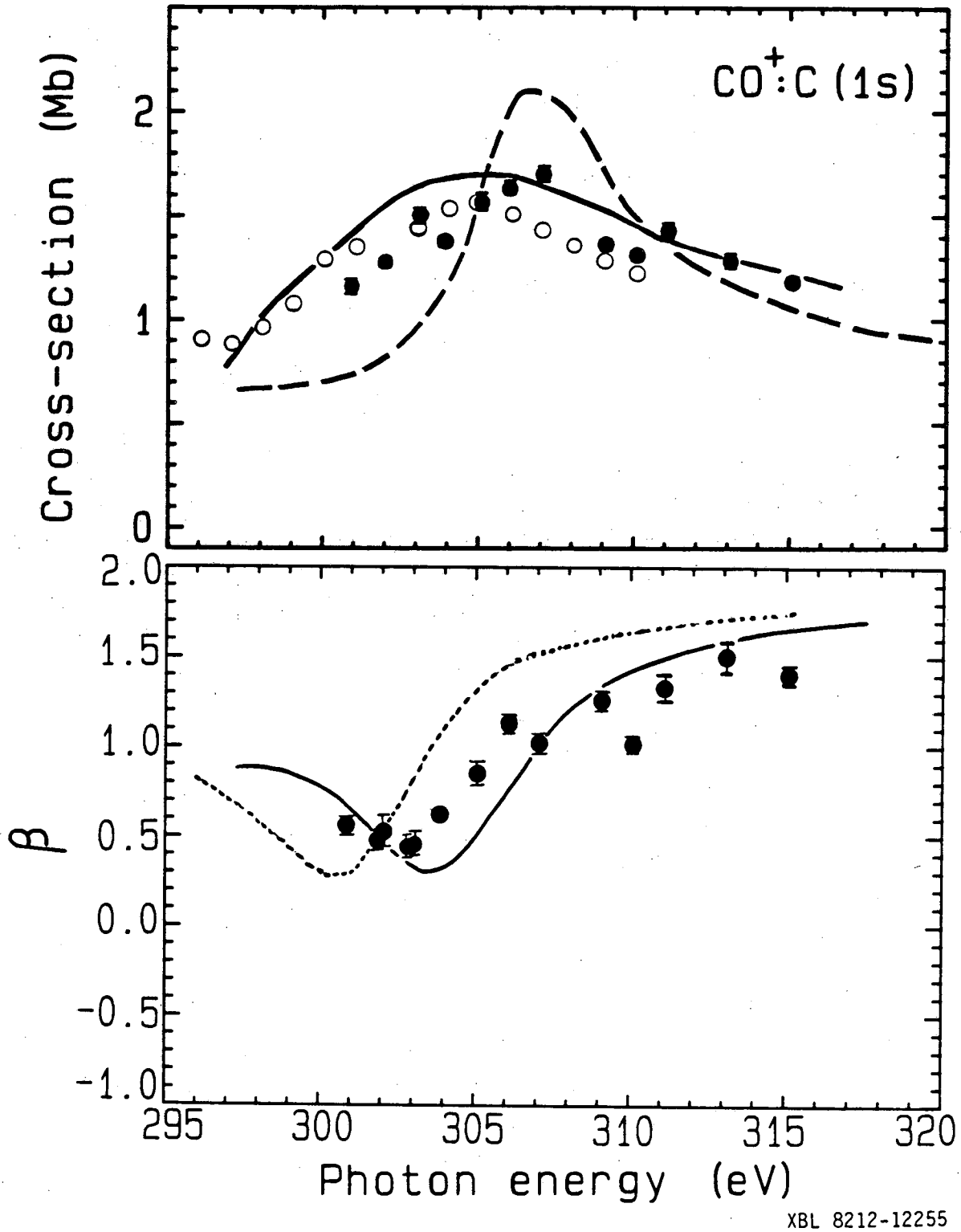

XBL 8212-12255

Fig. 5

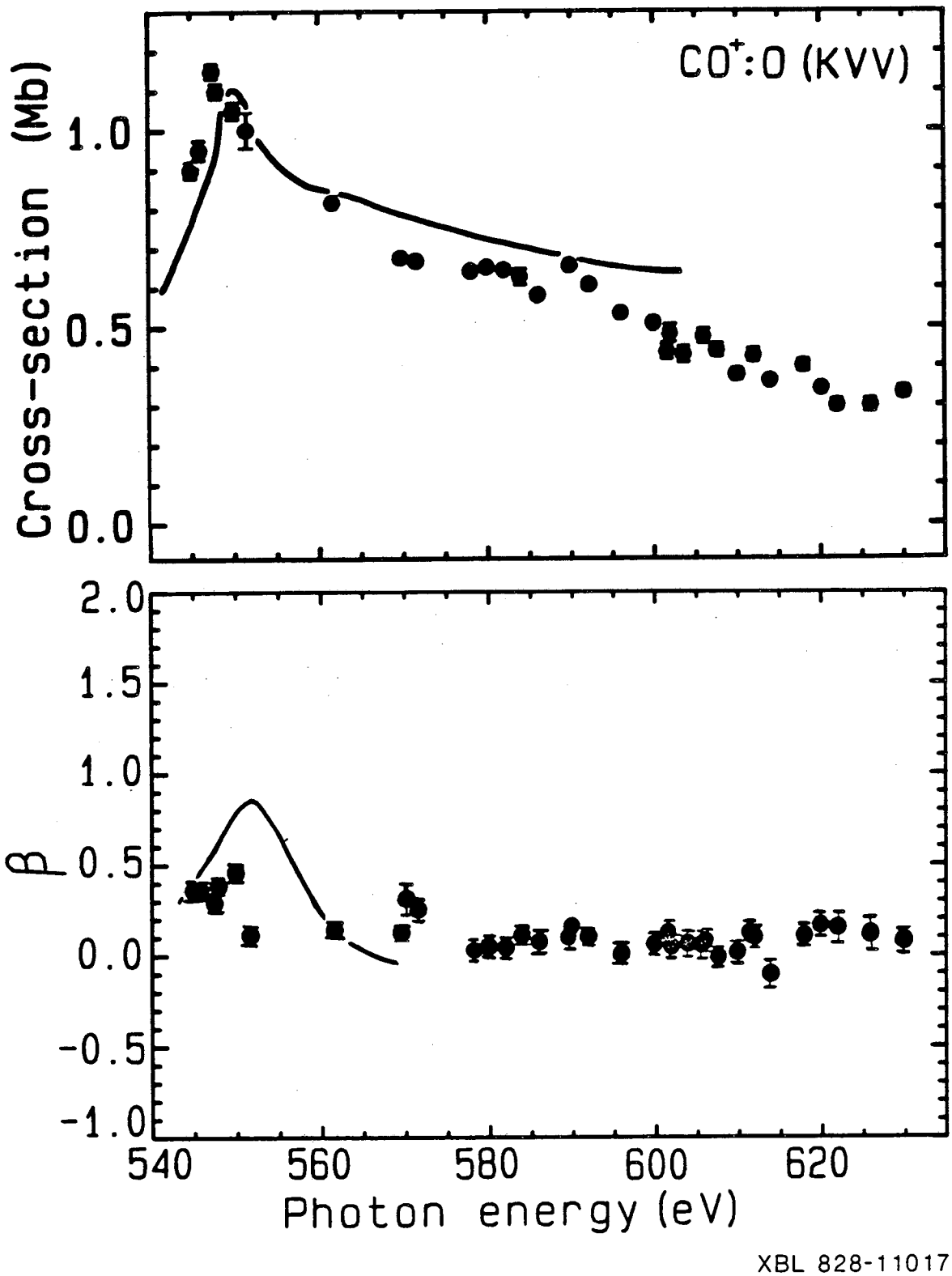

XBL 828-11017

Fig. 6

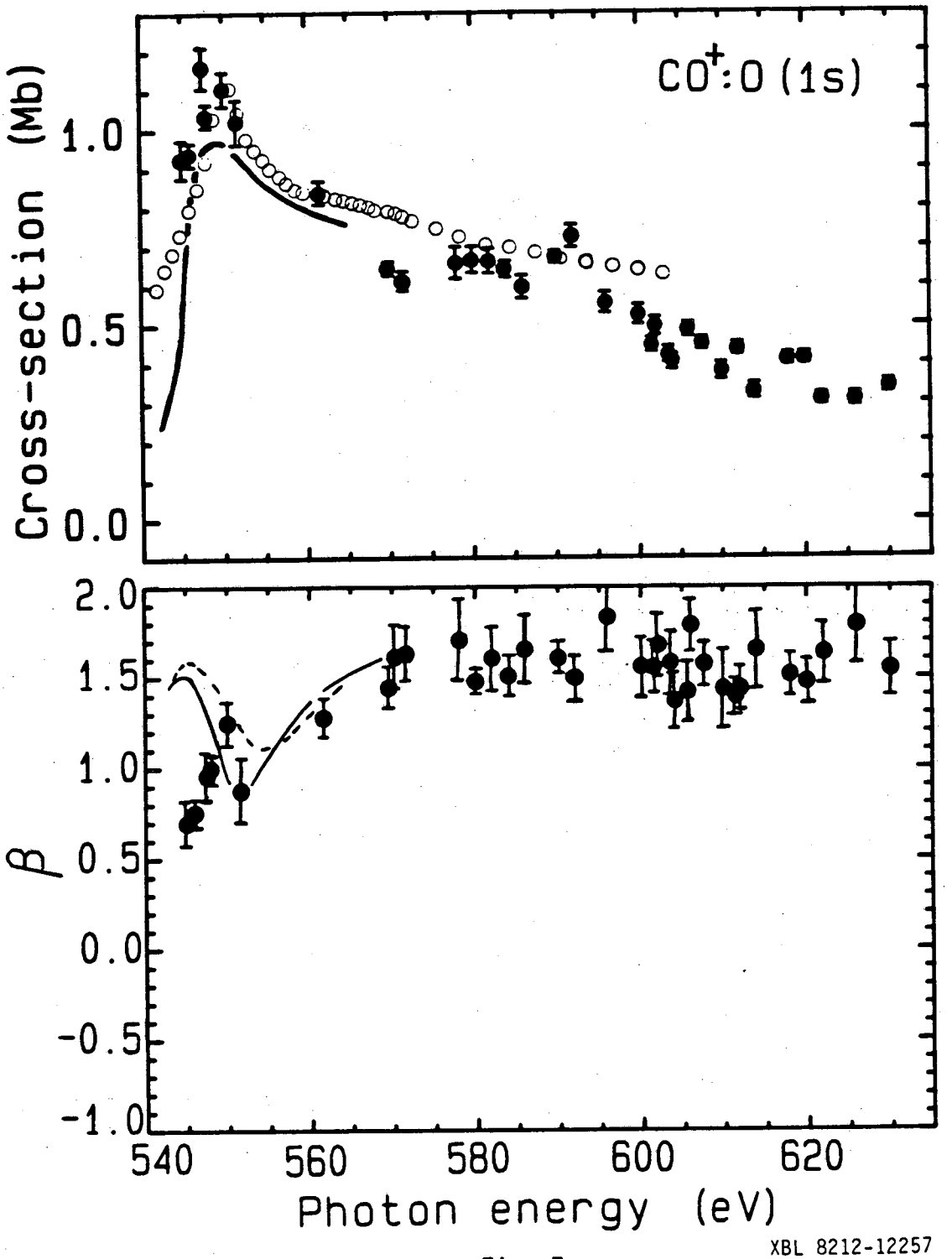
CO+:O (1s)
Cross-section (Mb)
1.0
0.5
0.0
2.0
1.5
1.0
0.5
0.0
-0.5
-1.0
β
540
560
580
600
620
Photon energy (eV)
XBL 8212-12257

Fig. 7

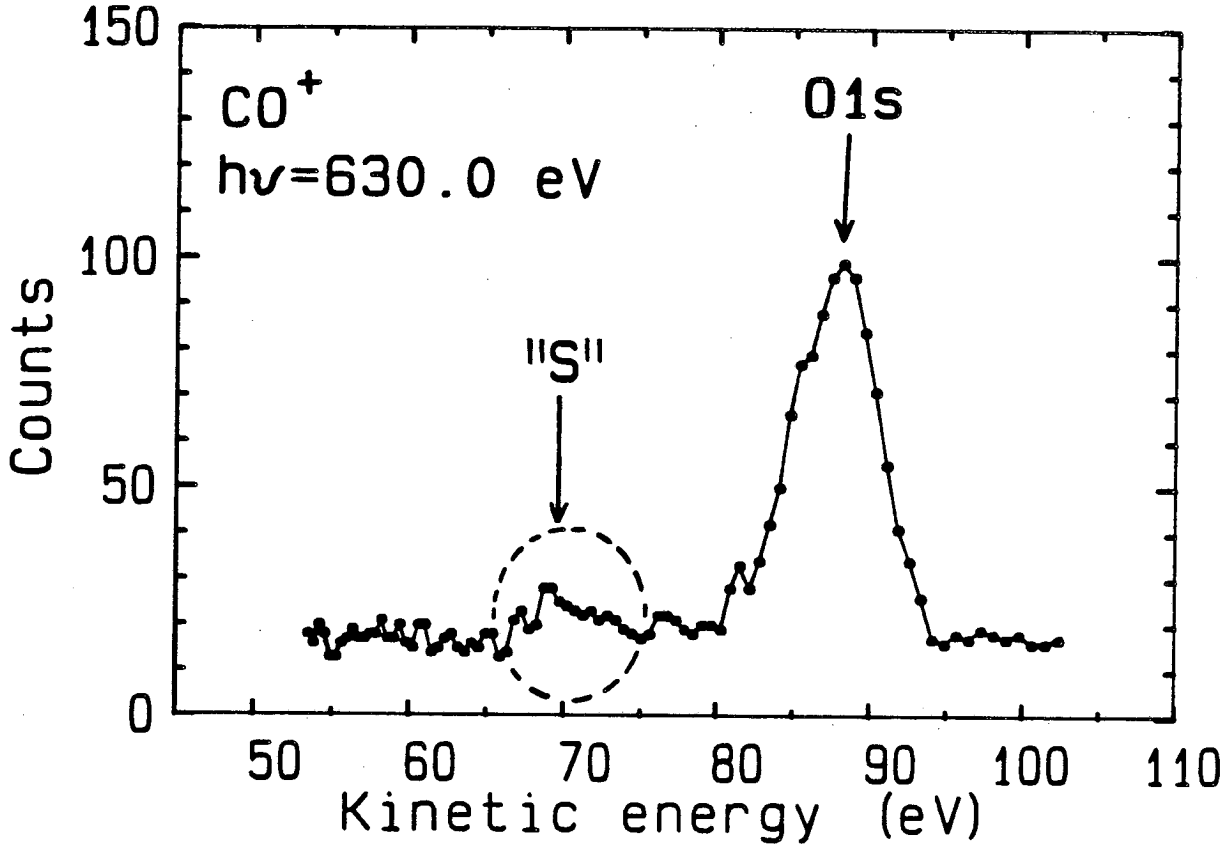

XBL 832-8333

Fig. 8

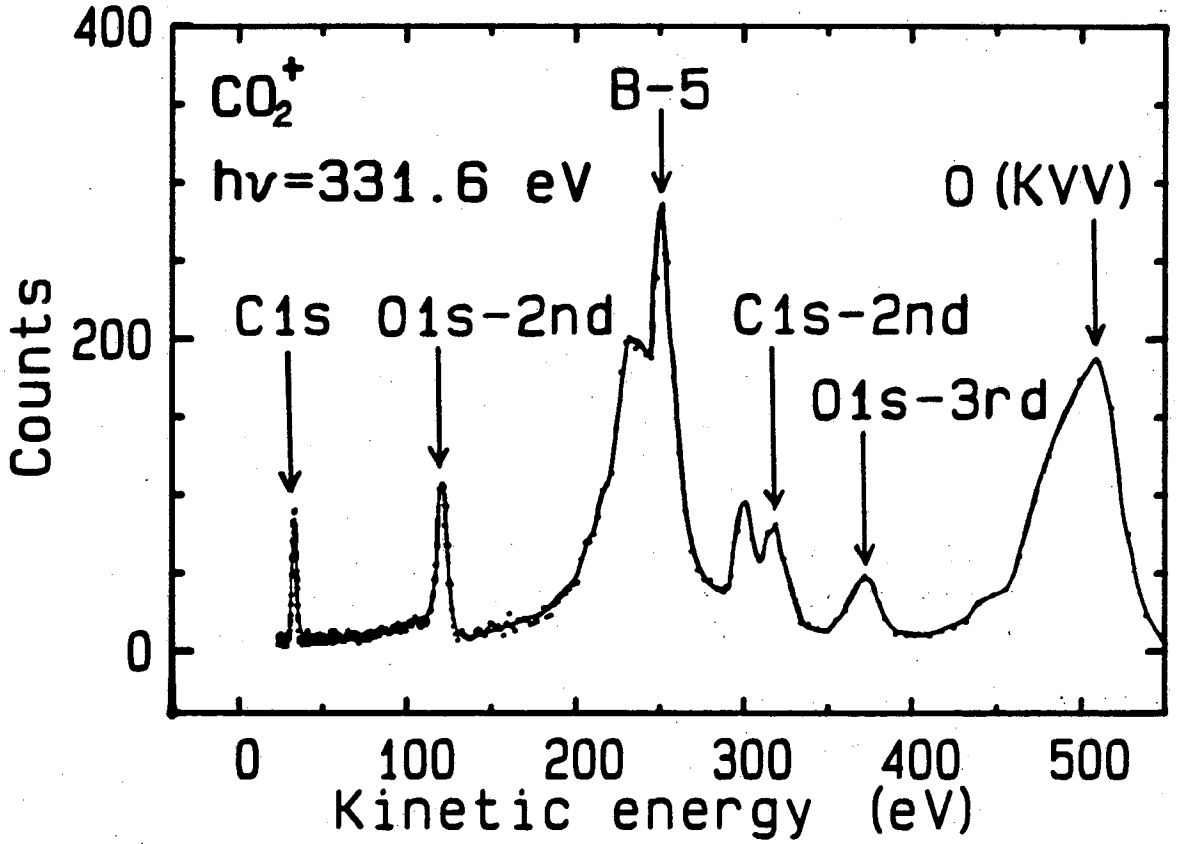

XBL 832-8337

Fig. 9

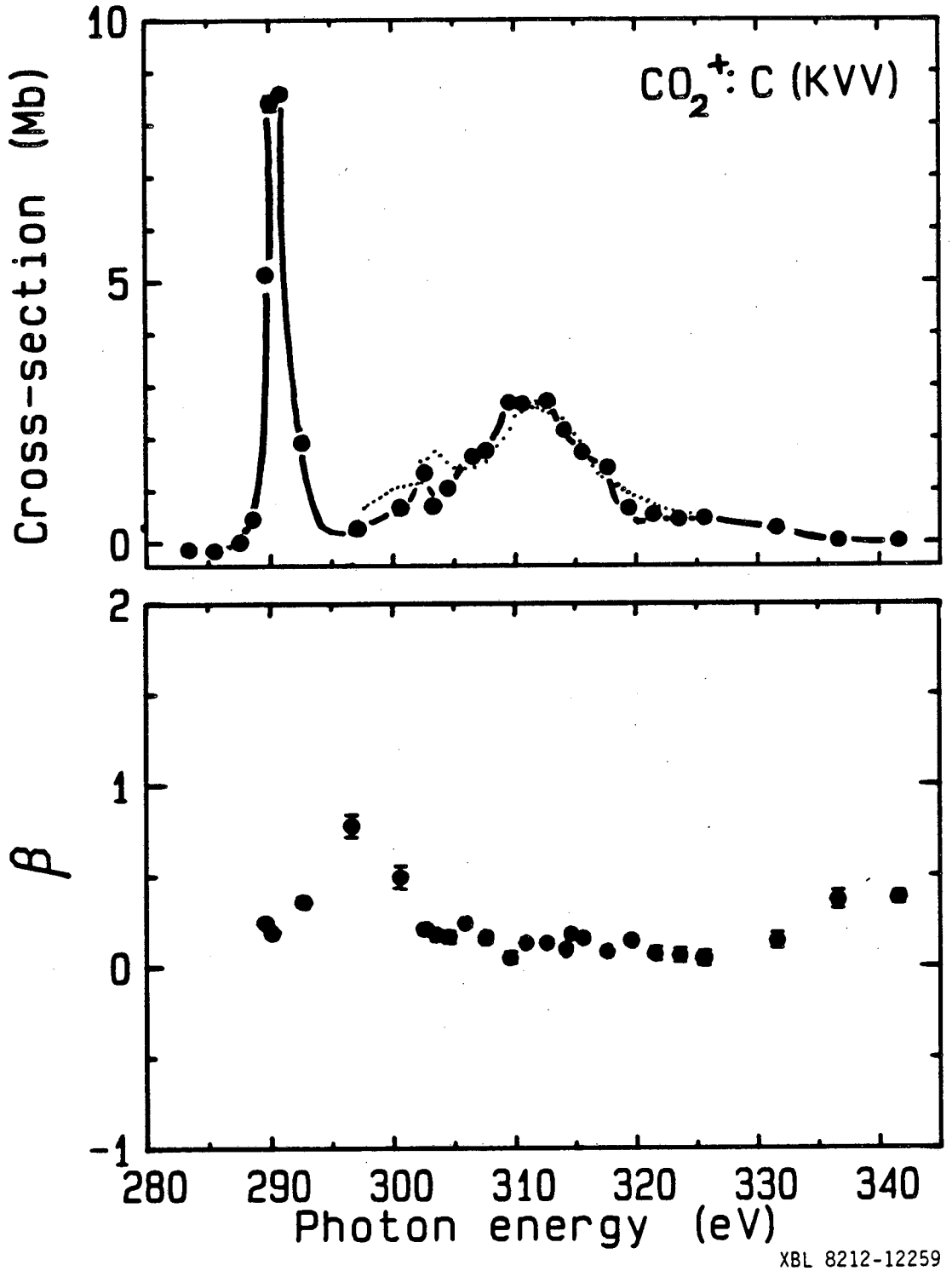
Cross-section (Mb)
10
5
0
CO_2^+: C (KVV)
β
2
1
0
-1
280
290
300
310
320
330
340
Photon energy (eV)
XBL 8212-12259

Fig. 10

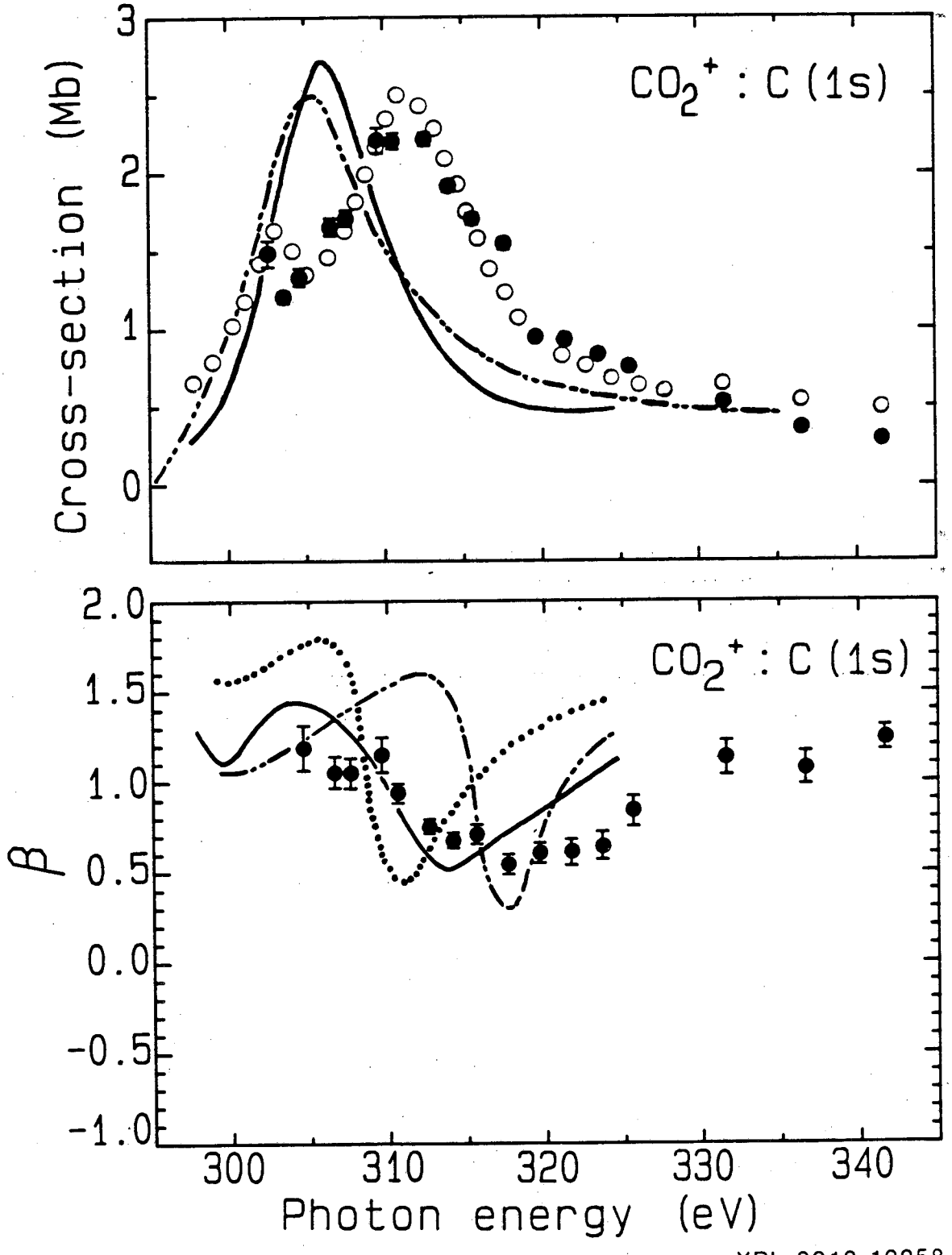

XBL 8212-12258

Fig. 11

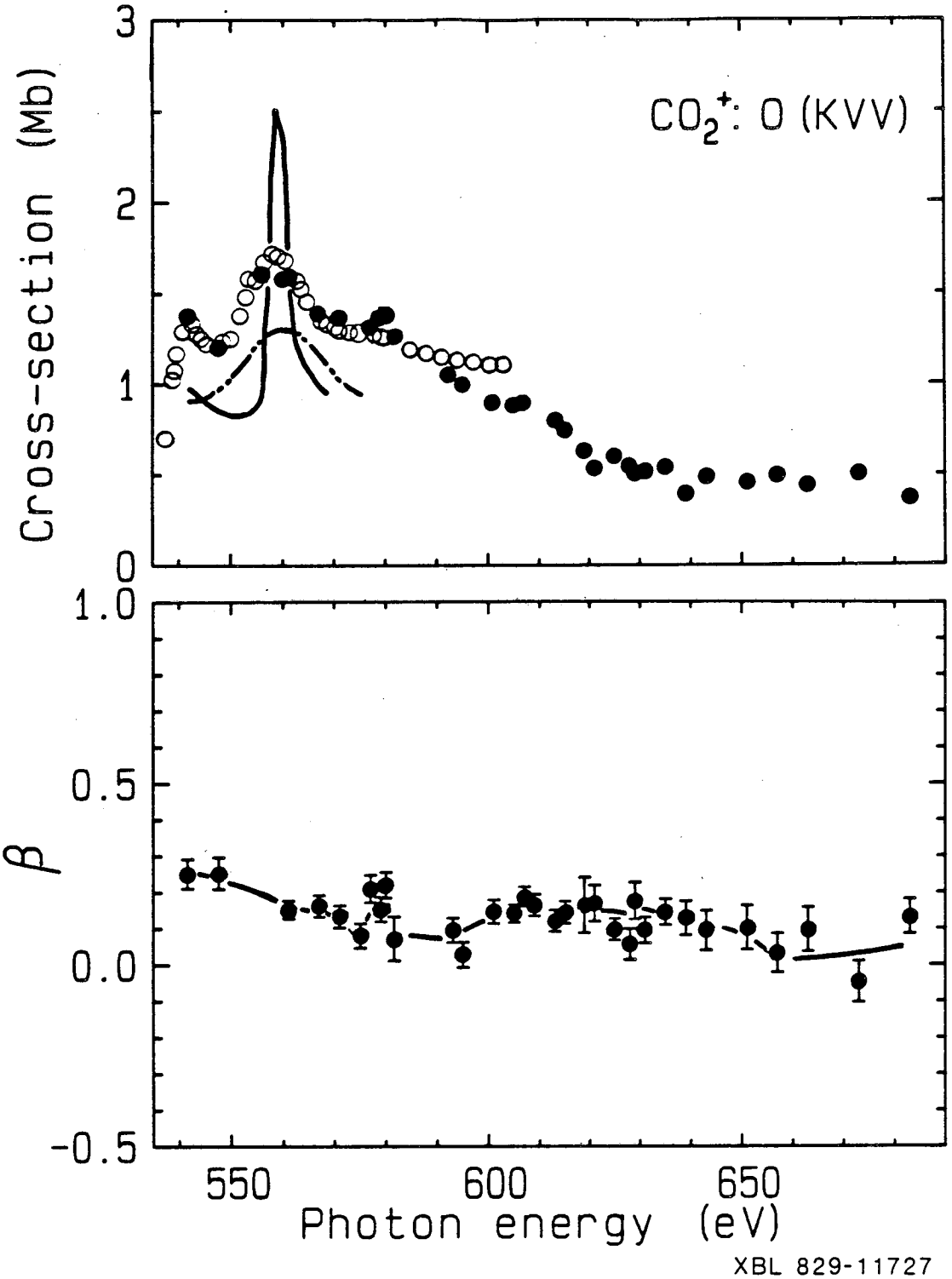
Cross-section (Mb)
3
2
1
0
CO_2^+: O (KVV)
1.0
0.5
0.0
-0.5
β
550
600
650
Photon energy (eV)
XBL 829-11727

Fig. 12

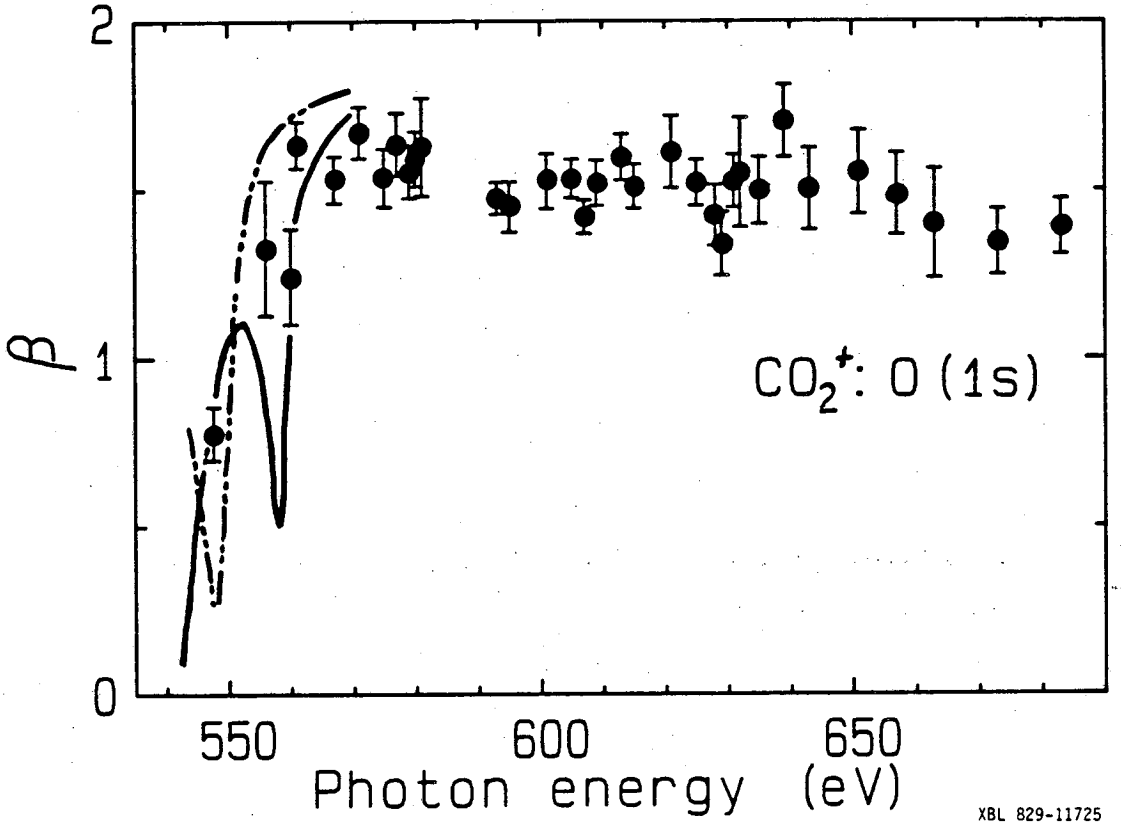

Fig. 13

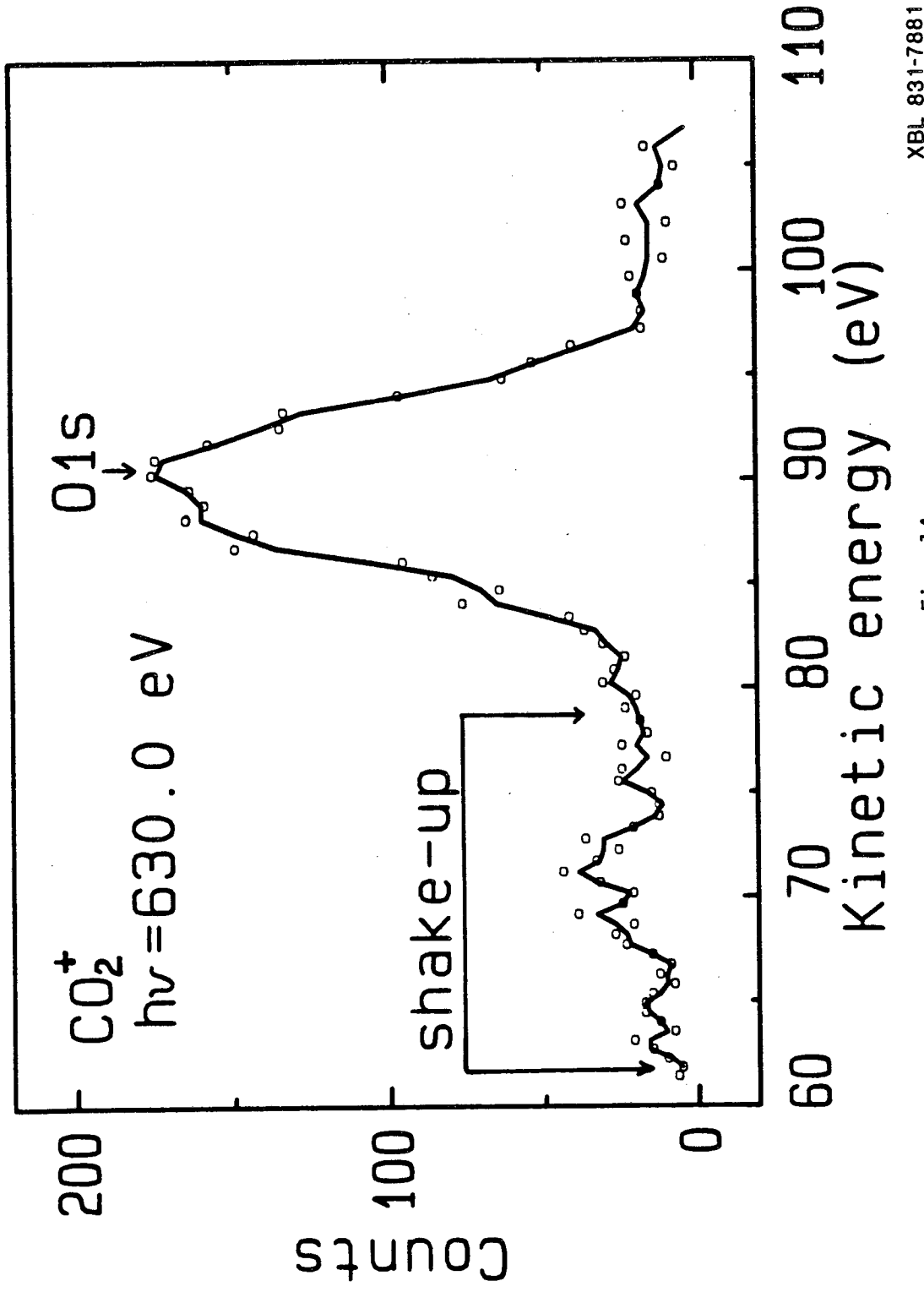

XBL 831-7881

Fig. 14

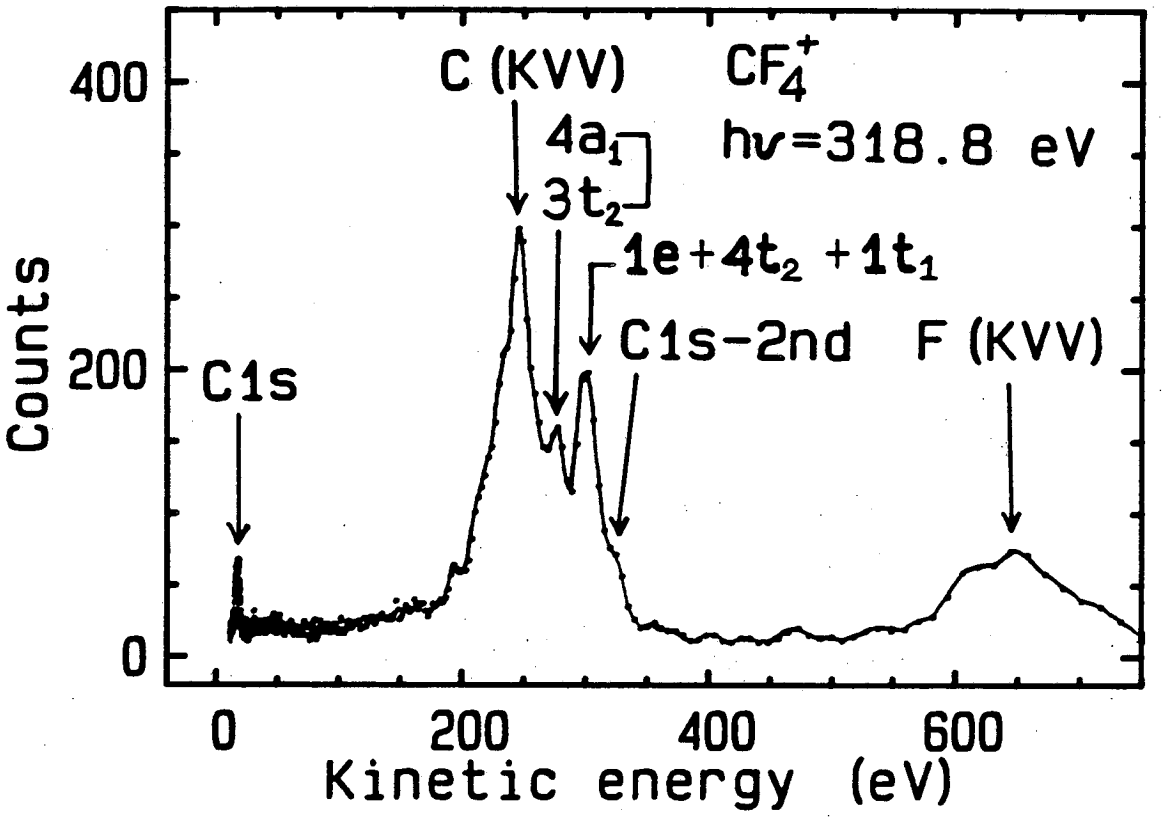

Fig. 15

XBL 832-8334

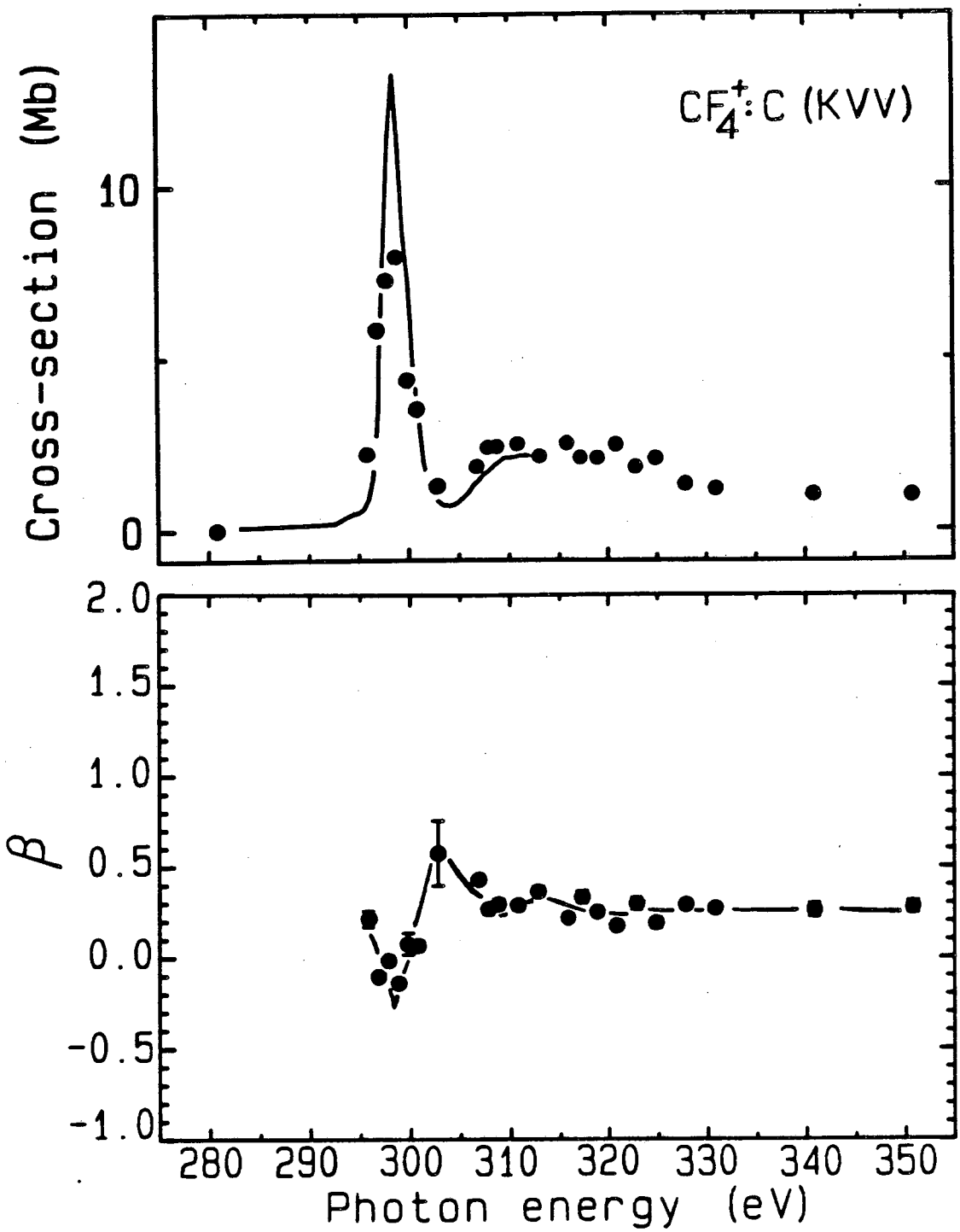

XBL 828-11143

Fig. 16

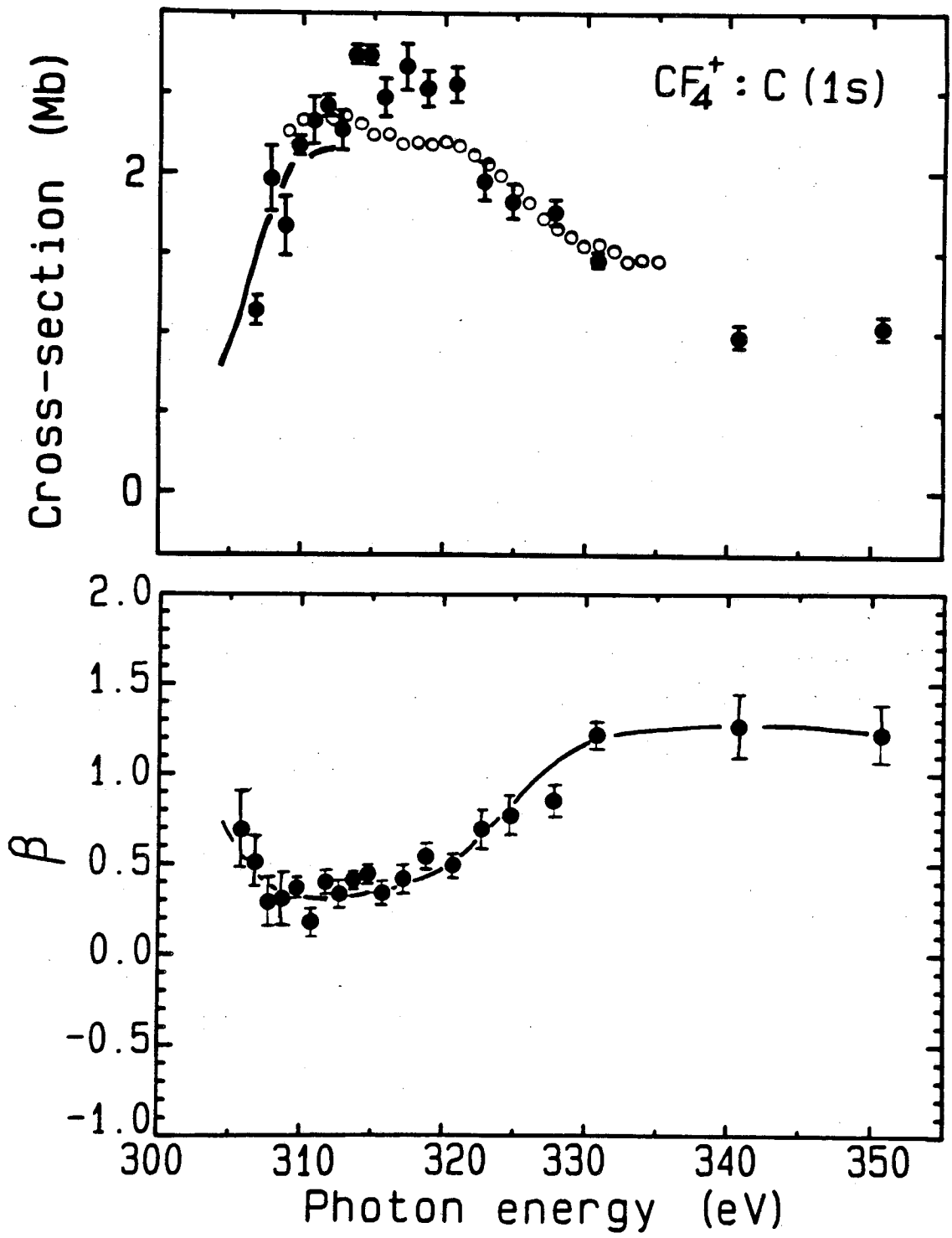

Fig. 17

XBL 828-11141

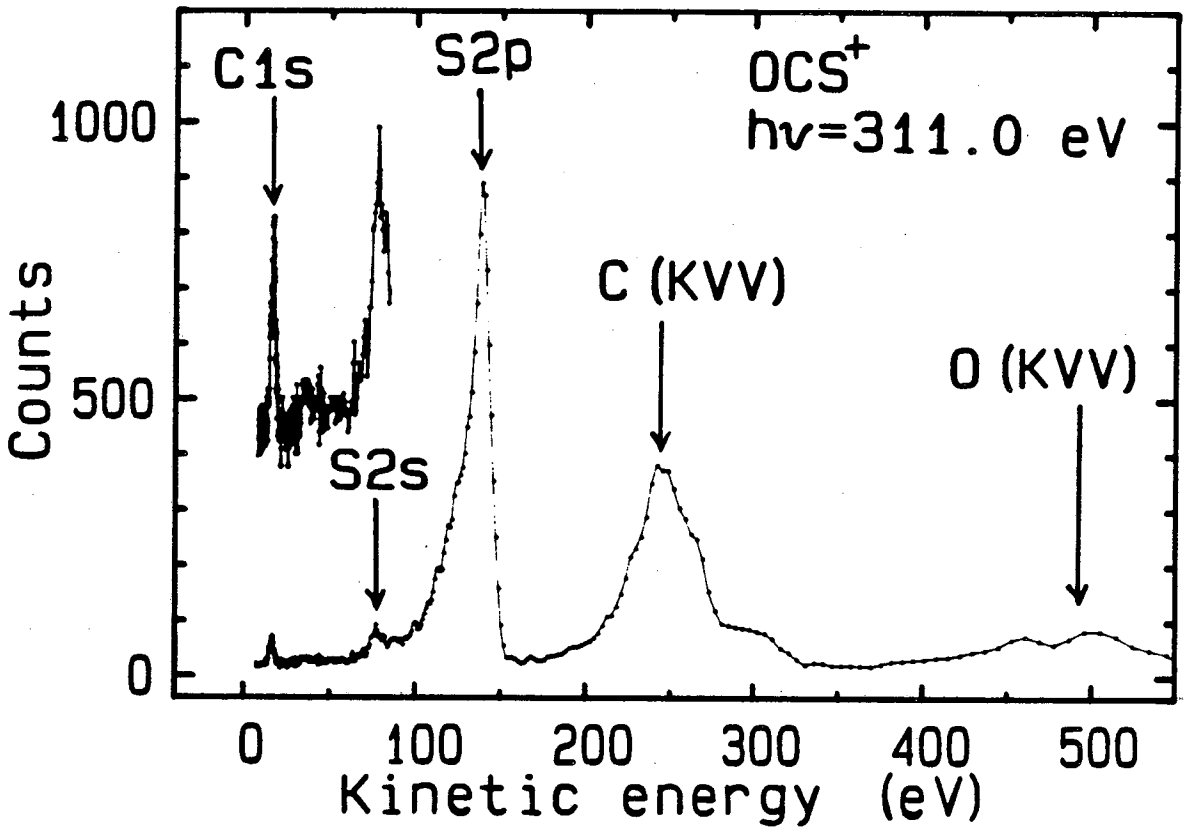

Fig. 18

XBL 832-8335

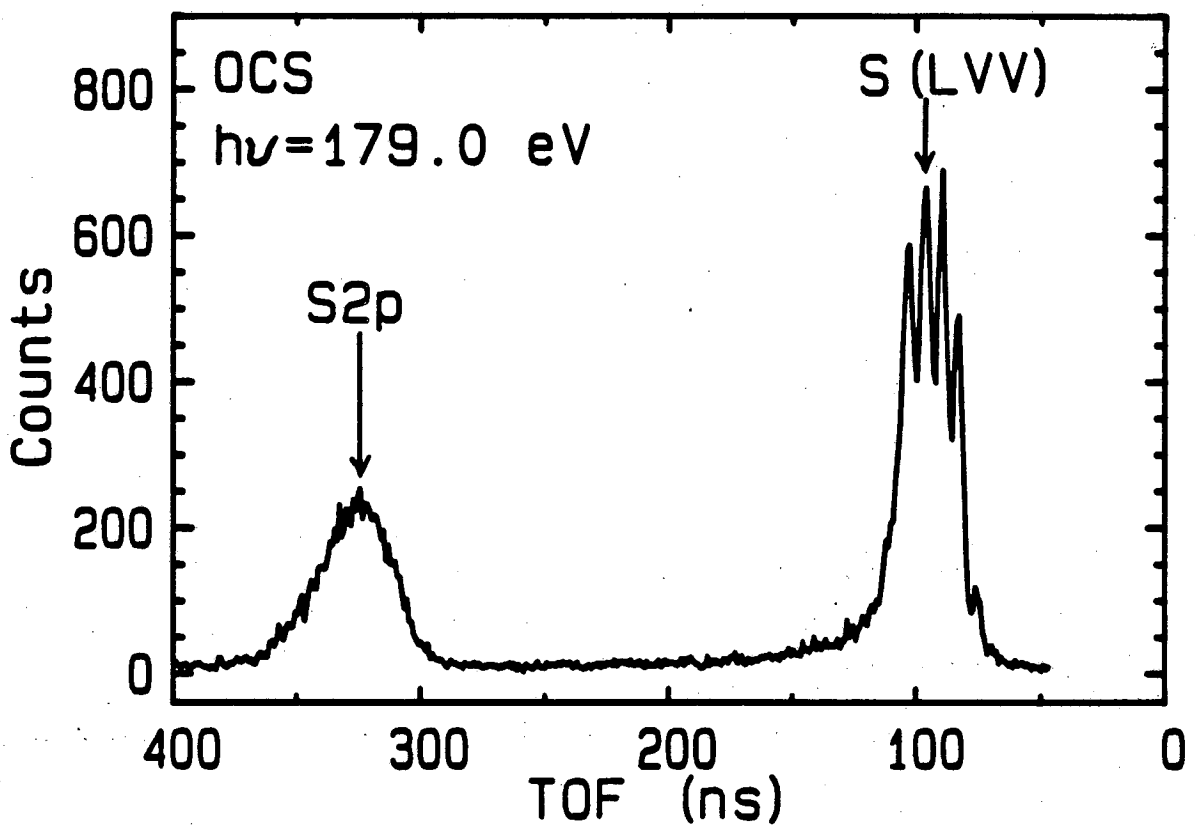

XBL 832-8336

Fig. 19

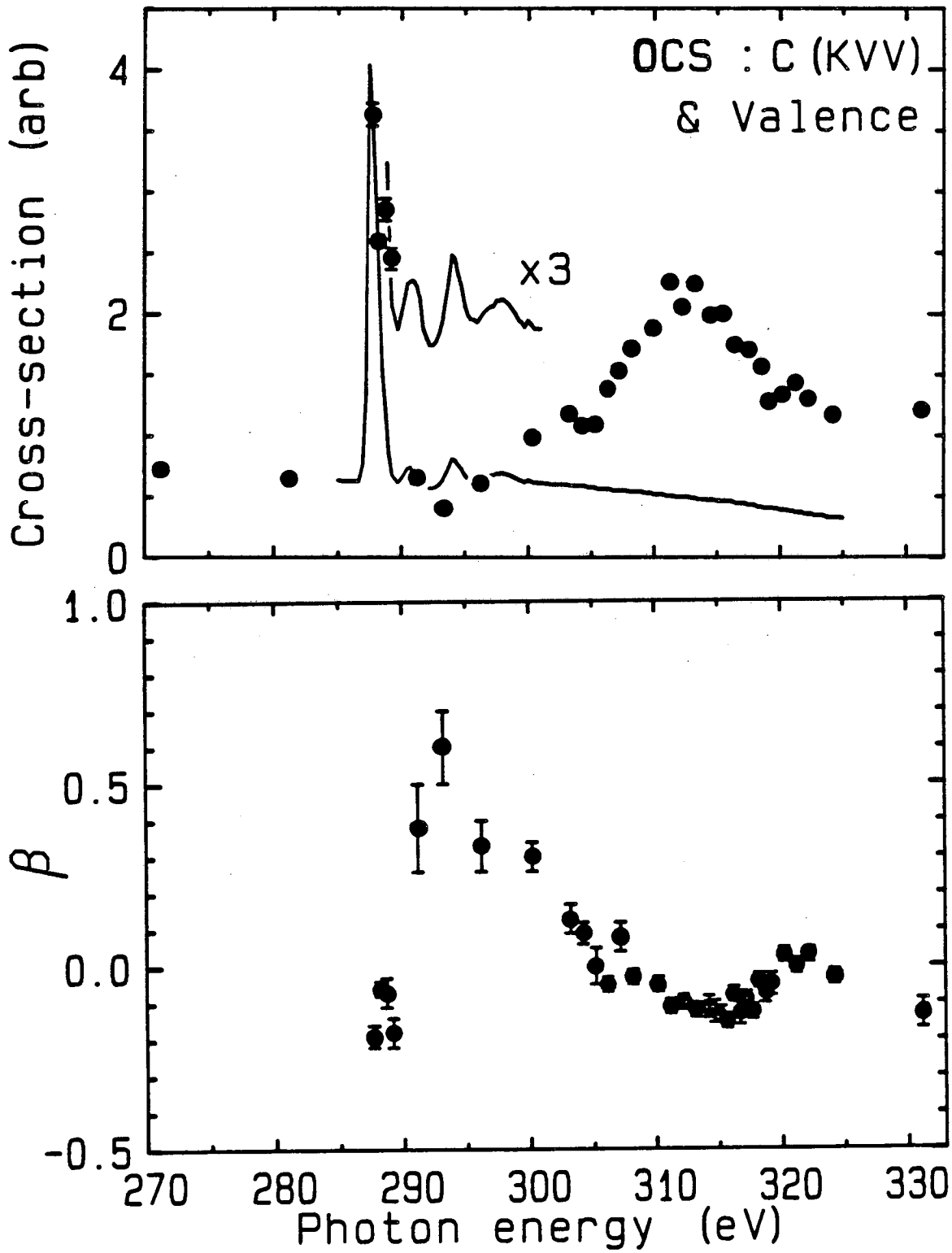

XBL 833-8921

Fig. 20

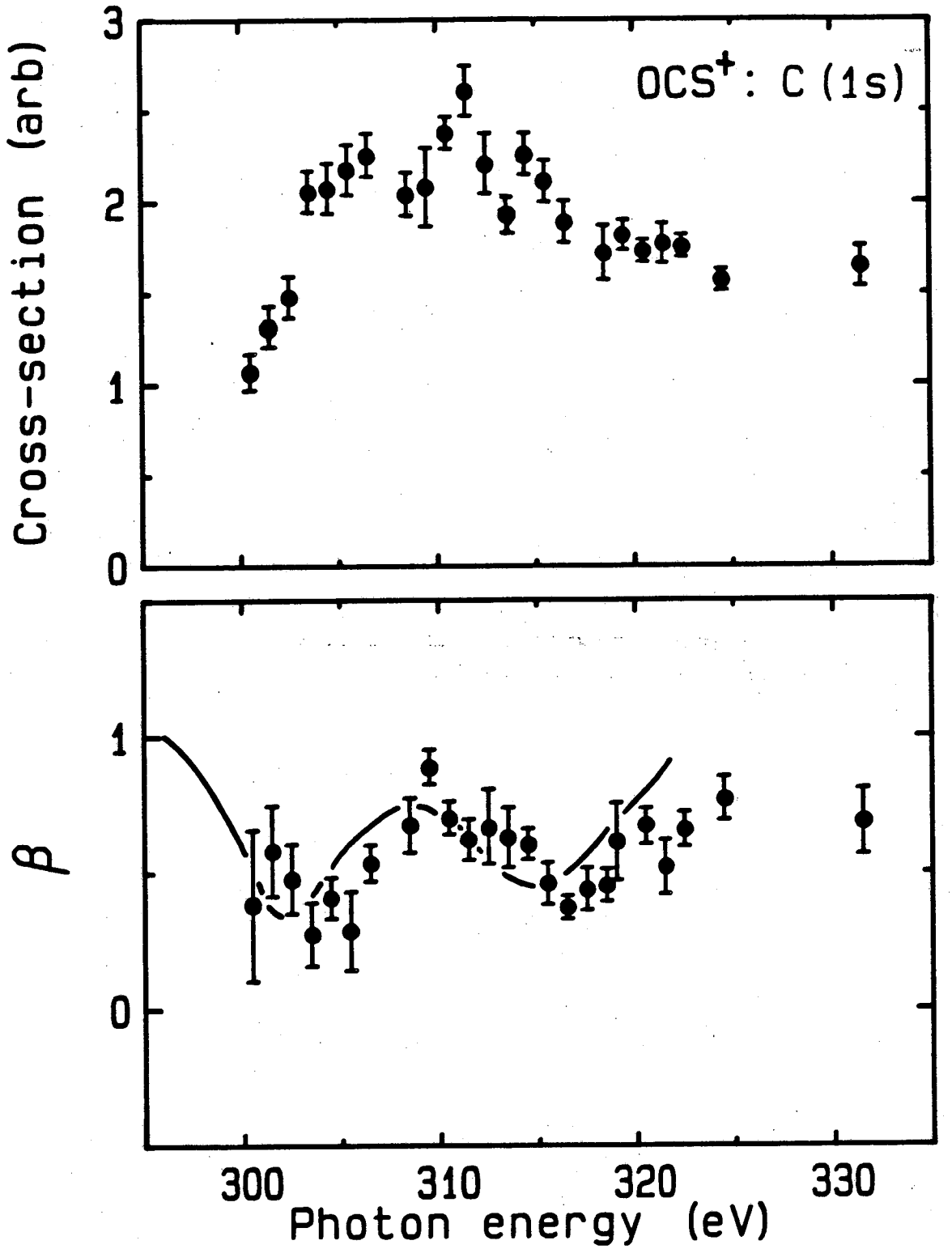

XBL 833-8920

Fig. 21

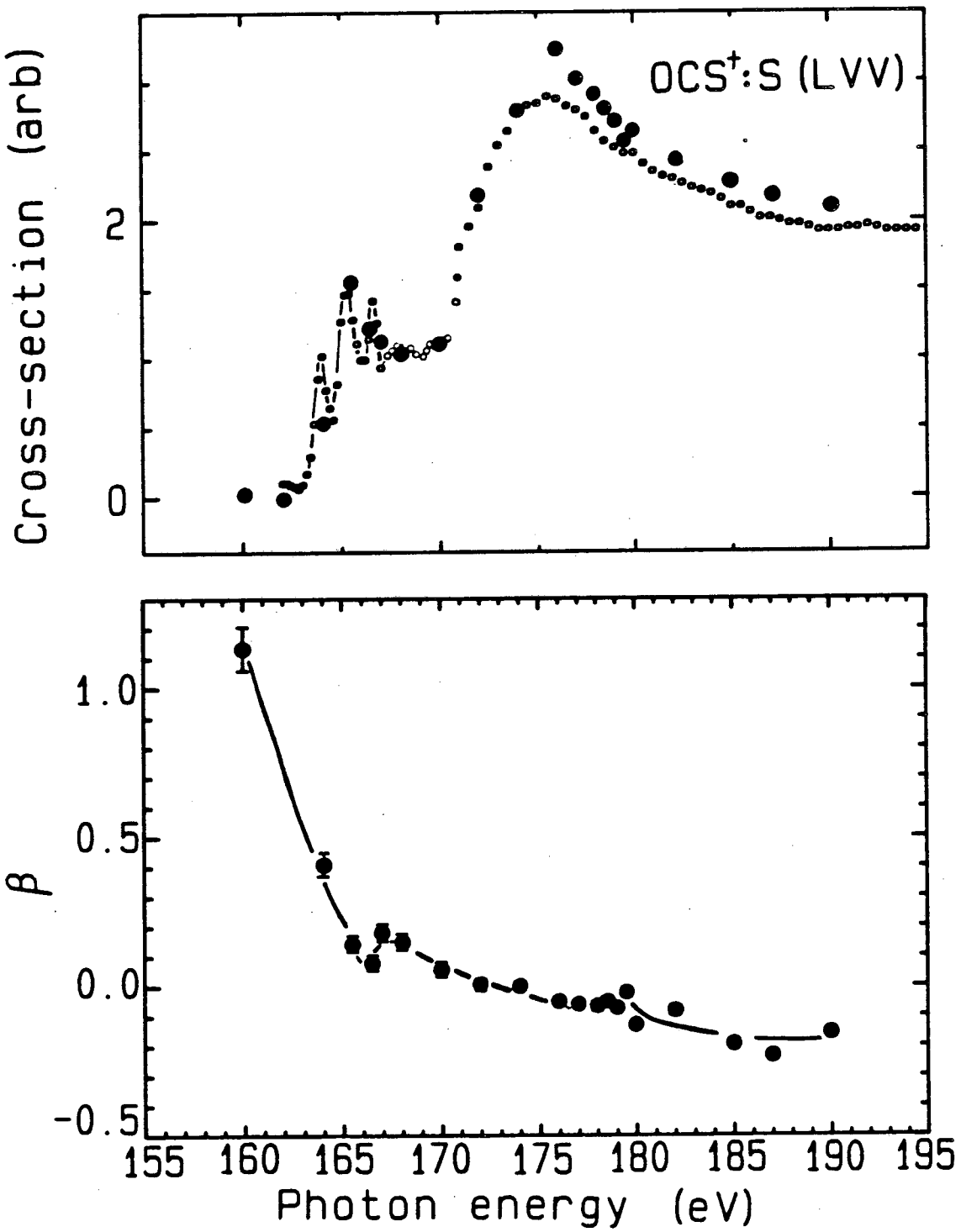

Fig. 22

XBL 828-11147

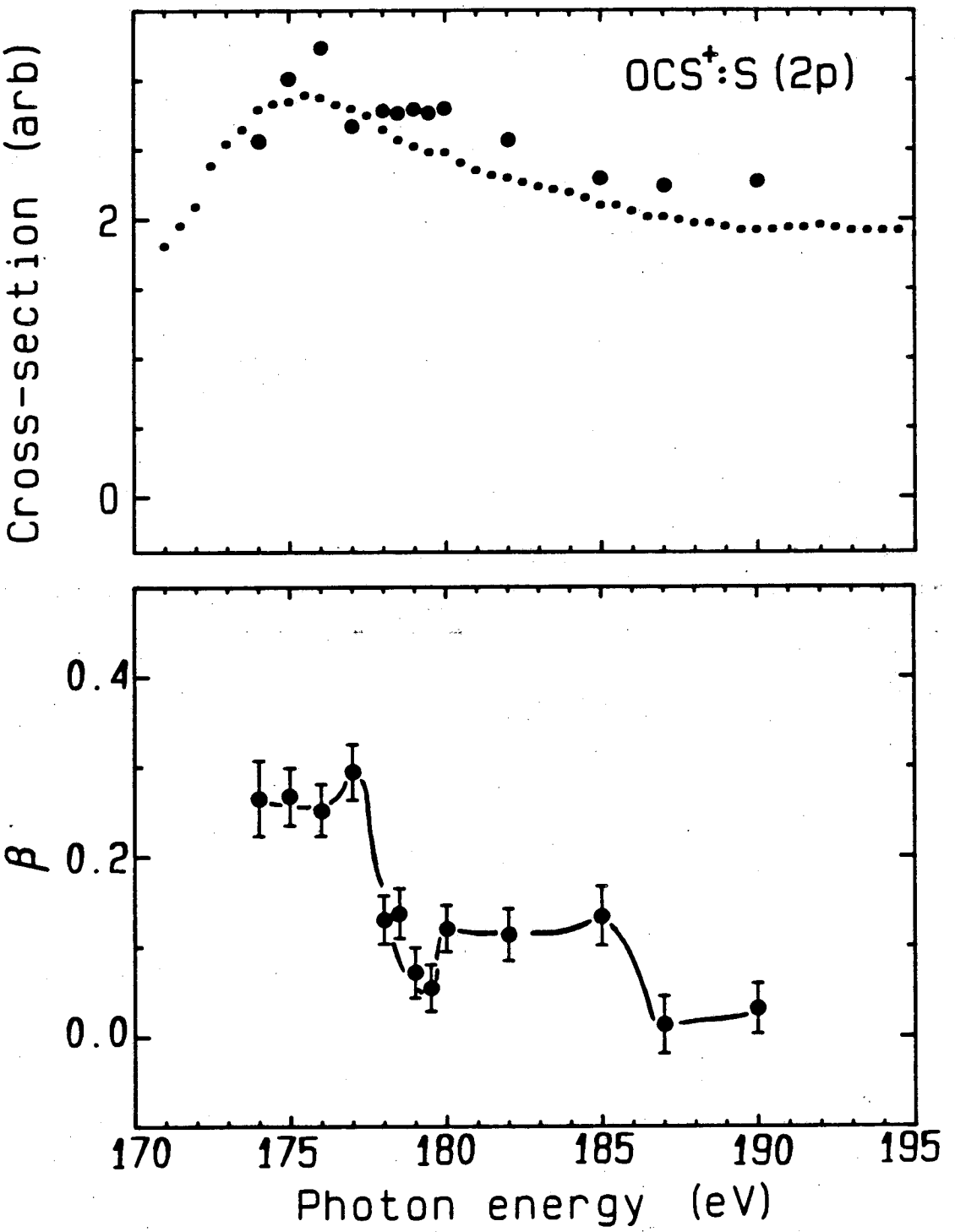

Fig. 23 XBL 828-11145

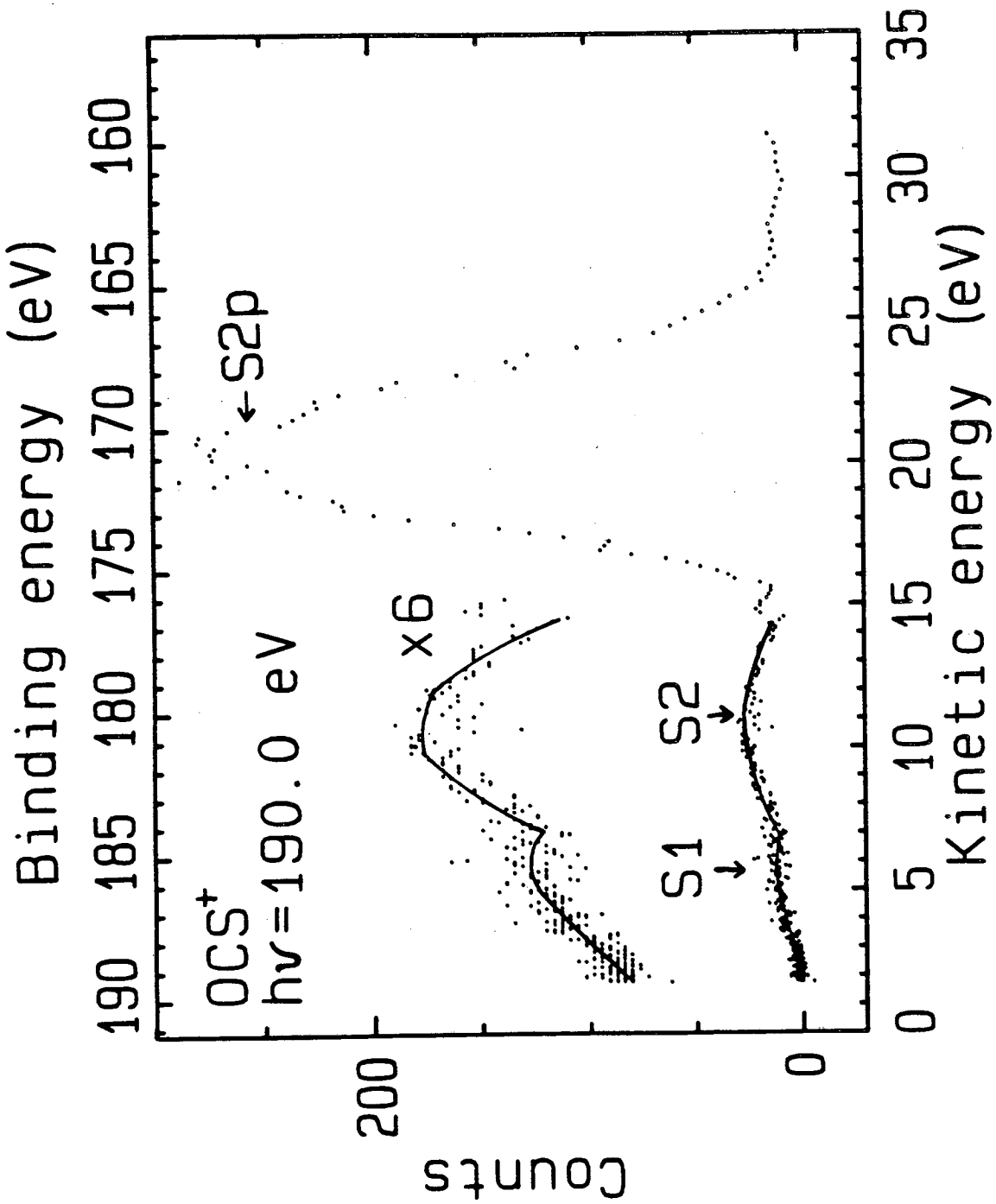

XBL 831-7880

Fig. 24

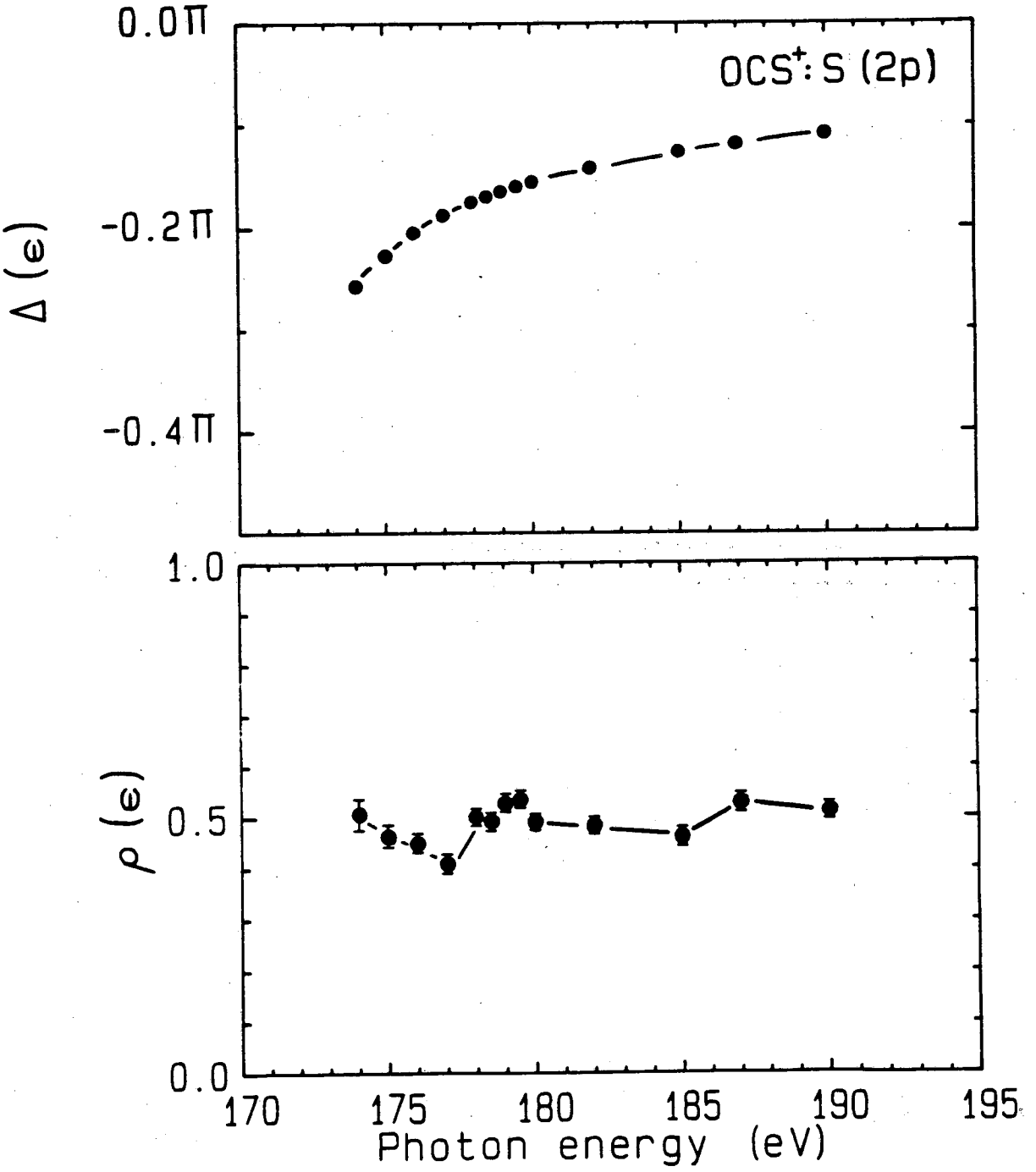

Fig. 25

XBL 831-7883

Acknowledgements

The collaborative work herein required many hours of preparation as well as sustained support from many individuals. I praise these people for their efforts in providing expertise, love, friendship toward the culmination of my graduate career.

I would like to thank my research director, David A. Shirley, for his support, for his scientific advice, and for allowing me the opportunity to investigate my own experimental interests.

I would like to acknowledge several co-workers for making the TOF "project" successful. Steve Southworth, Paul Kobrin, and Dennis Lindle were students whom I have worked with the longest period of time. Bill Brewer, Shige Owaki, Uwe Becker, and Hans Kerkhoff were visitors in our research laboratory. I thank Phil Heimann and Trish Ferrett, who are new students in our research group, for their assistance.

I would also like to thank Dennis Trevor, John Barton, and Charlie Bahr for providing helpful humor, suggestions, and information.

I would like to acknowledge support from the people in the mechanical engineering and machinists groups in building 70 A, TID, Joe Katz, and George Gabor. I would also like to thank the staff at SSRL for all of their assistance.

I would like to acknowledge Barbara Moriguchi, Wini Heppler, and the other members of the Shirley group for their friendship and assistance. I thank Deborah Colbert, Jean Wolslegel, and June de la Vergne for

their work in editing, and printing the final copy of this manuscript.

This work was supported by the Director, Office of Energy Research, Office of Basic Energy Sciences, Chemical Sciences Division of the U.S. Department of Energy under Contract No. DE-AC03-76SF00098. It was performed at the Stanford Synchrotron Radiation Laboratory, which is supported by the NSF through the Division of Materials Research.

TECHNICAL INFORMATION DEPARTMENT
LAWRENCE BERKELEY LABORATORY
UNIVERSITY OF CALIFORNIA
BERKELEY, CALIFORNIA 94720